Dissertation

submitted to the

Combined Faculties for the Natural Sciences and Mathematics

of the Ruperto-Carola University of Heidelberg, Germany

for the degree of

Doctor of Natural Sciences

Put forward by

Meike Charlotte Danisch

Born in Herford, Germany

Oral examination: 12.01.2022

Measurement of neutral mesons and direct photons in Pb–Pb collisions at $\sqrt{s_{\mathrm{NN}}} = 5.02\,\mathrm{TeV}$ with ALICE at the LHC

Referees: Prof. Dr. Johanna Stachel

Prof. Dr. Hans-Christian Schultz-Coulon

Abstract

The goal of the ALICE experiment at CERN is to study strongly interacting matter under extreme conditions, which are generated in ultra-relativistic heavy-ion collisions at the LHC. It has been established that a medium with unconfined quarks and gluons, the quark-gluon plasma (QGP), exists shortly after these collisions. Detecting direct photons produced in heavy-ion collisions can help characterize the properties and dynamics of this medium. We present the first direct photon measurement using the highest available heavy-ion collision energy per nucleon-nucleon pair of $\sqrt{s_{\mathrm{NN}}} = 5.02\,\mathrm{TeV}$. Photons are reconstructed from electron and positron track pairs, which emerge from the occurrence of pair production of photons in the detector material; this is the photon conversion method (PCM). Within the work of this thesis, new methods are developed and implemented in the analysis procedure. As a result, direct photon spectra and R_γ are presented in 0-20, 20-40, 40-60, and 60-80% classes of collision centrality. The neutral mesons π^0 and η constitute the largest background source for direct photons, with their decays to two photons, which is one motivation for measuring their spectra as precisely as possible. The second goal is to study the energy loss of partons in the QGP by observing the suppression of high transverse momentum particle production in heavy-ion collisions with respect to pp collisions. Neutral pion spectra and nuclear modification factors R_{AA} are presented in 0-10, 20-40, and 60-80% centrality classes, η meson spectra, R_{AA}, as well as η/π^0 ratios in 0-20, 20-40, and 60-80%.

Zusammenfassung

Das Ziel des ALICE Experimentes am CERN ist die Untersuchung von stark wechselwirkender Materie unter extremen Bedingungen, welche in ultrarelativistischen Schwerionenkollisionen, z.B. am LHC, herbeigeführt werden können. Es hat sich gezeigt dass für eine kurze Zeit nach einer solchen Kollision ein Quark-Gluon-Plasma (QGP) entsteht, in welchem Quarks und Gluonen ungebunden sind. Die Messung direkter Photonen, welche in Schwerionenkollisionen erzeugt werden, trägt dazu bei, die Eigenschaften und Dynamik dieses Materiezustandes zu charakterisieren. Die erste Analyse direkter Photonen aus Schwerionenkollisionen mit der höchsten verfügbaren Schwerpunktsenergie pro Nukleon-Nukleon Paar, $\sqrt{s_{\mathrm{NN}}} = 5.02\,\mathrm{TeV}$, wird vorgestellt. Photonen werden detektiert, indem Elektron-Positron Paare rekonstruiert werden, welche aus der Paarbildung im Detektormaterial entstehen, diese Methode nennt sich PCM (Photon Conversion Method). Im Zuge der vorgestellten Arbeit wurde die Analyseprozedur durch die Entwicklung und Anwendung neuer Methoden verbessert. Das Ergebnis, Spektren und R_γ aus den jeweils zentralsten 0-20, 20-40, 40-60 und 60-80% Kollisionen, werden vorgestellt. Da die neutralen Mesonsn π^0 und η den gröten Beitrag zum Untergrund des Signals direkter Photonen darstellen, sollen diese möglichst präzise gemessen werden. Die Untersuchung des Energieverlustes von Partonen im QGP über die Beobachtung reduzierter Produktion hochenergetischer Teilchen in Pb–Pb im Vergleich zu pp Kollisionen ist eine weitere Motivation. Spektren und R_{AA} des π^0 werden in den zentralsten 0-10, 20-40 und 60-80% Kollisionen gezeigt, Spektren und R_{AA} des η Mesons, sowie das Verhältnis η/π^0 in 0-20, 20-40 und 60-80%.

Contents

Chapter 1

Introduction

The main goal of the work presented in this thesis is the measurement of direct photons in ultra-relativistic heavy-ion collisions. A large amount of particles are produced in these collisions and photons are among their decay products. Direct photons however are defined as those that do *not* originate from the decays of other particles. For example, they can emerge from the initial scatterings of nucleons within the colliding ions. It has been established by experiments at CERN and BNL [1–4] that a state of strongly interacting matter where quarks and gluons are not bound within nucleons like in ordinary matter, the quark-gluon plasma (QGP), can be created in ultra-relativistic heavy-ion collisions. This hot and dense medium is expected to radiate direct photons as well, called thermal photons. A thermal photon signal is therefore a good signature of the QGP. Furthermore, because the mean free path length of photons is much larger than the medium size, photons can escape the QGP without further interaction and help characterize its properties. Therefore, measuring direct photons is one contribution to better understanding the behavior of strongly interacting matter under extreme conditions and consequently Quantum Chromodynamics (QCD), the theory of the strong interaction between quarks and gluons.
The basic concepts of QCD will be introduced in chapter 2, embedded in a short historical overview. Theoretical motivation for the existence of the QGP phase at high temperatures and densities will be given as well. In chapter 3, the method of ultra-relativistic heavy-ion collisions as a tool to study QCD and the QGP is presented. A historical overview of past experiments and some of their discoveries is given, as well as a description of the current general understanding of the course of events in a heavy-ion collision.
Chapter 4 is dedicated to the field of research of direct photons and neutral mesons and its discoveries. The measurement of the neutral mesons π^0 and η is the second goal of this work. Photons originating from their decays are the largest contribution to the considerable decay photon background.

Therefore, a precise measurement of neutral mesons is required in order to quantify the direct photon signal. Another motivation is that neutral mesons can be used to study the energy loss of highly energetic quarks and gluons (from initial nucleon-nucleon scatterings) in the QGP, as described in section 4.1. In section 4.2, more detailed information on the sources of photons in heavy-ion collisions will be given and theoretical considerations will be summarized as well. In addition, the physics observables which are determined experimentally will be introduced; a measurement of direct photons does not only comprise verifying their production, but also detecting how many photons have been created, having which energy. The latter can for example give a first hint on the origin of the direct photon. Angular distributions can provide important information as well but are beyond the scope of this thesis.
The data which was used for the presented analysis was recorded with the ALICE experiment, which is one of the four big experiments at the Large Hadron Collider (LHC) at CERN, and specialized on heavy-ion collisions. Pb–Pb collisions with a center-of-mass energy per nucleon-nucleon pair of 5.02 TeV were analyzed. This is the highest heavy-ion collision energy available worldwide and the first direct photon measurement at this energy is presented here. Both the ALICE experiment and the LHC will be described in chapter 6. The ALICE experiment offers different methods to detect photons. In addition to two electromagnetic calorimeters, photons can be reconstructed by detecting electron-positron pairs which originate from conversions of photons in the detector material. This so-called photon conversion method (PCM) is used in this analysis. Its main advantage over the calorimeters is the very good energy resolution [5]. The calorimeters can measure photons up to higher transverse momenta (the momentum transverse to the ion beam is called p_{T}), but the p_{T} range which is accessible with PCM even exceeds the region where thermal photons are expected to be the dominant contribution to direct photons.
As it will be described in more detail in section 4.2, direct photons have been measured previously in different collision systems with lower collision energies. Some disagreement was found between the results of different experiments and to calculations of theoretical models. The results of the analysis presented here might contribute to the resolution of this ambiguity. Compared to previous datasets recorded by ALICE, ions were not only colliding with higher energy but also a larger number of collision events was recorded for the dataset at hand. It was investigated to what extent this larger amount of statistics can improve neutral meson and direct photon measurements. As mentioned before, one of the main challenges when measuring direct photons is the large decay photon background, which has to be quantified using a measurement of neutral mesons. In this thesis, it was attempted to increase the precision by introducing new methods in the analysis procedure, which will be presented, followed by the analysis results,

in chapter 7 and chapter 8. [a]

[a] Small parts of this thesis have been copied from my ALICE-internal analysis note [6] and conference proceedings [7].

Chapter 2

Quantum chromodynamics and the quark-gluon plasma

After Hofstadter and McAllister found in 1955 that the proton is not a point-like particle but a composite object with substructure [8][9], a journey of discovery into the hidden world inside of the nucleons began. In 1964 Murray Gell-Mann and George Zweig proposed the new idea that protons and neutrons could be made up of so-called quarks [10][11] and indeed, a bit later in 1968, deep inelastic scattering experiments proved that the proton contains point-like constituents [12–15].
By now, quarks of six different flavors are an integral part of the standard model of particle physics (see Figure 2.1). They are considered to be point-like elementary particles, massive fermions, which carry an electric charge. In addition, each quark carries a color charge, of which there are three types, arbitrarily called red, green, and blue. The presence or motion of these color charges is what gluons, the exchange particles of the strong interaction, react to.

Back in the 1960s, physicists were wondering why these quarks are not observed as independent particles but seem to occur only confined together in hadrons. In 1973 David Politzer [17], David Gross, and Frank Wilczek [18] came up with a theory of the strong interaction featuring asymptotic freedom. The latter suggests that the coupling strength between quarks increases with increasing distance to another, which delivered an explanation for the observed confinement.
The fact that nucleons contain more constituents than quarks, was first supported by a measurement in 1971 which showed that only about half of the proton momentum is carried by its quarks [19][20]. It turned out that the rest is carried by gluons for which the direct evidence was provided in 1979 by observing the products of gluon bremsstrahlung in electron-positron collisions at DESY [21–24].
The quantum field theory of the strong interaction, known as Quantum

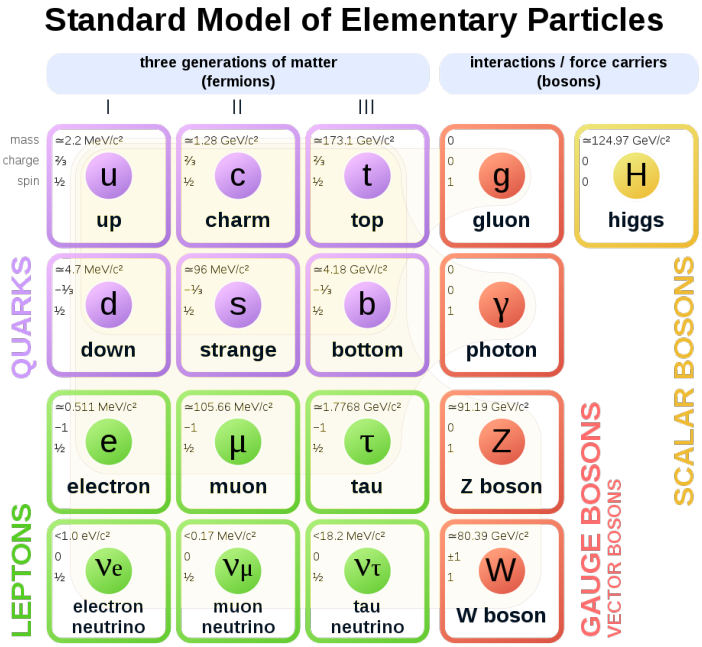

Figure 2.1: Elementary particles in the standard model of particle physics [16]. In addition to the up and down quarks, which are the constituents (valence quarks) of protons and neutrons, there are four more, heavier types of quarks. The four gauge bosons are the mediators of three of the four fundamental interactions; the gluon for the strong force, the photon for the electromagnetic force, and the W and Z bosons for the weak force. Mass, charge, and spin of all particles are listed in the figure.

Chromodynamics (QCD), which was further developing in parallel with the experiments, describes 8 different types of gluons. They carry color charge themselves, and therefore can also interact with each other.
One consequence of asymptotic freedom is that processes with high momentum transfer or small distances can be calculated with perturbation theory, where the solution to a problem is written as a power series in a small parameter, which is, in this case, the coupling strength α_s of the strong interaction. This approach is called perturbative QCD (pQCD).
Early calculations based on QCD indicated that strongly interacting matter, when it exceeds a certain temperature or density undergoes a transition into a different phase where quarks and gluons are free [25, 26], called Quark Gluon Plasma [27].
For the regime where α_s is large, where pQCD cannot be applied, the numerical approach called lattice QCD [28] is used, in which space-time is discretized, which simplifies the calculations. Monte Carlo techniques are used to calculate expectation values of physical observables [29].

Lattice QCD has proved itself capable of describing quantities quite precisely in agreement with measurements, for example, the masses of a variety of hadrons [30].
With this method, the energy density of strongly interacting matter can be calculated as a function of its temperature, for example. It features a rapid increase above 130 MeV [31][32] which can be explained by a transformation of hadrons, when heated up, into a deconfined state of matter, the QGP. This is related to an increase in the number of degrees of freedom (due to the different possible flavor, color, spin, and polarization states of quarks and gluons) in the QGP than in the hadron phase. Another theoretical argument for deconfinement is delivered by the analysis of fluctuations of conserved charges (like charge, baryon number, and strangeness) as a function of temperature. For example, the difference between the second and fourth-order cumulants of baryon number fluctuations starts to deviate from zero for temperatures $T > 145\,\mathrm{MeV}$, which indicates the presence of degrees of freedom with fractional baryon numbers (like quarks) [33][34].
The behavior of strongly interacting matter can be visualized in a phase diagram [26] like in Figure Figure 2.2. It is shown in dependency of its temperature and baryon chemical potential μ_B. When describing equilibrated QCD matter with thermodynamics, μ_B expresses the amount of energy that is absorbed or released when the baryon number is changed. The diagram displays ordinary nuclear matter, the heated hadron gas, as well as the QGP phase at even higher temperatures and densities. The first microseconds after the Big Bang, the universe was most likely in this state [37] before it cooled down and hadrons, atoms, and stars could form.
Another property distinguishes hot and dense from cold nuclear matter: hot QCD matter, where quark masses are small compared to its temperature, is characterized by chiral symmetry, whereas in normal nuclear matter chiral symmetry is broken. Calculations for $\mu_\mathrm{B} = 0$ with physical quark masses show that the transition in-between is not a phase transition but a continuous crossover [38][39]. The corresponding pseudo-critical temperature was calculated as $T_\mathrm{c} = (156.5 \pm 1.5)\,\mathrm{MeV}$ [40].

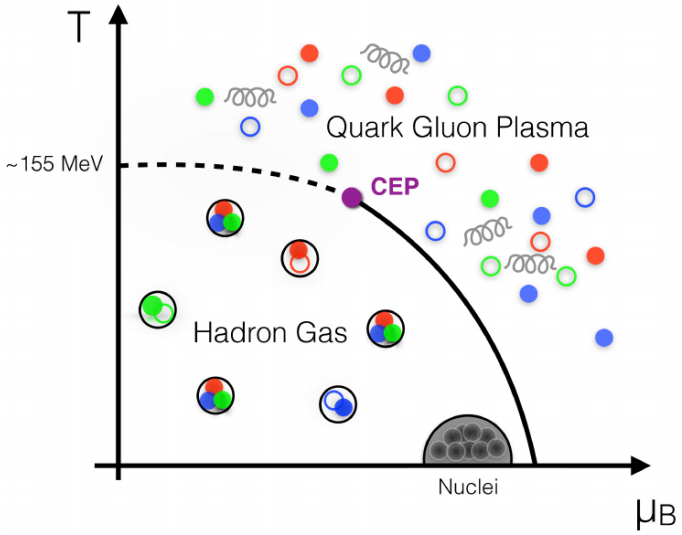

Figure 2.2: Phase diagram of strongly interacting matter [35]. The dashed line at low μ_B illustrates the smooth transition (crossover) between the hadron gas and the QGP (as opposed to a phase transition with a discontinuous change of thermodynamic properties). For higher values of μ_B, the existence of a second-order critical endpoint (CEP) [36] was postulated, followed by a line of first-order phase transition.

Chapter 3

Ultra-relativistic heavy-ion collisions

The energy densities and temperatures which are required in order to create a quark-gluon plasma in the laboratory can be achieved by colliding heavy atomic nuclei which are moving with almost the speed of light. In these ultra-relativistic heavy-ion collisions, physicists want to investigate strongly interacting matter under extreme conditions, explore the QCD phase diagram and investigate the QGP phase, for example, its equation of state and transport properties.

Experiments with one beam aiming at a fixed target were for example pursued at the Super Proton Synchrotron (SPS) at CERN, and the Alternating Gradient Synchrotron (AGS) at the Brookhaven National Laboratory (BNL) starting in the 1980s, with $20 - 200\,\mathrm{GeV}$ and $2 - 15\,\mathrm{GeV}$ beam energies per nucleon, respectively. Collisions of in opposite directions moving ions started in 2000 at the Relativistic Heavy Ion Collider (RHIC) with center-of-mass collision energies per nucleon-nucleon pair of $\sqrt{s_{\mathrm{NN}}} = 130 - 200\,\mathrm{GeV}$ using gold, and at the Large Hadron Collider (LHC) starting in 2010 with $\sqrt{s_{\mathrm{NN}}} = 2.76 - 5.02\,\mathrm{TeV}$ using lead (and later xenon). Different values of $\sqrt{s_{\mathrm{NN}}}$ are provided by the different accelerators and make different paths in the QCD phase diagram accessible. At the LHC, a medium with very high temperatures at very low μ_{B} can be created.

Before giving a description of the current general understanding of the course of events in a heavy-ion collision, the next paragraphs focus on proton-proton and proton-ion collisions first, for simplicity.

Proton-proton collisions

When two protons collide, it is their constituents that scatter off each other. The incoming constituents can be either one of the three valence quarks within each proton or one of the virtual quarks, antiquarks, or gluons. The probability to find a quark or gluon with a certain momentum fraction x of the total proton momentum is described by so-called parton distribution

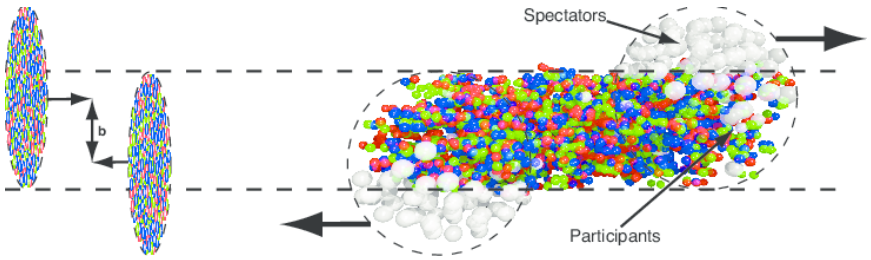

Figure 3.1: The sketch on the left illustrates the definition of the impact parameter b in a heavy-ion collision. The ions are drawn flat because of the Lorentz contraction which is caused by their relativistic speed. The sketch on the right side shows how it is related to the number of participant- and spectator nucleons [42].

functions (PDF), which are functions of the momentum transfer Q^2. When the incoming protons are moving very fast, with almost the speed of light, the outgoing partons, quarks, and gluons, can be very energetic as well. This process is called hard scattering. It is followed by low-energy processes like gluon radiation and quark-antiquark pair creation, so that a shower of partons, all moving in a similar direction, is created around each outgoing parton (a jet). Then, in order to obey confinement, all free quarks get bound as hadrons, which can then be measured in the surrounding detectors.

Proton-ion collisions

When colliding a proton with an ion instead of another proton, most of the nucleons are unaffected by the collision, but the situation gets somewhat more complicated. In the atomic nucleus, protons and neutrons are bound by the nuclear force. Now, the constituents of the proton can interact with the constituents of the protons and neutrons within the nucleus. However, there is a higher chance for multiple parton-parton interactions than in a proton-proton collision. Also, the PDFs are changed by the nuclear environment and are called nuclear pdfs (nPDF) in this case, originally motivated by the fact that experimental results from deep inelastic scattering off nuclei could not be explained using PDFs of free nucleons (for a review see [41]).

Ion-ion collisions

The collision of two ions is characterized by its impact parameter, which is the distance of the two centers of the nuclei, in a plane perpendicular to the beam axis (see Figure 3.1). The larger the impact parameter, the more nucleons remain unaffected by the collision. These are called spectators. The more central the collision, the larger the overlap region and the more nucleons participate in interactions, with those coming from the other side. The spectators keep on traveling in their original direction. A large number of quarks, antiquarks, and gluons are created in the overlap region. They interact with each other frequently, so that the whole system of particles can approach local states of thermal equilibrium after $\tau_0 \approx 1\text{fm}/c$. If the collision energy and centrality was high enough, the energy density is initially

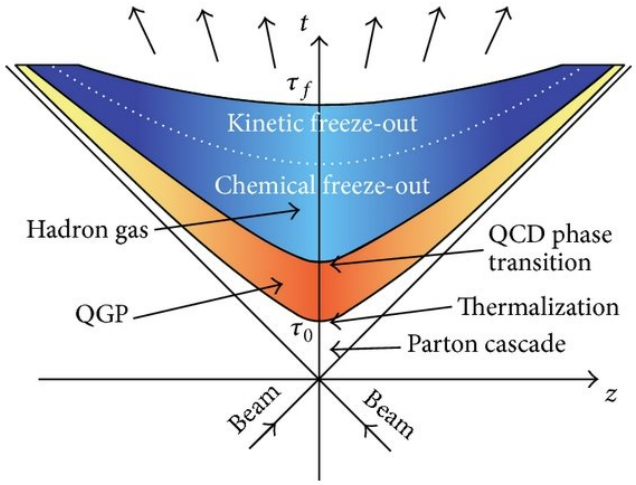

Figure 3.2: Sketch of the space-time evolution in and after a heavy-ion collision [43].

above the critical energy density (The calculated value in (2+1)-flavor lattice QCD for $\mu_B = 0$ is $\epsilon_c = (0.34 \pm 0.16)\,\mathrm{GeV/fm^3}$) so that the quarks do not hadronize immediately but make up a fluid-like medium called quark-gluon plasma (QGP), see Figure 3.2. Its properties like temperature, volume, pressure and chemical potential can now be described by its equation of state and relativistic hydrodynamics. Due to the large pressure gradient between the medium and the vacuum surrounding it, it expands quickly. This also means that the particles collectively move (flow) outwards. While expanding, the system cools down and the crossover takes place when the pseudo-critical temperature is reached. After the confinement transition, the system has transformed into a hot hadron gas. The moment when the hadron yields are fixed is called chemical freeze-out. However, the particles can still engage in elastic collisions. Then, after kinetic freeze-out, they do not change their momentum anymore. Along with the particles which were created in hard scatterings and around the highly energetic partons, those which were created during hadronization of the QGP, move away from the interaction point and can be observed by surrounding detectors. The probability with which a certain parton fragments into a certain final state particle species (with momentum fraction z) is usually described by fragmentation functions (FF). They can be modified (mFF) significantly in collisions of nuclei with respect to those in nucleon or lepton collisions; Because of the presence of the medium which they have to traverse, partons can lose part of their energy in interactions like elastic scattering and gluon radiation.
It has to be noted that the described picture is the traditional one where the creation of a hot and dense medium is only expected in AA collisions,

however, more recent measurements question this assumption (see for example [44]).
In the following paragraph a short historical overview over heavy-ion experiments is given, which are or have been operating at the aforementioned accelerator facilities, and their most important discoveries. The observation of particles in these experiments is based on the principles of interaction of particles with matter, which is the topic of chapter 5.
In 2000, after the SPS heavy-ion beams had been used for fixed target collision experiments (NA*, WA*, etc.) for over a decade, in order to study strongly interacting matter under extreme conditions, the results from a variety of measurements were interpreted as "evidence for a new state of matter" which had been created in the laboratory [1][2].
The same year, RHIC started colliding gold ions with a 10 times higher center-of-mass energy. The experiments at the intersection points (STAR, PHENIX, PHOBOS, BRAHMS) were designed to further investigate the properties and behavior of this new state of matter and clarify if it is the theoretically predicted quark-gluon plasma.
One important discovery was the phenomenon of jet quenching [45–48]. As mentioned before, while the hard scattered partons travel through the created medium, they can lose energy by interacting with the medium constituents, the quarks and gluons. This was experimentally observed by comparing hadron spectra in nucleus-nucleus (AA) collisions to those in pp collisions, which revealed a significant suppression and shift to lower momenta in the spectra which were measured in AA collisions. Additional evidence for the interpretation that this observation is caused by parton energy loss was provided by the fact that in pA collisions, where no creation of a QGP was expected, also no suppression of high-momentum hadrons was observed. Also, direct photons, which would not be affected by the strong force governing a medium made of quarks and gluons, were not suppressed in AA collisions, as opposed to hadrons [49].
An important step towards revealing the nature of the created medium was taken with measurements of elliptic flow. In non-central nucleus-nucleus collisions, the overlap region where the two nuclei cross each other has an almond-like shape, which determines the initial shape of the medium. This leads to different pressure gradients in different directions, so that the medium expands anisotropically, unlike in central collisions. Therefore, particles in different fluid cells, of which each is characterized by a common velocity, are accelerated differently. Experimentally, the resulting azimuthal anisotropy of final velocities is addressed by measuring the angular distribution (with respect to the reaction plane) of momenta of the particles which enter the surrounding detectors. Using a Fourier decomposition of that distribution, one can extract the Fourier coefficients, of which the second one is referred to as elliptic flow coefficient v_2. Measurements of v_2 for different hadrons could confirm the predictions from hydrodynamical calculations

and simulations, modeling the expansion of a hot, liquid medium [3]. Since the elliptic flow coefficient is sensitive to the existence and value of viscosity of the medium (besides the initial conditions and equation of state) and the data could be described by non-viscous hydrodynamics quite well, it was deduced that the viscosity of the medium must be very small.
When the LHC started operating with lead ion beams in 2010, an even higher center-of-mass collision energy became available for heavy-ion collisions, which helped answer so far open questions. Proton-proton and proton-ion collisions were also on the schedule, being studied by the four big experiments ATLAS, CMS, ALICE, and LHCb. Of those, ALICE is the one which is specialized in investigating heavy-ion collisions.
An important piece of information was given by measuring yields of a variety of identified hadrons with different masses in ALICE and analyzing these with the statistical hadronization approach [50]. The measured particle multiplicities can be well reproduced by modeling a hadron resonance gas (which goes back to Hagedorn [51] [52]) by means of a statistical (grand canonical) ensemble of particles in chemical equilibrium, being produced simultaneously during a chemical freeze-out (cf). The temperature T_{cf} and baryon chemical potential μ_{B} of this ensemble are the two free parameters. By fitting the model to the measured hadron yields in most central Pb–Pb collisions, the medium properties at the time of chemical freeze-out can be obtained ($\mu_{\mathrm{B}} = 0.7 \pm 3.8\,\mathrm{MeV}$ and $T_{\mathrm{cf}} = 156.5 \pm 1.5\,\mathrm{MeV}$). It is remarkable that the temperature agrees well [50] with the results from lattice QCD calculations for the pseudo-critical temperature [53][32], and even [54] with the more precise result [40]. The chemical freeze-out temperature has also been extracted from hadron measurements with experiments using lower collision energies [55–61]. Comparing all results shows that T_{cf} increases with increasing energy and saturates at some point, which confirms the expectation that hadronic matter cannot be heated above a certain critical temperature without transitioning into a whole different phase.
The time until kinetic freeze-out τ_{kf} and the volume V_{kf} of a homogeneous region in the medium at that time can be measured with a method called HBT (Hanbury Brown and Twiss) interferometry [62]. Analyses showed that the lifetime of the medium in central Pb–Pb collisions at $\sqrt{s_{\mathrm{NN}}} = 2.76\,\mathrm{TeV}$ is $\tau_{\mathrm{kf}} \approx 10\,\mathrm{fm/c}$ [63]. The medium size was determined as $V_{\mathrm{kf}} \approx 5000\,\mathrm{fm}^3$ [64][63].
These findings, together with those from analyses of multiplicity and azimuthal anisotropy, indicate that at LHC energies the produced medium has a higher temperature, longer lifetime and larger volume at freeze-out than at the lower RHIC energies [63].
Low p_{T} direct photons, as well as other electromagnetic probes, can serve as more or less direct QGP signatures. This thesis contributes to this field of research, which will be discussed in chapter 4.

Chapter 4

Motivation for measuring neutral mesons and direct photons

4.1 Light neutral mesons π^0 and η

By comparing neutral meson yields between pp and AA collisions, we can study the energy loss of hard partons in the QGP, in order to investigate the properties of the created medium. This is usually done by measuring the nuclear modification factor

$$R_{\mathrm{AA}} = \frac{\mathrm{d}^2 N^{\mathrm{AA}}/\mathrm{d}p_{\mathrm{T}}\mathrm{d}y}{\langle T_{\mathrm{AA}} \rangle \, \mathrm{d}^2\sigma^{\mathrm{pp}}/\mathrm{d}p_{\mathrm{T}}\mathrm{d}y} \tag{4.1}$$

where a particle yield in AA collisions N^{AA} is compared to the corresponding cross section σ^{pp}, measured for that particle type in pp collisions. It is measured differentially in the transverse momentum p_{T} (transverse to the beam axis) and rapidity y. The nuclear overlap function $\langle T_{\mathrm{AA}} \rangle = \langle N_{\mathrm{coll}} \rangle / \sigma^{\mathrm{NN}}_{\mathrm{INEL}}$ is proportional to the average number of nucleon-nucleon collisions $\langle N_{\mathrm{coll}} \rangle$ in the considered centrality class, which is obtained from simulations of nuclear collisions [65], based on the Glauber model (a short description of the latter can be found in the paragraph on centrality determination in section 6.4). The quantity $\sigma^{\mathrm{NN}}_{\mathrm{INEL}}$ is the full cross section for inelastic nucleon-nucleon collisions, which is measured separately in a different analysis [66][67]. A measured R_{AA} of 1 would indicate that the particle production in AA collisions could be evoked by an independent superposition of nucleon-nucleon collisions. The commonly measured R_{AA} smaller than 1 is referred to as suppression. At low p_{T}, it can be used to study collectivity in the medium evolution and hadronization. In the high p_{T} domain, we can investigate parton energy loss.
Because the comparison of measurements to theoretical models is used for

gaining insights, some theoretical considerations and aspects of the used models are described in the following. The cross section σ^{pp} for a given process in pp collisions can be calculated by factorizing it [68][69][70][71] into parton distribution functions (PDF), the partonic scattering cross sections $\hat{\sigma}$, and fragmentation functions (FF), illustrated by the simplified expression of convolution products:

$$\sigma^{\mathrm{pp}} = \int \mathrm{PDF} \otimes \mathrm{PDF} \otimes \hat{\sigma}_{\mathrm{pQCD}} \otimes \mathrm{FF}. \tag{4.2}$$

The partonic cross sections can be calculated with pQCD. Fragmentation functions (e.g. [72],[73],[74]) and PDFs (e.g.[75][76]) can be obtained from the analyses of simpler collision systems like e^+e^- and ep.
In order to calculate particle production in AA collisions at high p_{T}, one has to modify equation 4.2 by using nuclear PDFs (e.g.[77]) instead of proton PDFs. The nPDFs are generated by analyzing data primarily from lepton-nucleus and pA collisions. In addition, one has to account for parton energy loss. In some models, the latter is incorporated by using modified fragmentation functions, other models calculate it separately. The energy loss of a parton depends on its own properties (its energy and if it is a gluon or a quark jet) as well as on the medium properties like the jet transport coefficient $\hat{q}$, which can be quantified by measuring high p_{T} particle production [78]. For calculating effects which are relevant for the low p_{T} region, hydrodynamics simulations of the medium evolution are used.

As mentioned before, jet quenching, the suppression of high p_{T} hadrons in AA with respect to pp collisions was first observed at RHIC with measurements of inclusive charged particles, and interpreted as the energy loss of hard scattered partons in the medium [79][80]. In the most central collisions, neutral pions were found to be suppressed by a factor of about 5 in the region $5\,\mathrm{GeV}/c < p_{\mathrm{T}} < 10\,\mathrm{GeV}/c$ [81]. Measurements of charged particle production at the LHC with a much higher collision energy of $\sqrt{s_{\mathrm{NN}}} = 2.76\,\mathrm{TeV}$ were able to test the suppression up to higher p_{T} than previously possible [82–84] and showed that it is stronger than at RHIC (≈ 7 for $5\,\mathrm{GeV}/c < p_{\mathrm{T}} < 10\,\mathrm{GeV}/c$.). Furthermore, it was observed that the R_{AA} increases with decreasing collision centrality. Also, an increasing trend for increasing p_{T} was found, as opposed to the measurements at RHIC, which can be understood considering the interplay between the energy dependence of parton energy loss and the shape of the p_{T} spectrum of partons [85]. Also, gluons and quarks are suppressed differently and might contribute by a different amount to particle production in different p_{T} regions [86].
Important information can be obtained by the measurement of identified particles, allowing the comparison of the R_{AA} between mesons and baryons, as well as between hadrons with different masses and quark compositions. While the latter is a superposition of $\mathrm{u\bar{u}}$ and $\mathrm{d\bar{d}}$ for the neutral pion, it is

a superposition of $u\bar{u}$, $d\bar{d}$ and $s\bar{s}$ for the η meson. Measurements [87][81] found that at high p_T, the suppression of η mesons is similar to the one of π^0 and kaons which suggests that it is a purely partonic effect.
The η/π^0 ratio was found to approach a universal constant value (≈ 0.5) in different collision systems and -energies for high p_T [88]. A measurement of π^0 and η mesons can also be used to test m_T-scaling, which is the phenomenological observation that cross sections of different particles have the same shape when plotted as a function of their transverse mass $m_T = \sqrt{m_h^2 + p_T^2}$, where m_h is the hadron mass [89] [90]. However, a dependence of the spectra in the low and intermediate p_T region on the collision system and centrality is expected, considering that collective flow in AA collisions affects the heavier η meson differently than the lighter pion. This would cause a violation of m_T-scaling and also will be reflected in the η/π^0 ratio. A measurement of η/π^0 with sufficiently small uncertainties in the intermediate p_T region would also be sensitive to the jet transport coefficient [86].

Most photons which are produced in a heavy-ion collision originate from the decay $\pi^0 \rightarrow \gamma\gamma$ followed by $\eta \rightarrow \gamma\gamma$. The sum of all photons from any hadron decay is referred to as decay photons. Direct photons are defined as those which come from other processes than hadron decays. In order to measure direct photons, the decay photon background has to be determined precisely, which is another motivation to measure as many mother particles as possible. The π^0 is the most relevant and most abundantly produced one, and therefore easiest to measure, followed by the η which is more challenging. The direct photon excess over decay photons can then be determined on a statistical basis.

4.2 Direct photons

In order to understand the properties of the QGP, a variety of hadronic observables are used, but while hadrons are created during freeze-out, photons are emitted also during all previous stages of the collision and afterward they can leave the medium without further interaction because their mean free path length is much larger than the system size. Therefore, it is possible to look directly into the medium at higher temperatures and earlier times than with hadrons. In order to understand which pieces of information about which medium properties are carried by photons, one has to understand in which processes they are emitted. As mentioned in the previous chapter, the vast majority of all created photons are decay photons from π^0 and other particles. All photons which do not originate from hadron decays are called direct photons. They can be classified into the following categories.

Prompt photons come from interactions of partons within the colliding nuclei (Feynman diagrams (a) and (b) in Figure 4.1), and the fragmentation of scattered partons into photons among other particles, including Bremsstrahlung (Feynman diagram (c) in Figure 4.1)). Photons from the processes (a) and (b) occur back-to-back with a jet, whereas those from (c) can be found within a jet. The production of prompt photons in pp collisions can be calculated with pQCD [92–95], in a similar manner like calculating hadron production, factorizing the cross section into partonic cross sections, (n)PDFs and fragmentation functions to photons [96][97] (see also Equation 4.2). In AA collisions, fragmentation photons could be suppressed with respect to pp collisions because of the energy loss of the parton in the medium before the photon is created. On the other hand, the interaction of jets with the medium could generate new photons, which might balance the suppression [98][99].

Thermal photons

When a medium is sufficiently hot and dense, its constituents (in the case of a heavy-ion collision the partons in the QGP and later the hadrons in the

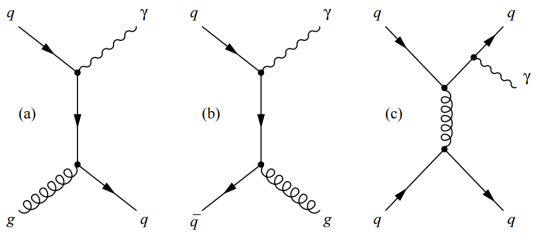

Figure 4.1: Feynman diagrams of direct photon production processes to leading order: (a) quark-gluon Compton scattering, (b) quark-antiquark annihilation, and (c) Bremsstrahlung/fragmentation. Figure from [91].

hadron gas) scatter off each other and produce photons. If the QGP is not yet in equilibrium, they are called pre-equilibrium photons, otherwise thermal photons. In an equilibrated medium with temperature T the thermal photon emission rate R depends approximately exponentially on the photon energy E:

$$E\frac{\mathrm{d}R}{\mathrm{d}^3p}(E,T)\propto T^2\mathrm{e}^{-E/T} \tag{4.3}$$

[100][101][102]. Therefore, direct photons carry information about the temperature of the medium.
In the hadron gas, photons can be emitted in reactions between mesons (like $\pi+\rho\rightarrow\pi+\gamma$) and baryons, in radiative decays, or hadron Bremsstrahlung [103–107]. They also feature an approximately exponential spectrum at low p_{T} [103].
At high p_{T} direct photons are dominated by prompt photons because of their power-law spectral shape, in contrast to the approximately exponentially distributed thermal photons, which should dominate at lower $p_{\mathrm{T}}\lesssim 3\,\mathrm{GeV/c}$ [108]. Therefore, thermal photon production can be tested especially well by measuring direct photons at low p_{T} and prompt photons at high p_{T}.
Pre-equilibrium photons
It is natural to assume that the medium before reaching equilibrium emits photons as well. The initial state of the medium between collision and thermalization can be theoretically described as Glasma [109][110]. In [111] it was demonstrated that its contribution to direct photon production, which had not been taken into account before, is comparable to that of the thermal phase. Further theoretical calculations including pre-equilibrium photons [112] [113] showed that direct photons are sensitive to the pre-equilibrium stage. Therefore, photons might be able to even probe the medium before the QGP is created. However, there is no consensus on the impact of this contribution [114].
Furthermore, the effect of strong magnetic fields in non-central heavy-ion collisions on photon production was studied [115][116][117].

Measuring direct photons is experimentally challenging because the decay photon background has to be estimated very precisely. Technically, this is done on a statistical basis, by calculating the ratio of the two measured quantities inclusive photons γ_{I} and decay photons γ_{D}:

$$R_\gamma=\frac{\gamma_{\mathrm{I}}}{\gamma_{\mathrm{D}}}=\frac{\gamma_{\mathrm{dir}}+\gamma_{\mathrm{D}}}{\gamma_{\mathrm{D}}}=1+\frac{\gamma_{\mathrm{dir}}}{\gamma_{\mathrm{D}}} \tag{4.4}$$

so that $R_\gamma>1$ indicates a direct photon signal, which can then be compared to the sum of expected photons from the different sources.
Direct photons in AA collisions have been observed for the first time in the WA98 fixed target experiment [118] at SPS with Pb–Pb collisions at

$\sqrt{s_{\mathrm{NN}}} = 17.3\,\mathrm{GeV}$ at low p_{T}. Comparisons to expectations for prompt photons hinted towards the existence of an additional photon source. At RHIC, the PHENIX experiment observed a direct photon signal in Au–Au collisions at $\sqrt{s_{\mathrm{NN}}} = 200\,\mathrm{GeV}$ in different centrality classes up to $\approx 14\,\mathrm{GeV}$ [119]. It was found to be consistent with N_{coll}-scaled pQCD calculations for pp collisions, which confirmed pQCD calculations for prompt photons, including nPDFs, partonic cross sections and fragmentation functions to photons. Later, direct photons were measured more precisely in the low p_{T} region and the PHENIX collaboration found a large signal of $R_\gamma \approx 1.2$ in the 0-20% most central events [120] [121]. At the LHC, the ALICE experiment measured direct photons in $\sqrt{s_{\mathrm{NN}}} = 2.76\,\mathrm{TeV}$ Pb–Pb collisions [122] [123]. A direct photon signal of $R_\gamma \approx 1.1$ was found with 2σ significance in most central events in the range $1\,\mathrm{GeV/c} < p_{\mathrm{T}} < 2\,\mathrm{GeV/c}$, which exceeds the expected prompt photon contribution and therefore can be attributed to thermal photons. However, the signal is much smaller than the one observed by PHENIX. At higher p_{T} the ALICE measurement is consistent with expectations from pQCD calculations for prompt photons as well. The direct photon analysis of the STAR collaboration [124] also found values of R_γ above the pQCD calculation for prompt photons with a significance of 1.8σ at $p_{\mathrm{T}} = 5.5\,\mathrm{GeV/c}$. However, their results are systematically below the PHENIX values up to 60% centrality and consistent with model calculations within uncertainties up to 80% centrality.

From the slope of the low p_{T} direct photon spectrum, one can extract information about the temperature of the medium. However, the photon emission rates are averaged over the whole medium evolution time and convoluted with the collective flow of the medium because - due to the movement of the emitting source towards the detector - the photon energies are blueshifted. Therefore, the measured inverse slope of the spectrum corresponds to an effective temperature T_{eff}, which is the time-average of the observable temperature $T_{\mathrm{obs}}(t)$:

$$T_{\mathrm{obs}}(t) = \sqrt{\frac{1+\beta_{\mathrm{flow}}(t)}{1-\beta_{\mathrm{flow}}(t)}} \cdot T(t), \tag{4.5}$$

where $T(t)$ is the actual temperature of the medium at time t. From analyzing the most central AA collisions, the effective temperature $T_{\mathrm{eff}} = (239 \pm 7\mathrm{stat} \pm 25\mathrm{syst})\,\mathrm{MeV}$ was extracted by PHENIX and $T_{\mathrm{eff}} = (297 \pm 12\mathrm{stat} \pm 41\mathrm{syst})\,\mathrm{MeV}$ by ALICE, which is both much larger than the expected deconfinement temperature. However, the development of the actual temperature over time can only be extracted by employing models which describe the whole evolution of the system.

Other interesting observables are the flow coefficients of direct photons. Even though thermal photons are neither in thermal equilibrium nor flow with the medium themselves, they still are emitted with the anisotropy

which the medium has at photon production time. This anisotropy can be addressed by measuring direct photons differentially in the azimuthal angle with respect to the event plane. The PHENIX collaboration found that the elliptic flow of direct photons (v_2) is comparable to that of neutral pions [125]. The term direct photon puzzle was coined because it was difficult for theoretical models to describe the large anisotropy and the PHENIX direct photon spectra simultaneously. At the LHC, the ALICE collaboration measured the direct photon elliptic flow in central and semi-central Pb–Pb collisions [126]. As expected, the v_2 in central events is smaller than the one in semi-central events because of the smaller initial spatial anisotropy in the first case. At low p_{T}, where the direct photon signal was attributed to thermal photons, $v_2 > 0$ is found with a significance of about 1–2 σ, which reflects the average elliptic flow of the medium at photon production times. Towards higher p_{T} it decreases, which is consistent with the growing importance of promt photons with $v_2 \approx 0$ (no momentum anisotropy yet). The measurement confirmed that the v_2 of direct photons is similar to that of decay photons, which come from neutral pions mostly. A Bayesian approach was used to estimate the uncertainty and no significant deviation from model predictions was found. However, all predictions lie below the data points, which confirms the tension between data and theory.
The flow coefficients are sensitive to the viscosity of the medium [127–129], however, the experimental uncertainties are currently still too large in order to discriminate between different model predictions [125] [126] [129].
Summarizing, photon yields and flow coefficients are sensitive to the medium temperature and anisotropy (due to collective flow of the medium constituents) at photon production time. Therefore, we can use photon measurements to cross-check our understanding of the space-time evolution and photon emission rates.
One goal for the measurements carried out in this thesis is to reduce their uncertainty, in order to achieve a better significance and to be able to better confirm or exclude model predictions. In the low p_{T} region of the ALICE measurement, systematic uncertainties dominate and need to be reduced. Another goal is to compare measurements among different collision systems and energies; the analysis presented in this thesis uses a new dataset with Pb–Pb collisions at $\sqrt{s_{\mathrm{NN}}} = 5.02\,\mathrm{TeV}$.

Chapter 5

Interaction of particles with matter

This chapter addresses the different types of interactions that particles can encounter with a given material which they travel through. For example, the particles created in a heavy-ion collision with a detector, which is set up surrounding the collision point.
When charged particles travel through a given material, they interact with the atomic electrons and nuclei. They can excite or ionize atoms when they scatter off electrons (depending on the amount of transferred energy). The mean energy loss per path length is described by the Bethe-Bloch formula for heavy, fast particles (e.g. charged pions). The released electrons can then cause further ionization if they have enough energy. Also, light (e.g. electrons) or very fast charged particles can lose energy via Bremsstrahlung when they are deccelerated in the Coulomb fields of atomic nuclei. The energy loss of electrons by Bremsstrahlung follows approximately the following relation:

$$E(x) = E_0 \mathrm{e}^{-\frac{\rho x}{X_0}} \tag{5.1}$$

The radiation length X_0 is given in units of g/cm^2 and indicates after which distance on a path through a material with a given density the energy is reduced by a factor 1/e. For decreasing electron energy, energy loss via Bremsstrahlung becomes less (and ionization more) important.
Photons, on the other hand, interact fundamentally differently. The possible interaction mechanisms are the photoelectric effect, Compton scattering, and pair production. The latter dominates over the other processes for photons with large energies E_γ, depending on the proton number Z of the traversed material (see Figure 5.1). While charged stable particles gradually lose energy in every interaction until they come to rest, for a photon this is not the case. Instead, we can only define a probability for a photon to still exist after it has traveled a certain length x through a material with a given density ρ, according to equation Equation 5.2, which describes the

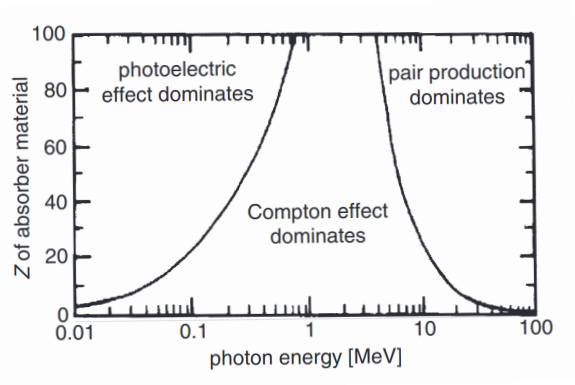

Figure 5.1: Interaction of photons with matter [130]. Dominance of different processes depending on the photon energy and the proton number Z of the material.

attenuation of a photon beam.

$$I(x) = I_0 \mathrm{e}^{-\mu\rho x} \tag{5.2}$$

μ is a characteristic property of the material in units of $^{\mathrm{cm}^2}/_{\mathrm{g}}$.
Pair production will be described in more detail in the following because will be of importance later in this thesis. In the Coulomb field of an atomic nucleus, which can acquire the generated momentum recoil $\vec{p}_{\mathrm{r}}$, a photon with momentum $\vec{p}_\gamma$ can convert into an electron-positron pair (with momenta $\vec{p}_{\mathrm{e}^+}$ and $\vec{p}_{\mathrm{e}^-}$).

$$\vec{p}_\gamma = \vec{p}_{\mathrm{e}^-} + \vec{p}_{\mathrm{e}^+} + \vec{p}_{\mathrm{r}} \tag{5.3}$$

Without the recoiling nucleus, it is impossible to satisfy energy and momentum conservation simultaneously. The photon energy is transformed into the fermion masses m_{e} and kinetic energies E_{e},

$$E_{\mathrm{e}^-} + E_{\mathrm{e}^+} = h\nu - 2m_{\mathrm{e}}c^2 \tag{5.4}$$

however, the electron mass is negligible compared to the photon energies which are relevant in this thesis. The kinetic energy transferred to the nucleus can be neglected due to its large mass.
The following relation holds for the opening angle θ_{o} between the electron and positron [130]:

$$\theta_{\mathrm{o}} \approx \frac{m_{\mathrm{e}}c^2}{E_\gamma}. \tag{5.5}$$

which means that electron and positron emerge almost parallel from the conversion of a highly energetic photon. For the latter, the cross section can be approximated by

$$\sigma_{\mathrm{pair}} = \frac{7A}{9N_{\mathrm{A}}X_0}, \tag{5.6}$$

where A and X_0 are the mass number and the previously mentioned radiation length of the traversed material, and N_{A} the Avogadro constant.

Chapter 6

The ALICE experiment

6.1 The Large Hadron Collider

The Large Hadron Collider (LHC) is a synchrotron-type circular particle accelerator with a circumference of 27 km, located near Geneva. It accelerates bunches of either protons or heavy-ions in two parallel beam pipes, in opposite directions. Experiments are located at four interaction points, where the beams cross and the particle bunches collide. In Pb–Pb running mode, almost 600 bunches circulate in each direction, which contain 70 million $^{208}_{82}\mathrm{Pb}^{82+}$ ions each. During the lifetime of the beam of several hours, the number of particles per bunch decreases due to the loss of ions in collisions.
The beam pipes are surrounded by superconducting dipole magnets which bend the particle trajectories to keep them on their circular path (see Figure 6.1). They are contained in a cryogenic tunnel, which is cooled down to a temperature of 1.9 K. Inside, an ultrahigh vacuum has to be maintained. The beams are focussed by quadrupole and higher multipole magnets.
In order to prepare the lead ion beam, a lead sample is heated and a small

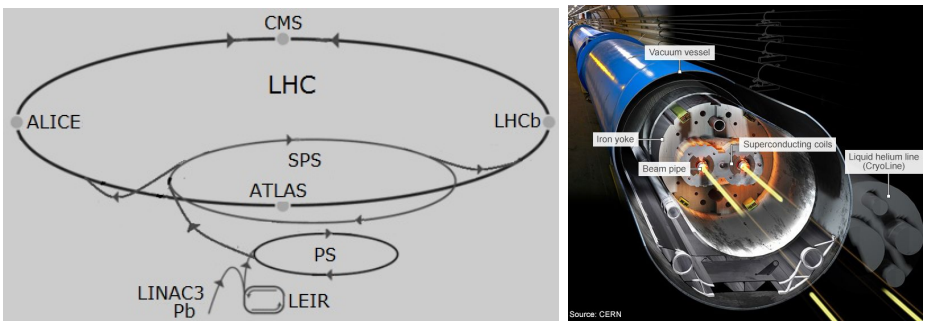

Figure 6.1: Left: Schematic drawing of the LHC and the pre-acceleration stages for ions. [131] **Right:** Cross section through the cryogenic tunnel of the LHC.

amount of atoms is vaporized. After they have been stripped from some of their electrons, the ions are gradually accelerated and further stripped in the linear accelerator LINAC3, the Low Energy Ion Ring (LEIR), Proton Synchrotron (PS) and Super Proton Synchrotron (SPS), as shown in Figure 6.1, before they are injected into the LHC, where they are accelerated to their final speed by means of radiofrequency cavities. The maximum center-of-mass energy in Pb–Pb collisions per nucleon-nucleon pair is $\sqrt{s_{\mathrm{NN}}} = 5\,\mathrm{TeV}$, in proton-proton collisions up to $\sqrt{s} = 13\,\mathrm{TeV}$ were reached.

6.2 The ALICE detector

ALICE is an acronym, which stands for A Large Ion Collider Experiment. As the name suggests, the experiment is specialized in studying heavy-ion collisions. It was designed to be able to cope with the large particle densities arising in Pb–Pb, compared to those in pp collisions. It is situated at one of the four interaction points of the LHC, where collisions of ions, as well as protons, take place.

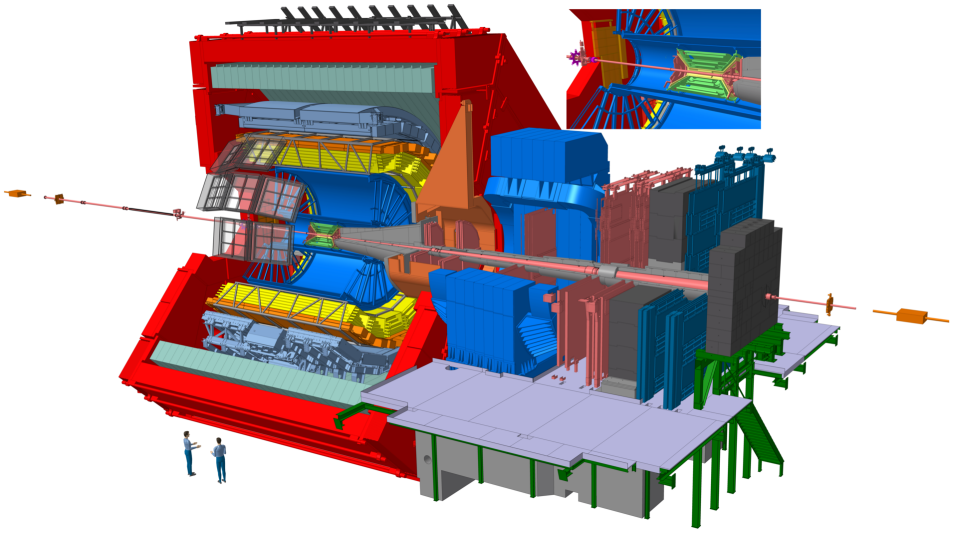

Figure 6.2: Schematic drawing of the ALICE detector and its components [132].

A schematic drawing of ALICE and its subdetectors is shown in Figure 6.2. The whole apparatus is 26 m long and 16 m in diameter [133]. A right-handed cartesian coordinate system with its origin at the interaction point and its z-axis along the beamline is used to describe points and vectors in the ALICE detector volume. In the central barrel part of the experiment (at mid-rapidity), the detector components are arranged in cylindrical layers around the LHC beam pipe, centered at the interaction point. Each subdetector serves a specific purpose and provides complementary information,

that is acquired during the passage of particles, which are created in the collisions. The central barrel is contained in a solenoid magnet (red color in Figure 6.2), which provides a 0.5 T magnetic field, oriented parallel to the beam direction. It causes charged particles to move on curved trajectories in the x-y-plane according to their momentum and charge. The charged particle tracking in ALICE is performed by the Inner Tracking System ITS (green in Figure 6.2), the Time Projection Chamber TPC (blue), Transition Radiation Detector TRD (yellow) and time-of-flight detector TOF (orange) [134]. The subdetectors which are relevant for the analysis presented in this thesis are described in the following paragraphs.

ITS

The Inner Tracking System ITS [135] is the innermost detector component, placed at radii R between 3.9 cm and 43 cm. It consists of six layers based on different technologies: two Silicon Pixel Detectors (SPD), two Silicon Drift Detectors (SDD), and two Silicon Strip Detectors (SSD). Their working principle is based on the creation of electron-hole pairs in silicon diodes by ionizing particles and segmented readout chips which detect the electrical signal and deliver the position of the interaction. The ITS is used for track reconstruction and especially the vertex reconstruction benefits from the good spatial resolution of the SPD.

TPC

The Time Projection Chamber [136] is a cylindrical detector in the central barrel, which covers the pseudorapidity range $|\eta| < 0.9$. It is placed around the ITS, at radii $85 < R < 247$ cm. During the analyzed data-taking period, it was filled with an Ar–CO_2 (88–12) gas mixture. Charged particles ionize the gas along their trajectory. A high voltage electrode at the axial center (in z-direction), electrodes at the endplates, and a field cage at the inner and outer surface (in radial direction) provide a uniform electric field, which causes the ionization electrons to drift in z-direction with a constant velocity v_{drift} towards the endplates of the TPC (shown in Figure 6.3). Here, the arrival locations in the x-y-plane and the arrival times are measured, so that the location of the initial ionization (x and y directly and z via v_{drift} and the collision time) can be derived. The working principle is based on the multi-wire proportional chamber (MWPC) technique with pad readout. The ionized electrons travel until they reach a plane of parallel anode wires. On their way, they produce further electron-ion pairs, especially when they are close to the anode wires, where the electric field is strong enough to initiate electron avalanches. The positive charges are collected by the surrounding electrodes. Until collection, the moving charges induce currents in the pad plane, which is two-dimensionally segmented into pixels, allowing to determine the position in x and y. The TPC is used for track reconstruction and particle identification based on the specific energy loss of particles.

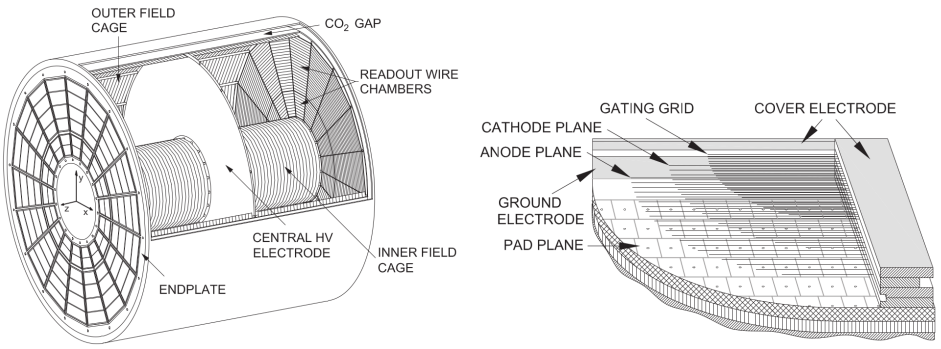

Figure 6.3: Left: Schematic drawing of the TPC field cage with its central electrode and readout chambers **Right:** Closer view of a readout chamber showing the pad plane and wire planes [136].

V0, T0, and ZDC

The V0 detectors are two arrays of scintillation counters, placed close to the beamline on either side of the interaction point. V0A in the pseudorapidity range $2.8 < \eta < 5.1$ and a longitudinal position of $z = 329\,\text{cm}$ and V0C at $-3.7 < \eta < -1.7$ and $z = -88\,\text{cm}$ [133]. They have a good time resolution better than 1 ns and are used for triggering. The V0 detector is also used to determine the collision centrality. In addition, background events that are not due to beam-beam collisions but interactions of one beam with residual gas molecules in the beampipe can be rejected when comparing V0A and V0C signal times.

The T0 consists of two Cherenkov detector arrays T0A and T0C on either side of the interaction point and has a time resolution of 20-25 ps in Pb–Pb collisions [134]. It is used to determine the collision time, which can vary by a few hundred ps within one bunch crossing [134].

The ZDC detectors are hadronic sampling calorimeters placed at a distance of $z = 113\,\text{m}$ on both sides of the interaction point [134] in order to detect spectator nucleons. In the dataset used for this work, they are used to reject background events from collisions between ions out of the main bunches.

TOF

The time-of-flight detector (TOF, orange in Figure 6.2) consists of Multi-gap Resistive Plate Chambers (MRPC). It is positioned at radii $370 < R < 399\,\text{cm}$ from the beam axis, covers the full azimuth and the pseudorapidity range $|\eta| < 0.9$. These fast ionization detectors measure the arrival time of a particle and therefore its velocity. The time has to be evaluated relative to the time of the collision, which is measured by the T0 detector. The intrinsic time resolution of TOF is 80 ps [134]. Together with the measured momentum of tracks found also in the TPC (and ITS) the mass of the particle is

determined and therefore the particle species can be identified. In addition, TOF provides additional space points for the reconstruction of tracks.

TRD

The Transition Radiation Detector TRD [137] (yellow in Figure 6.2) was designed for electron identification, tracking, and triggering. In the analysis described in this work it is used mainly for calibrating the distortions caused by space charges in the TPC (see also Section 6.4 and [138] for more details). Its working principle is based on ionization by charged particles and transition radiation (TR). The TRD is placed between TPC and TOF, at radii between 290 and 368 cm from the beam. It covers the full ϕ range and the pseudorapidity window $|\eta| < 0.84$. In ϕ-direction it is segmented in 18 sectors, in z-direction in 5 stacks and in radial direction in 6 layers. One layer consists of a radiator made from Polypropylene fiber and Rohacell foam, where the TR is generated, a drift region filled with a xenon-based gas mixture, and an MWPC-based readout chamber. When charged particles travel through the gas, they deposit energy via ionization. In addition, the radiator which contains many boundaries between media with different dielectric constants, causes highly relativistic particles ($\beta\gamma > 800$ for the installed radiator [137]) to produce transition radiation. The TR photons deposit a large amount of energy at the entrance of the gas chamber. This characteristic signal is seen only for electrons because heavier paricles don't reach the $\beta\gamma$ threshold in ALICE. The TRD contributes also to track reconstruction. Clusters are reconstructed from signals in the segmented readout pad plane and sampled in time bins of 100 ns. From these, local track segments (tracklets) can be reconstructed within each TRD chamber. A TRD track can be composed of up to 6 tracklets, one from each layer.

Photon detection

As described before, the dominant interaction mechanism of high-energy photons with matter is pair production. Ionization of the TPC gas or the silicon diodes, like for charged particles, does not take place. Therefore, photons are invisible to the tracking system. In ALICE, photons can be detected directly by the electromagnetic calorimeters EMCal/DCal (Di-Jet Calorimeter) [139][140] and PHOS (Photon Spectrometer) [141][142] and indirectly with the Photon Conversion Method (PCM).

EMCal and PHOS

The probability for pair production depends on the density of the traversed material. However, the tracking detectors are designed to contain as little material as possible, in order to minimize the scattering of charged particles which distorts their trajectories. Many of the generated photons have not converted until they reach the calorimeters which are placed beyond the TOF detector. The working principle of the calorimeters is based on electro-

magnetic showers, the interplay of photon conversions in a dense material, and Bremsstrahlung of electrons. Electrons also initiate showers and can be distinguished from photons on the basis of matching tracks. The calorimeters measure the energy of the incoming particle, which is fully absorbed. The energy resolution improves for increasing particle energy because the number of interactions, which are detected, increases.
The EMCal is a sampling calorimeter (Pb-scintillator layers) placed at a radius of $R = 4.3\,\mathrm{m}$ over a range of $80^\circ < \varphi < 187^\circ$. The covered pseudorapidity window is $|\eta| < 0.7$. It has a larger acceptance than PHOS, a homogeneous calorimeter made out of $PbWO_4$ crystals. The latter is located at a radius of $R = 4.6\,\mathrm{m}$ over a range of $250^\circ < \varphi < 320^\circ$ and $|\eta| < 0.12$. It is characterized by a finer cell granularity ($\approx 2.2 \times 2.2\,\mathrm{cm}^2$) than EMCal ($\approx 6 \times 6\,\mathrm{cm}^2$). DCal is an addendum with the same design as EMCal, covering $260^\circ < \varphi < 327^\circ$. It was installed between LHC run 1 and run 2 for measuring di-jets.

Photon Conversion Method
The Photon Conversion Method (PCM) is complementing the capabilities of the calorimeters to reconstruct photons. As mentioned, a photon can convert to an electron-positron pair in the detector material before the calorimeters as well. If the conversion takes place well before the outer radius of the TPC, the electron and positron, being ionizing charged particles, can be detected via tracking. The required track reconstruction will be described in Section 6.4 and the PCM is discussed further in Section 7.1. Figure 6.4 shows the distribution of conversion coordinates. Most conversions take place in the TPC containment vessels, the ITS layers and support structures, and the beam pipe. According to the material budget of the ALICE detector, 8% of all photons have converted within $R_{\mathrm{conv}} < 180\,\mathrm{cm}$. The ITS can complement the tracking, if a photon converts before the second layer of the SSD.

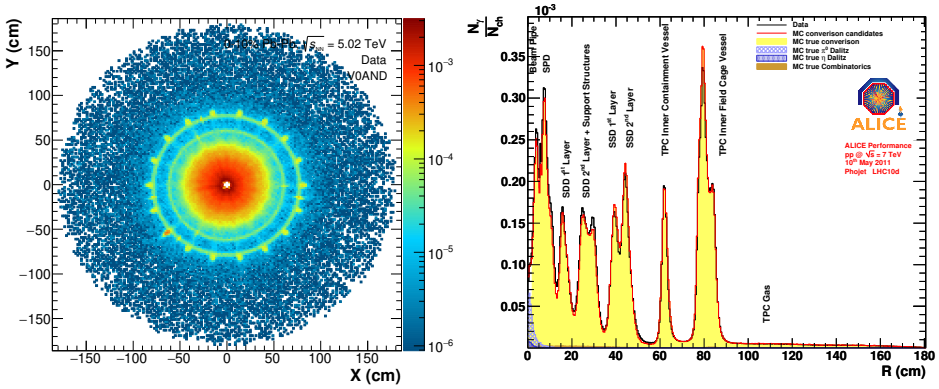

Figure 6.4: Left: X and Y distribution of conversion coordinates within the analyzed dataset. **Right:** Radial projection of conversion points, measured in pp collisions and compared to MC simulation. Different regions are labeled with the corresponding detector components [143].

6.3 Data taking

In the presented analysis, Pb–Pb collisions with a center of mass collision energy per nucleon-nucleon pair $\sqrt{s_{\mathrm{NN}}} = 5.02\,\mathrm{TeV}$ are analyzed. The dataset was recorded in November/December 2015, when the LHC provided ion beams with the highest energy for the first time. During the analyzed period, called LHC15o, up to 518 lead ion bunches per beam were circulating in the LHC with a time bunch spacing of 150 ns - 225 ns between them. This filling scheme results in a bunch crossing rate of about 6 MHz. However, on average a collision of two ions takes place only in about 1‰ of the bunch crossings. The actual collision rate in ALICE was about 6 kHz. As mentioned before, the maximum rate is achieved when a new beam is injected and decreases over time because the colliding ions are lost. During the LHC15o period, the beams were dumped followed by a new fill about 30 times. About 10% of the fills were injected with only 50 bunches per beam and delivered a lower collision rate of 50 Hz. The total delivered integrated luminosity at ALICE is $233\,\mu\mathrm{b}^{-1}$, which is 60 % more than in the previous $\sqrt{s_{\mathrm{NN}}} = 2.76\,\mathrm{TeV}$ dataset, which was recorded in 2011, before the long shutdown between LHC run 1 and run 2.
An inelastic collision of two ions is detected first by the trigger detectors, which initiate the data recording in the other detectors. In the analyzed minimum bias dataset, the trigger decision required a signal in both V0A and V0C detectors (V0AND) together with the beam crossing. Like this, a total number of 157 million events was recorded (compare also to Table 7.2).

6.4 Data reconstruction

The offline data processing is implemented based on the AliRoot software framework. It is used by the ALICE collaboration in the domains of reconstruction, calibration, analysis, and simulation, which will be described in the following sections. AliRoot is written with object-oriented programming techniques in C++ and uses classes and tools of the data analysis framework ROOT [144] for data storage, analysis, fitting, visualization, and unfolding. The large amount of required resources for storing and processing the ALICE data is provided by a distributed computing infrastructure called Grid [145], which connects many computing centers worldwide [133]. The interaction with the Grid is organized by the AliEn environment [146].
First, all steps of reconstructing the raw data, which are common to all physics analyses, like calibration, track and vertex reconstruction, are organized centrally and the output is saved in event summary data files (ESDs). In a second step, the information from ESDs is further processed, subjected to basic track quality cuts, and saved in a compressed format in analysis object data files (AODs). Further calibration is done based on the reconstructed data and is provided to the specific physics analyses in an offline analysis database (OADB). The physics analyses like the one described in this thesis are performed on the Grid as well, using the AODs as input. The output is further analyzed and visualized locally using ROOT and C++. All these steps are described in more detail in the following paragraphs.

Track and vertex reconstruction [134, 147]
Before the reconstruction of particle tracks starts, adjacent signals in space and time are grouped as clusters and their centers of gravity are determined. This is done in all detectors individually.
Afterward, a preliminary primary vertex (the coordinates of the collision) is reconstructed based on SPD tracklets. The latter are lines that connect a cluster in the outer layer of the SPD, one in the inner layer of the SPD, and the beam pipe. The point where most tracklets point to is identified as the primary vertex.
The Kalman filter (KF), a recursive data processing algorithm [148, 149] applied to track reconstruction [150] is used. It starts with previously determined seeds, finds tracks, and calculates their parameters and covariance matrix, while recursively adding more clusters. The parameters are the curvature radius, which determines the transverse momentum p_{T} and the position and angles with respect to the coordinate system. Seeds are determined in two different ways: either by two or three TPC clusters and with or without constraining the track to point to the preliminary primary vertex, in order to look for primary and secondary tracks respectively. The clusters are chosen from the outermost TPC radii, because the cluster density is minimal here. In general, the Kalman filter uses statistical methods

in every iteration to determine the best estimate and the uncertainty of the quantities of interest (here the track parameters), based on the seed or the previous iteration. When new information is added (in this context, the nearest cluster) the next iteration is started and the best estimate is updated, weighting with the uncertainties of the previous estimate and those of the current measurement (cluster). The KF is recursive in that sense that only the current best estimate and its uncertainty is stored after every iteration and all previous information does not need to be stored and reanalyzed. This algorithm runs from the outer to the inner TPC wall. Aftwerwards, matching ITS clusters are associated with the tracks. Then, the Kalman filter propagates the tracks back through ITS and TPC and adds TRD and TOF clusters to the tracks. In the final step, the tracks are refitted through all detectors until their distance of closest approach (dca) to the preliminary primary vertex. The p_{T} resolution is better than 1% [134] and the transverse dca resolution in Pb–Pb collisions is better than 300 μm for $p_{\mathrm{T}} > 0.2\,\mathrm{GeV/c}$ [134].
Finally, the final primary vertex can be determined from the reconstructed tracks. The resolution improves with respect to the preliminary SPD vertex, but both are better than 1 mm [134].

TPC space charge distortions
The electric drift field in the TPC can be distorted due to the accumulated space charge. In the analyzed dataset, the measured clusters were shifted by up to 5 cm in the x-y-plane due to this effect. Therefore, the measured TPC clusters are corrected in an additional time-dependent calibration step [138]. For this purpose, tracks from the surrounding detectors ITS, TRD and TOF are interpolated and provide reference positions for the TPC clusters. Within small volumes, the deviations are averaged over a time window of 40 minutes, which provides a correction map for the distortions.

$\mathrm{V_0}$ finder
Secondary vertices are identified using the $\mathrm{V_0}$ finder algorithm, which is described in the following. It can reconstruct secondary vertices due to neutral particle decays like K^0_{s} and Λ or photon conversions, using the emerging tracks. It is used for the photon conversion method. Figure 6.5 shows a sketch of a $\mathrm{V_0}$ topology and an event display with conversion candidates. First, all secondary tracks are selected by choosing only those with a large distance of closest approach b to the primary vertex. Then, pairs with opposite charge and a small distance of closest approach DCA to each other are chosen. The secondary vertex position is obtained at the point where the two tracks meet. The on-the-fly $\mathrm{V_0}$ finder, which runs during the track reconstruction process, refits the track parameters based on the identified secondary vertex, using the cluster information. The particle candidate which decayed or converted at this point is called $\mathrm{V_0}$. Its momentum $\vec{P}_{\mathrm{V_0}}$ and spa-

tial coordinates are calculated from the track properties with an algorithm (AliKF) based on the Kalman filter [151]. This algorithm also provides a quality measurement $\chi^2_{\text{red}} = \chi^2/\text{ndf}$, which quantifies how well the decay topology can be fitted consistently with the photon conversion hypothesis, i.e. assuming a massless mother particle and therefore small opening angle of the tracks. A cut on the angle $\theta_{\text{point}} = \measuredangle(\vec{P}_{\text{V}_0}, \vec{R}_{\text{V}_0})$ between the vector $\vec{R}_{\text{V}_0}$, which points from the primary to the secondary vertex, and the momentum is used to reduce the number of random combinations within the V_0 sample.

Particle identification in the TPC

In a proportional chamber like the MWPCs in the TPC, the measured signal is proportional to the deposited energy in the gas. Therefore, after the track has been reconstructed and the trajectory length, which is projected onto the pad plane, is known, the energy loss per track length, the specific ionization loss $\text{d}E/\text{d}x$, of the initially traversing particle can be measured. The distribution of $\text{d}E/\text{d}x$ is plotted versus the particle momentum for all tracks of a given dataset in Figure 6.6. The $\text{d}E/\text{d}x$ resolution is 6.5 % in most central Pb-Pb collisions [134]. A parametrization is generated according to the Bethe-Bloch formula for each particle species s, so that the specific energy loss of a track can be compared to the expectation for a given momentum. The deviation is then expressed in number of standard deviations $n\sigma_{\text{s}}$. The fact that the measured $\text{d}E/\text{d}x$ value can depend on the pseudorapidity η of the track and the particle multiplicity of the event is considered. However, for parts of the analyzed dataset no multiplicity correction could be implemented. In addition, the η distributions of the V_0 tracks differ from those that are used to calculate the parametrizations.
Therefore an additional recalibration step is necessary for this analysis. All available V_0 tracks are subdivided into bins of track momentum, η and

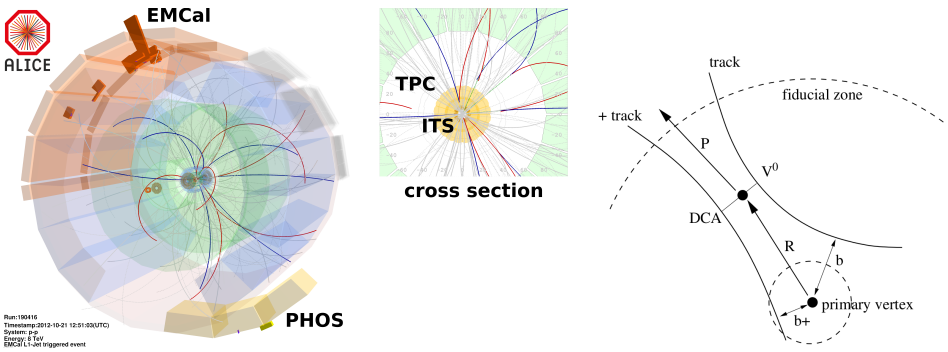

Figure 6.5: Left: Event display with conversion candidates. Blue and red lines depict oppositely charged tracks emerging from a common secondary vertex. **Middle:** Closer view of the x-y-plane. **Right:** Sketch of the V_0 finder algorithm [147]

conversion radius. One histogram for each bin is filled with the corresponding $n\sigma_{\mathrm{s}}$ values. Then, the electron peak is fitted with a gaussian and the deviation of the mean with respect to the expectation of 0 is determined (illustrated in Figure 6.6) and saved in correction maps in the OADB. During further analysis, the $n\sigma_{\mathrm{s}}$ value is corrected accordingly.

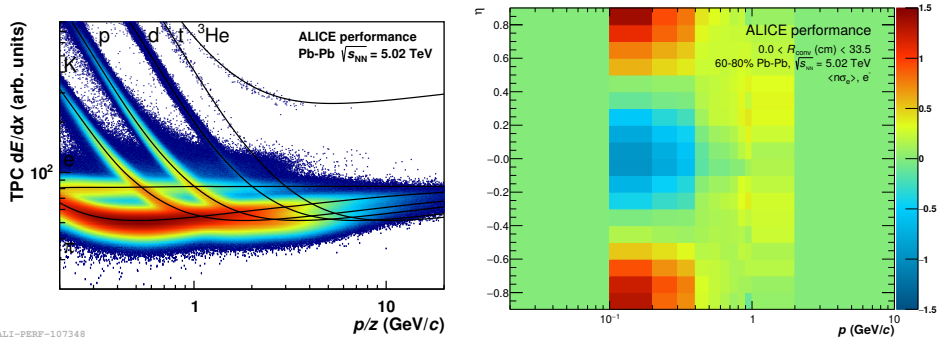

Figure 6.6: Left: TPC $\mathrm{d}E/\mathrm{d}x$ with Bethe-Bloch parametrizations for different particle species in Pb–Pb low interaction rate runs [152]. **Right:** Correction map for one R bin of one centrality class, which was manually created within this thesis. The color illustrates the value of $n\sigma_{\mathrm{e}}$ in each bin before recalibration (see text for more details).

Particle identification in the TOF

For PID with the TOF detector, the arrival time of a particle in the TOF modules is measured relative to the time of the collision, and compared to the expectation for the different particle species, as a function of p_{T}. The performance in Pb–Pb collisions is shown in Figure 6.7.

Centrality determination

The Pb–Pb data is analyzed in event classes of collision centrality. A class is described in terms of $c_1 - c_2\%$ most central collisions, where c is a percentile of the full hadronic cross section. The smaller the value c, the more central the collision and the larger the overlap between the nuclei. The impact parameter b denotes the distance of the centers of the two nuclei to each other during the collision. Central events are characterized by a small impact parameter, which is large for peripheral events. It can reach up to twice the radius of the nucleus. The centrality is determined using the track multiplicity registered by the V0 detectors. It is proportional to the total number of produced particles, which is assumed to decrease monotonically with increasing impact parameter [154]. A more detailed description can be found in [154] and [65]. The blue points in Figure 6.8 show the distribution of the summed V0A and V0C signal (V0M) in the analyzed dataset. The red line is a fit based on the Glauber [155, 156] model and the negative binomial distribution (NBD) [157]. The Glauber Monte Carlo simulation relates the

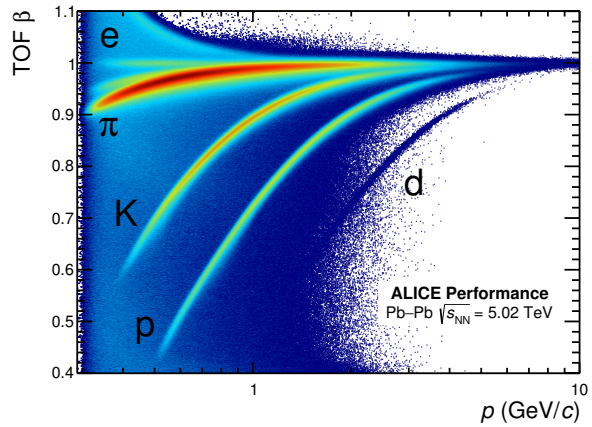

Figure 6.7: Particle identification with the TOF detector [153]. For this figure, tracks from low intensity runs were selected inside the pseudorapidity region $|\eta| < 0.5$. Furthermore, tracks with more than one matchable cluster in the TOF detector have been discarded in order to reduce the contamination from mismatched tracks, which is visible between the bands from electrons, pions, kaons, protons and deuterium.

impact parameter of a (simulated) collision to the number of participating nucleons N_{part} and the number of binary nucleon-nucleon collisions N_{coll}. It treats the nucleus-nucleus collision as independent nucleon-nucleon collisions, by which the nucleons are not deflected. This is justified by their large momentum. How many particles are produced according to N_{part} and N_{coll} is parametrized by the NBD $P_{\mu,k}(n)$, which determines the probability to measure n hits per ancestor (independently emitting sources of particles $N_{\mathrm{a}} = fN_{\mathrm{part}} + (1-f)N_{\mathrm{coll}}$) in the V0s. Afterward, centrality classes are assigned based on fractions of the integral of the V0M distribution. The geometrical properties $\langle N_{\mathrm{coll}}\rangle$,$\langle N_{\mathrm{part}}\rangle$ of this centrality class are then obtained from the Glauber MC. The centrality resolution is $< 2\,\%$ for $c < 80\,\%$ with V0M, which is better than the resolution which can be obtained with the ZDC or SPD multiplicity [134].

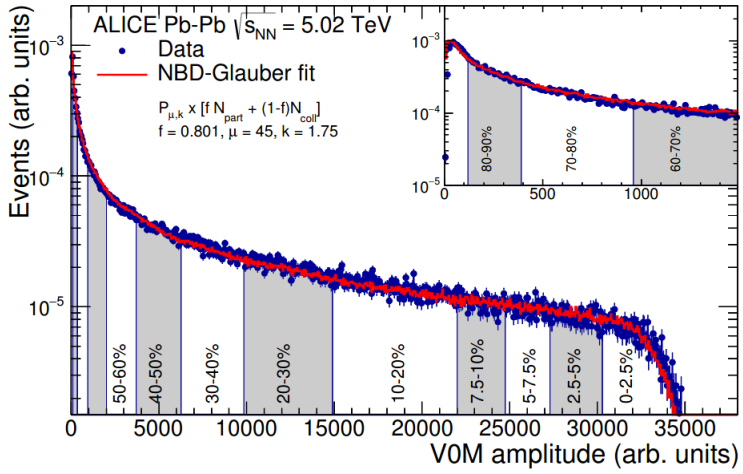

Figure 6.8: Distribution of V0M in all events of the analyzed dataset with NBD-Glauber fit and centrality classes [158].

6.5 Simulation

Monte Carlo simulations are widely used in data analyses. For example, detector acceptances and reconstruction efficiencies determined from MC are used to correct measured particle spectra. The simulation consists of the event generator and the detector simulation with GEANT [159]. To simulate AA collisions, the HIJING [160] generator is used.
For the analysis in this work, MC simulations with in total 28 million events are used. Some of them are produced with limits on the impact parameter b of the collision and some without (minimum bias). They are used together with the minimum bias productions for the respective analyzed centrality classes. A summary of the number of events in Data and MC in the different centrality classes can be found in Table 7.2.
In one MC production, additional π^0 and η mesons were inserted into each event. They are distributed uniformly with respect to pseudorapidity (within $-1.2 < \eta < 1.2$), azimuthal angle ϕ and transverse momentum p_{T} (within $0 < p_{\mathrm{T}} < 50\,\mathrm{GeV/c}$). The p_{T} distributions will be reweighted in order to match a physical distribution, as described in Chapter 7. The number of added mesons was chosen based on the impact parameter of the event, according to Equation 6.1, which is visualized in Figure 6.9, so that more particles are produced in central events than in peripheral events, like in data.

$$N(b) = 30 + 30\exp\Big(-\frac{1}{2}\Big(\frac{b}{5.12}\Big)^2\Big) \tag{6.1}$$

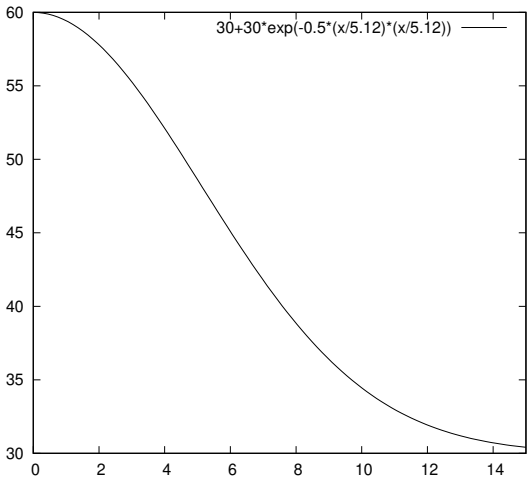

Figure 6.9: Number of added mesons in MC as a function of the impact parameter b.

Chapter 7

Measurement of the light neutral mesons π^0 and η

We measure the neutral mesons π^0 and η via their decays to two photons. Due to these electromagnetic decays of the lightest mesons, they have a very short decay length, which makes a direct measurement impossible. The branching ratios $\mathscr{BR}$ of these processes are listed in Table 7.1.
The measurement method will be discussed in the following sections, afterward the obtained results will be presented in section 7.6.

decay	$\mathscr{BR}$	**meson mass**
$\pi^0 \to \gamma\gamma$	$(98.82 \pm 0.03)\,\%$	$(134.9766 \pm 0.0006)\,\mathrm{MeV}$
$\eta \to \gamma\gamma$	$(39.41 \pm 0.20)\,\%$	$(547.862 \pm 0.018)\,\mathrm{MeV}$

Table 7.1: Branching ratios of considered decay channels and particle masses [161]

7.1 Event and photon selection for PCM

The analyses of neutral mesons and direct photons, which are presented in the following chapters, are based on PCM. As described before, in this method, we measure photons by reconstructing the tracks of their conversion products. First, the on-the-fly V_0 finder algorithm is used to identify secondary vertices, as described in Section 6.4. Afterward, the conversion point is recalculated, using the additional constraint that the track momenta must be parallel at this point due to the vanishing opening angle between electron and positron. This procedure is described in [162]. The V_0 sample contains mostly photons, K^0_s, Λ and $\bar{\Lambda}$, and combinatorial background consisting of random track pairs. Therefore, we apply selection cuts on the V_0 sample and the associated tracks to maximize the fraction of photons in the sample. They will be described in this section, after the following paragraph

on the event selection cuts that are used in this work.

Event selection

The set of triggered events (see section 6.3) is subjected to further selections in order to ensure a good quality of the dataset. First of all, it was checked that all relevant detectors (ITS, TPC, V0, ZDC) were functional and showed normal behavior. In addition, background events are rejected based on the timing information from ZDC and V0. Furthermore, only events with the collision vertex z position within $|z_{vtx}| < 10\,\text{cm}$ are used to prevent that the acceptance and reconstruction efficiency differs too much among the events. Because both collision rate and the probability that two collisions occur within one bunch crossing are small in Pb–Pb collisions, compared to those in pp collisions, complications due to pile-up (when the detector has to cope with more than one collision event at the same time) are less frequent. The average time between two collisions is of the order $100\,\mu\text{s}$. This is of the same order of magnitude as the TPC drift time ($92\,\mu\text{s}$), which limits the duration of the readout of one event. Therefore the pile-up probability is low but not negligible. To identify pile-up events, the V0 signal is compared to the number of tracks at the outer edge of the TPC. They should be clearly

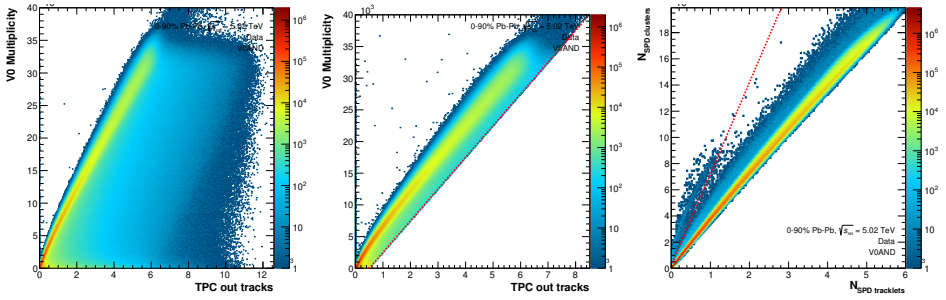

Figure 7.1: Signal in the V0 detector vs. number of tracks at the outer edge of the TPC **Left:** before the cut in Equation 7.1 and **Middle:** after the cut. The color scale illustrates the number of events in each bin. **Right:** SPC clusters vs. tracklets before the cut in Equation 7.2, which is drawn as red line.

correlated. But if the TPC track multiplicity is disproportionately larger than the V0 multiplicity in one event, it is identified as pile-up event and discarded [163]. We keep events that satisfy the condition

$$V0M > -2500 + 5N_{\text{TPC tracks}} \tag{7.1}$$

which is illustrated in Figure 7.1. In previous analyses of neutral mesons and direct photons in Pb–Pb collisions, the contribution of pile-up was rejected on a statistical basis by analyzing the distance of closest approach (dca) of the ee tracks (associated with the photon candidates) to the primary vertex *in beam-direction*. This method was prone to error because it

depended on the subjective fitting of the pile-up background dca distribution by eye. (see for example [164]). In this work, for the first time for this kind of analysis, pile-up was rejected on an event basis, so that no further correction was needed. Remaining machine-induced background is rejected based on the correlation between SPD clusters and SPD tracklets. In contrast to particles coming from collision events, particles from background events move through the detector rather parallel to the beam pipe. Therefore, only random combinations of clusters can be reconstructed as tracklets. If the number of clusters is very high, this can work but still the number of tracklets will be lower in a background event than in a collision event. We keep only events on the diagonal which satisfy

$$N_{\text{SPD clusters}} < 200 + 7N_{\text{SPD tracklets}}. \tag{7.2}$$

The resulting number of good events for analysis is summarized in Table 7.2.

	good events [10^6] **in centrality classes** [%]					
dataset	0-10	0-20	20-40	40-60	60-80	0-80
Low IR pass3						
High IR pass1 pidfix						
High IR pass1						
total data	10	20	20	20	20	80
LHC18e1,a,b,c						10
LHC16h4						2
LHC16i1a,b,c						9
LHC16i[2,3]a,b,c,						7
total MC	1.9	2.7	5.7	9.4	9.7	28

Table 7.2: Statistics of data and MC productions in classes of collision centrality after event selection. The data was recorded in three different subsets, having different interaction rates (IR) and reconstruction passes. The MC production with added π^0 and η mesons, mentioned in section 6.5, is LHC16h4.

Photon selection

In order to select the photons from the V_0 finder output, we use the TPC PID (see section 6.4) to enhance the fraction of electrons and positrons among all tracks, which contains also many pions and protons. We discard tracks with a $\mathrm{d}E/\mathrm{d}x$ value which deviates by more than 3σ from the electron parametrization and those which are too close to the pion hypothesis. The pion rejection is only applied in the p_{T} region where the pion and electron bands do not overlap. This way one accepts a lower purity of the electron sample in order to not lose too much statistics. Only tracks and photon candidates within the TPC acceptance $|\eta| < 0.9$ are used for the analysis. Tracks with $p_{\mathrm{T}} < 0.05\,\mathrm{GeV/c}$ are rejected because a good track-finding effi-

ciency cannot be guaranteed. To ensure a good track quality, we also require that 60 % of possible clusters, accounting for the track length in the TPC and the number of crossed pad rows, must be reconstructed and associated to the track.

The MC information in Figure 6.4 reveals that at small conversion radii,

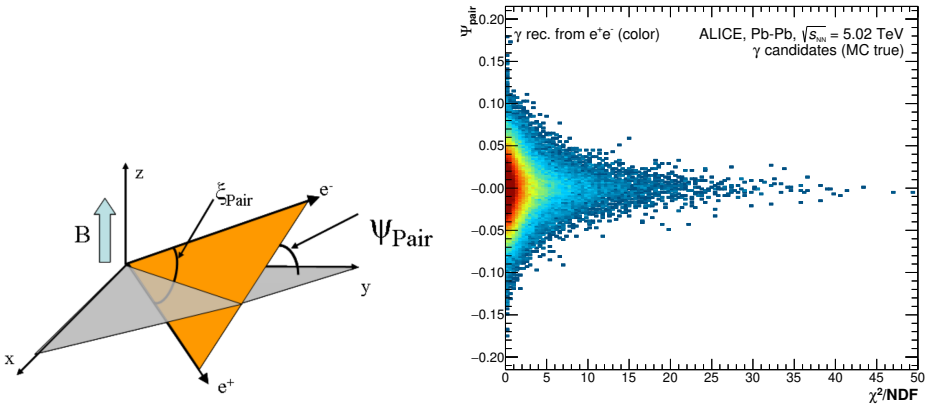

Figure 7.2: Left: Sketch of how ψ_{pair} is determined [165] **Right:** Distribution of ψ_{pair} vs χ^2/NDF of true conversion photons in MC, in the 0-10% centrality class.

many photons come from Dalitz decays $\pi^0 \rightarrow \gamma e^+e^-$ because of the short lifetime and thus range of the π^0 . Therefore conversions with $R_{\text{conv}} < 5\,\text{cm}$ are excluded as well.

Another measure to remove Dalitz decays, but also other decays and combinatorial background is a cut on the angle between the plane of the e^+e^- pair and the XY-plane, which is called ψ_{pair} . The separation power of this cut has to do with the fact that the conversion daughters of the massless photon have a very small intrinsic opening angle, whereas the decay daughters of the π^0 from the Dalitz decay can have random, non-zero opening angles [165].

In order to further reduce the contamination from kaon and lambda decays, we use the Armenteros-Podolanski method introduced in [166]. In the q_{T} vs α distribution of V_0s, photons are well separated from heavier particles. The quantity q_{T} is small due to the small opening angle and α is randomly distributed because of the equal masses of the daughter particles. In addition, we apply a p_{T} dependent $q_{\text{T, max}}$ cut as shown in Figure 7.3.

$$q_{\text{T}} = \frac{|\vec{p}_{\text{e}} \times \vec{p}_{\text{V}_0}|}{|\vec{p}_{\text{V}_0}|}, \quad q_{\text{L}} = \frac{|\vec{p}_{\text{e}} \cdot \vec{p}_{\text{V}_0}|}{|\vec{p}_{\text{V}_0}|}, \quad \alpha = \frac{q_{\text{L}}^{\text{e}^+} - q_{\text{L}}^{\text{e}^-}}{q_{\text{L}}^{\text{e}^+} + q_{\text{L}}^{\text{e}^-}} \tag{7.3}$$

All cuts are summarized in Table 7.3.

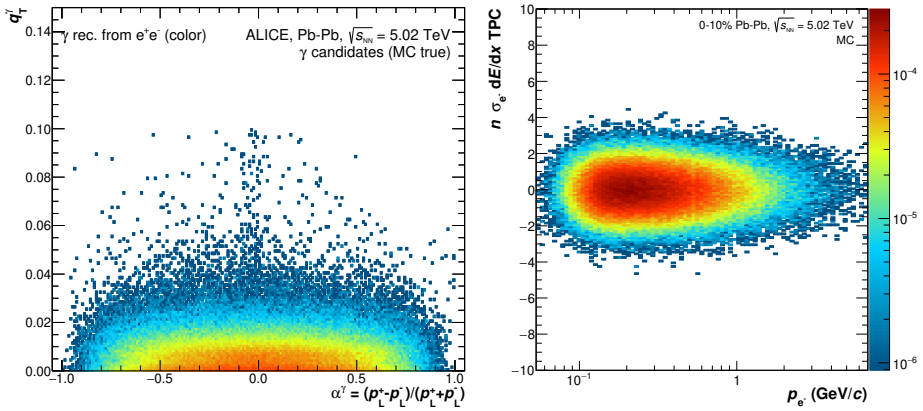

Figure 7.3: Left: Distribution of q_{T} vs α of MC true conversion photons and **Right:** TPC dE/dx nσ_{e} of true electrons from conversions.

Event selection	
Trigger	INT7 = $V0A$ && $V0C$
Centrality	$V0M$ estimator, $0 < c < 90\%$
Vertex	$\lvert z_{\mathrm{vtx}}\rvert < 10$ cm and $\geqslant 1$ contributing track
Pileup	$V0M > -2500 + 5N_{\mathrm{TPC\ tracks}}$
Background	$N_{\mathrm{SPD\ clusters}} < 200 + 7N_{\mathrm{SPD\ tracklets}}$
V$_0$ finder	
Distance to primary vertex	$b > 1$ mm
Distance to each other	DCA< 1.5 cm
Alignment of P and R	$\cos(\theta_{\mathrm{point}}) > 0.85$
Track selection	
Momentum	$p_{\mathrm{T}} > 0.05$ GeV/c
TPC cluster	$N_{\mathrm{TPC\ cluster}}/N_{\mathrm{reconstructible\ clusters}} > 0.6$
Acceptance	$\lvert\eta\rvert < 0.9$
Electron selection	-3 $< n\sigma_{\mathrm{e}} < 5$
Pion rejection	$n\sigma_{\pi} > 3$ for $0.4 < p < 2.0$ GeV/c and
	$n\sigma_{\pi} > 1$ for $p > 2.0$ GeV/c
Photon selection	
Acceptance	$\lvert\eta_{\mathrm{V_0}}\rvert < 0.9$
Conversion point	5 cm $< R_{\mathrm{conv}} <$ 180 cm
Alignment of P and R	$\cos(\theta_{\mathrm{point}}) > 0.85$
Photon quality	2D triangle cut with $\psi_{\mathrm{pair}} < 0.1$ and χ^2/NDF < 30
Armenteros-Podolanski	$(\alpha/\alpha_{\mathrm{max}})^2 + (q_T/q_{\mathrm{T,max}})^2 < 1$
	with $q_{\mathrm{T,\ max}} = 0.05$ GeV/cand $\alpha_{\mathrm{max}} = 0.95$

Table 7.3: Summary of cuts including those from the V$_0$ finder described in section 6.4. Accepted values are specified.

7.2 Lorentz-invariant yield

The quantity that we would like to measure first is the Lorentz-invariant yield of π^0 and η mesons, differential in y and p_{T}.

$$E\frac{\mathrm{d}^3N}{\mathrm{d}p^3} = \frac{\mathrm{d}^2N}{2\pi p_{\mathrm{T}}\mathrm{d}p_{\mathrm{T}}\mathrm{d}y} = \frac{N^{\mathrm{raw}}_{\mathrm{meson}} - N^{\mathrm{sec}}_{\mathrm{meson}}}{2\pi N_{\mathrm{ev}}\ \mathscr{B}\mathscr{R}\ \epsilon\ A\ p_{\mathrm{T}}\Delta p_{\mathrm{T}}\ \Delta y} \tag{7.4}$$

Here, N_{ev} is the number of analyzed collision events (see Table 7.2). How the raw yield $N^{\mathrm{raw}}_{\mathrm{meson}}$ is determined will be described in the next section 7.3. The corrections that have to be applied (secondaries $N^{\mathrm{sec}}_{\mathrm{meson}}$, detector acceptance A and reconstruction efficiency ϵ) in order to obtain the invariant yield are subject to the following section 7.4. The analysis is performed in p_{T} bins and their widths and centers enter as Δp_{T} and p_{T}. The considered range in rapidity is $\Delta y = 1.7$ ($|y| < 0.85$).

7.3 Invariant mass method

Photons are detected with the photon conversion method as described in previously. Meson candidates are constructed by pairing the available photons in all possible combinations. The energies and momenta of each of these hypothetical particles are calculated as

$$E = E_{\gamma_1} + E_{\gamma_2} \tag{7.5}$$

$$\vec{p} = \vec{p_{\gamma_1}} + \vec{p_{\gamma_1}} \tag{7.6}$$

from the energies and momenta of the two hypothetical daughter photons. The candidate list will naturally contain not only the real mesons but also a large background, mostly of combinatorial nature. Its removal will be discussed later in this chapter.
Several selection cuts, which are applied to the list of meson candidates are described in the following. The rapidity is calculated as

$$y = \frac{1}{2}\log\left(\frac{E + p_{\mathrm{z}}}{E - p_{\mathrm{z}}}\right) \tag{7.7}$$

Because of the limited acceptance of the detectors only candidates with rapidities $|y| < 0.85$ are used for analysis.

In addition, we cut on the asymmetry of photon energies

$$\alpha = \left|\frac{E_{\gamma_1} - E_{\gamma_2}}{E_{\gamma_1} + E_{\gamma_2}}\right| \tag{7.8}$$

in order to maximize the significance of the meson signal with respect to the combinatorial background [167] and therefore reduce the uncertainty on the background-subtracted signal.

$$\alpha < 0.65\ \tanh(1.8\,p_{\mathrm{T}}) \tag{7.9}$$

where p_{T} is the transverse momentum of the meson.
In the next step, we calculate the invariant mass of the remaining meson candidates using the photon energies E_{γ_1} and E_{γ_2} and the angle between the two photon momenta θ_{12} according to Equation 7.10 in bins of collision centrality and meson p_{T}.

$$M_{\gamma\gamma} = \sqrt{2E_{\gamma_1}E_{\gamma_2}(1-\cos\theta_{12})} \tag{7.10}$$

The black histograms in Figure 7.4 show the distribution of $M_{\gamma\gamma}$ in one

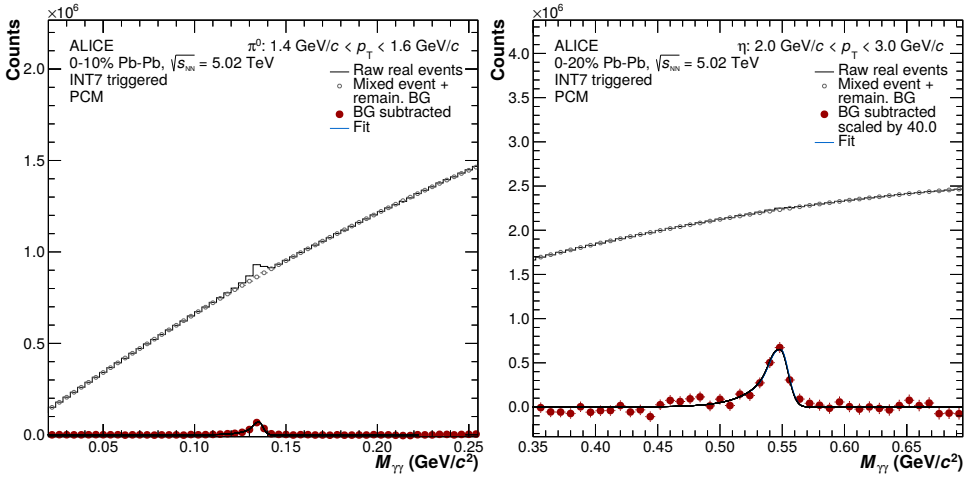

Figure 7.4: Invariant mass distributions in one p_{T} bin in most central events **left:** around the π^0 mass and **right:** around the η meson mass, scaled by a factor of 40. The black line shows the distribution before background subtraction and the red bullets afterward. The blue line is a fit with the function $A \cdot (g(M_{\gamma\gamma}) + e(M_{\gamma\gamma}))$ from Equation 7.13.

example bin around the π^0 mass and around the η meson mass (the particle masses are also listed in Table 7.1). As a next step, we estimate the aforementioned combinatorial background in order to subtract it from the measured distribution. To do so, we build another list of meson candidates, in the same way as described before but with taking γ_2 from a different event than γ_1 in order to ensure that these two photons cannot originate from the same meson decay or any other source of correlated photons. The two events are selected from different classes defined by the z coordinate of the primary vertex position or by the number of photon candidates in the event. Within this thesis, the invariant mass distributions of background meson candidates have been compared between the different classes. One example is shown in Figure 7.6. The investigation showed that the invariant mass distributions can differ by up to a few percent between the different classes in the same way in mixed and same events, and therefore confirmed that it is necessary to mix only events from the same class. The combinatorial background invariant mass distributions are normalized in order to

agree with the distributions of the actual meson candidates in a region on the right side of the peak in the respective centrality and p_{T} bin. After subtraction of this combinatorial background also small meson peaks become visible and we observe a remaining background, which could originate from other processes than meson decays in which at least two photons are produced in a correlated way. The function $f(M_{\gamma\gamma})$ (Equation 7.13) is fit-

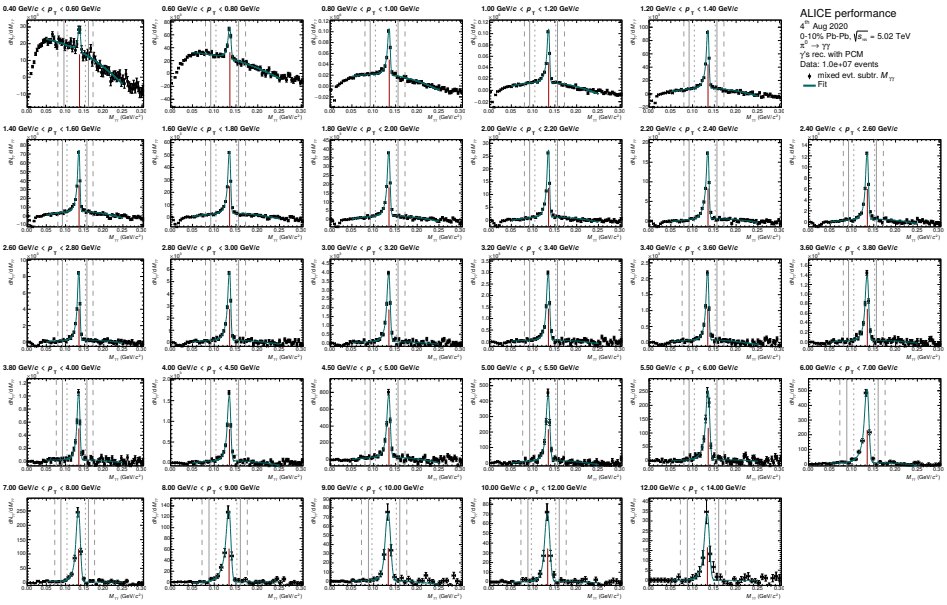

Figure 7.5: Invariant mass distributions around the π^0 mass after subtraction of combinatorial background in the 0-10% centrality class. The green lines are fits with the function $f(M_{\gamma\gamma})$ from Equation 7.13. The red vertical line indicates the π^0 mass. The grey lines mark the integration windows, as described in the text and Table 7.4. For other centrality classes see section A.1 and the distributions around the η meson mass section A.3.

ted to the remaining invariant mass distributions, in the ranges specified in Equation 7.11 and Equation 7.12, in order to 1) determine the peak position μ which defines the signal integration window and 2) determine the amount of remaining background $r_i(M_{\gamma\gamma})$.

$$\pi^0 \text{ fit range: } 0.05 \text{ GeV/c}^2 < M_{\gamma\gamma} < 0.25\,\text{GeV}/c^2 \tag{7.11}$$

$$\eta \text{ fit range: } 0.4 \text{ GeV/c}^2 < M_{\gamma\gamma} < 0.7\,\text{GeV}/c^2 \tag{7.12}$$

The function has 7 free parameters (A, μ, σ, λ, a, b, c). A is the amplitude of the peak, λ describes the shape of the exponential tail $e(M_{\gamma\gamma})$ on the left side of the peak, which arises because of the energy loss of the conversion

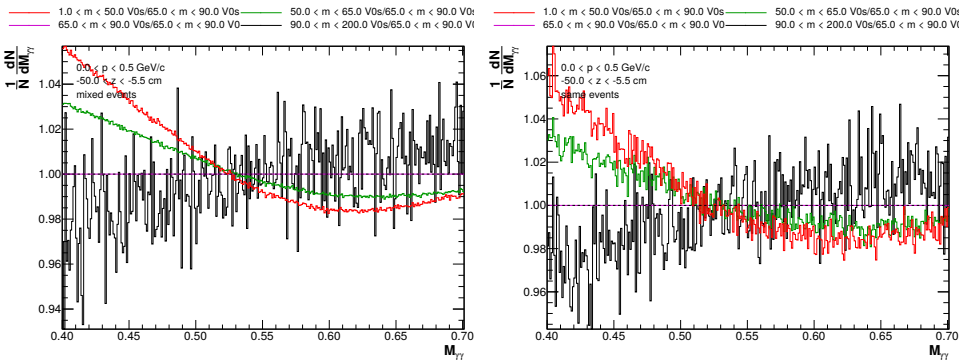

Figure 7.6: Ratios of invariant mass distributions in different multiplicity (m) classes of (**left:**) combinatorial background η candidates from mixed events and **right:** real η candidates from same events.

electrons and positrons due to Bremsstrahlung.

$$
\begin{aligned}
f(M_{\gamma\gamma}) &= A \cdot (g(M_{\gamma\gamma}) + e(M_{\gamma\gamma})) + r_i(M_{\gamma\gamma}) \\
g(M_{\gamma\gamma}) &= \exp\Big(-\frac{1}{2}\Big(\frac{M_{\gamma\gamma}-\mu}{\sigma}\Big)^2\Big) \\
e(M_{\gamma\gamma}) &= \exp\Big(\frac{M_{\gamma\gamma}-\mu}{\lambda}\Big) \cdot \Big(1 - g(M_{\gamma\gamma})\Big) \cdot \theta\Big(\mu - M_{\gamma\gamma}\Big) \\
r_1(M_{\gamma\gamma}) &= a + b \cdot M_{\gamma\gamma} \\
r_2(M_{\gamma\gamma}) &= a + b \cdot M_{\gamma\gamma} + c \cdot M_{\gamma\gamma}^2 \\
r_3(M_{\gamma\gamma}) &= a + b \cdot M_{\gamma\gamma} + c \cdot M_{\gamma\gamma}^2 + d \cdot M_{\gamma\gamma}^3
\end{aligned}
\tag{7.13}
$$

In this work, the necessity for remaining background fits with second-order polynomials (r_2 instead of r_1) was demonstrated for the analysis of π^0 in central Pb–Pb events. It is visible by eye in Figure 7.5 that especially in the region 1 GeV/c^2 $< p_{\mathrm{T}} <$ 2 GeV/c^2, the histogram cannot easily be fitted with a single linear function on both sides around the peak. However, it is difficult to determine which function fits best for describing the remaining background because the latter changes with $M_{\gamma\gamma}$ and consequently it is not possible to fit the background far away from the peak, where no signal is left. Therefore, this question was further studied with MC information as described in the following. Figure 7.7 shows the invariant mass distributions in data (black points), reconstructed π^0 from MC (blue), reconstructed and validated π^0 from MC (red), which does not contain any background. To obtain the MC background (green), the red histogram is subtracted from the blue one. Different functions are fitted to the MC background; linear (r_1), second (r_2) and third-order polynomial (r_3) in the range $0.02 < M_{\gamma\gamma} < 0.3$. It is visible by eye that a larger order polynomial than 1 is needed to describe the MC background. To make a quantitative statement, the χ^2/ndf values of the fits are compared to each other in Figure 7.8. Especially at low p_{T}, the

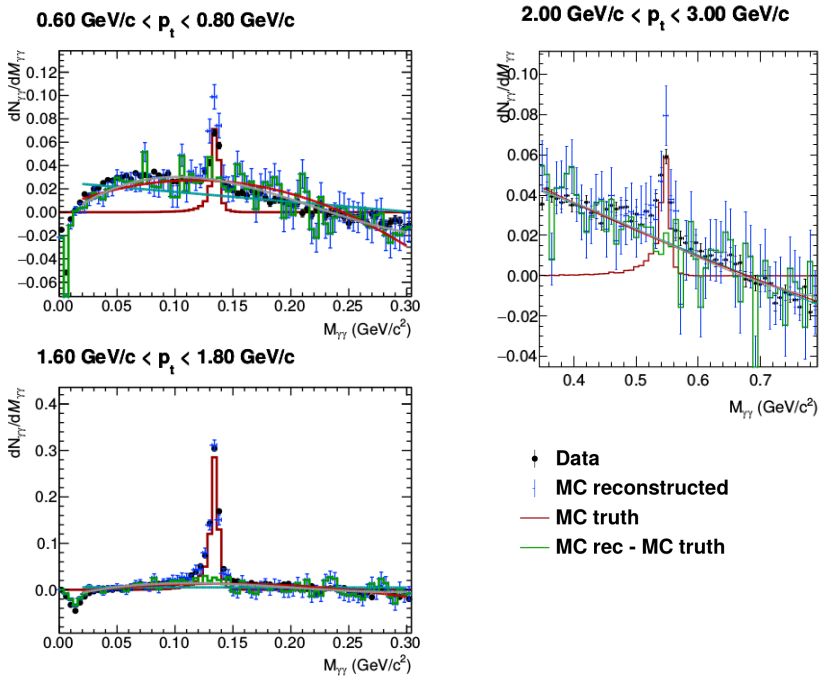

Figure 7.7: Invariant mass distributions around the π^0 mass (**left**) for two p_{T} bins and around the η meson mass (**right**). Mesons reconstructed from data, those reconstructed from MC and reconstructed and validated mesons from MC (MC truth) are shown. The functions r_1 (cyan), r_2 (red) and r_3 (grey) are fitted to the green histogram, which is the remaining background in MC.

χ^2/ndf values with r_2 and r_3 are smaller than those with r_1, which confirms that r_2 and r_3 are more suited than r_1 to describe the MC background. However, choosing a too high order might cause overfitting and removing part of the signal when only the background is supposed to be subtracted.

Furthermore, it was studied how well the $M_{\gamma\gamma}$ distribution *in data* can be described with fits including the different r_i contributions. A measure for that is if the fit results for the parameters μ, σ, and λ, which describe the actual signal, agree with those which are obtained when fitting the same function (without r_i) to true MC (reconstructed and validated MC). This comparison is shown in Figure 7.9. The parameters of the fit results are compared between data using r_1 or r_2 for the remaining background and true MC. in Figure 7.9. One can see that the second order polynomial fit parameter results agree well between data and true MC. In case a linear fit function is used for the remaining background, it is difficult to obtain matching results between data and MC for all parameters. In particular, the λ tail parameter deviates around $p_{\mathrm{T}} \approx 1\,\mathrm{GeV}/c$.

To use a higher-order polynomial function is more important in central than

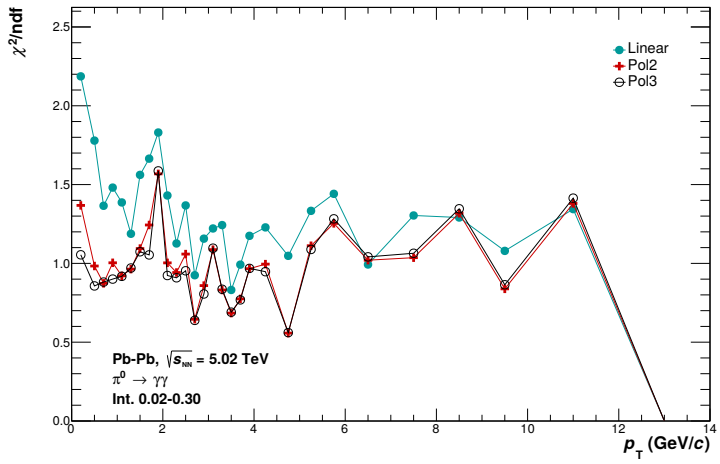

Figure 7.8: χ^2/ndf of fits to the MC background (see text and Figure 7.7) $M_{\gamma\gamma}$ distributions around the π^0 peak in 0-10% most central events, using different functions (linear = r_1, pol2 = r_2, pol3 = r_3) to describe the remaining background.

in peripheral events because in the latter, the remaining bachground is much smaller. Around the η meson mass, the remaining background has a different shape than around the π^0 mass. By eye, it looks linear (see Figure 7.7) and within the uncertainties it is not possible to make a quantitative statement on which r_i fits best.
To get the raw meson yield, the contents of all invariant mass bins within the solid vertical lines in Figure 7.5 are added up (see standard in Table 7.4, where μ is taken from the fit result, individually for each p_T bin). To subtract the remaining background, the part r_1 or r_2 of the fit function is integrated in the same range and this background is subtracted from the total integral. Executing this procedure for every p_T bin results in the raw meson yield $N^{\mathrm{raw}}_{\mathrm{meson}}$.

narrow		$0.030\,\mathrm{GeV}/c^2$		$0.015\,\mathrm{GeV}/c^2$
standard	μ_π -	$0.040\,\mathrm{GeV}/c^2$	$< M_{\gamma\gamma} < \mu_\pi$ +	$0.02\,\mathrm{GeV}/c^2$
wide		$0.055\,\mathrm{GeV}/c^2$		$0.035\,\mathrm{GeV}/c^2$
narrow		$0.06\,\mathrm{GeV}/c^2$		$0.02\,\mathrm{GeV}/c^2$
standard	μ_η -	$0.08\,\mathrm{GeV}/c^2$	$< M_{\gamma\gamma} < \mu_\eta$ +	$0.04\,\mathrm{GeV}/c^2$
wide		$0.10\,\mathrm{GeV}/c^2$		$0.06\,\mathrm{GeV}/c^2$

Table 7.4: Integration ranges for the invariant mass $M_{\gamma\gamma}$ histograms, where μ is the fit result for the (π^0 and η) peak position (top and bottom).

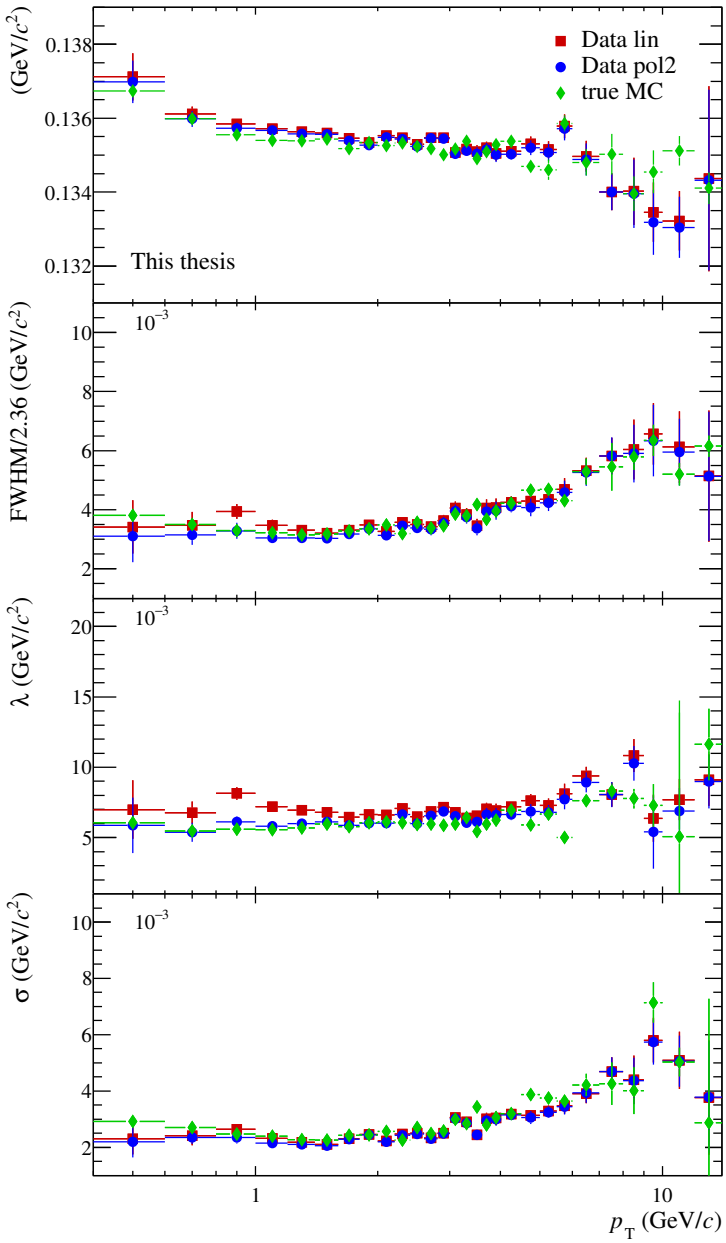

Figure 7.9: Parameters μ, FWHM, λ, and σ, obtained from fits of the invariant mass distributions around the π^0 mass, for the 0-10% centrality class. Comparison of fits with r_1 (red) and r_2 (blue) to data and fits to distributions from reconstructed and validated π^0 in MC (green).

7.4 Corrections

Secondaries

First, we subtract secondary pions $N^{\mathrm{sec}}_{\pi^0}$ from the full measured sample $N^{\mathrm{raw}}_{\pi^0}$. Primary particles include per definition also daughters of strong and electromagnetic decays. This definition is chosen (within ALICE) because within the common detector resolution it would not be possible to detect the mother particles because of their short decay lengths. For example, the measured π^0 spectra contain also those from $\eta \to 3\pi^0$ and other decays. Daughters of weak decays are considered as secondary particles and have to be excluded from the measurement. For example, if mother and daughter particles of a weak decay are charged and the daughter particle has a significant lifetime, there will be a kink in the observed tracks which indicates a decay topology. However, in our case, this method cannot be applied in order to check whether a π^0 originates for example from the decay $K^0_{\mathrm{s}} \to 2\pi^0$ because we detect the π^0 not directly (as it is neutral and decays immediately) and also the K^0_{s} is neutral. Therefore we have to estimate the number of neutral mesons from weak decays on a statistical basis.

To do so, hadrons with known π^0 decays are generated in a so-called cock-

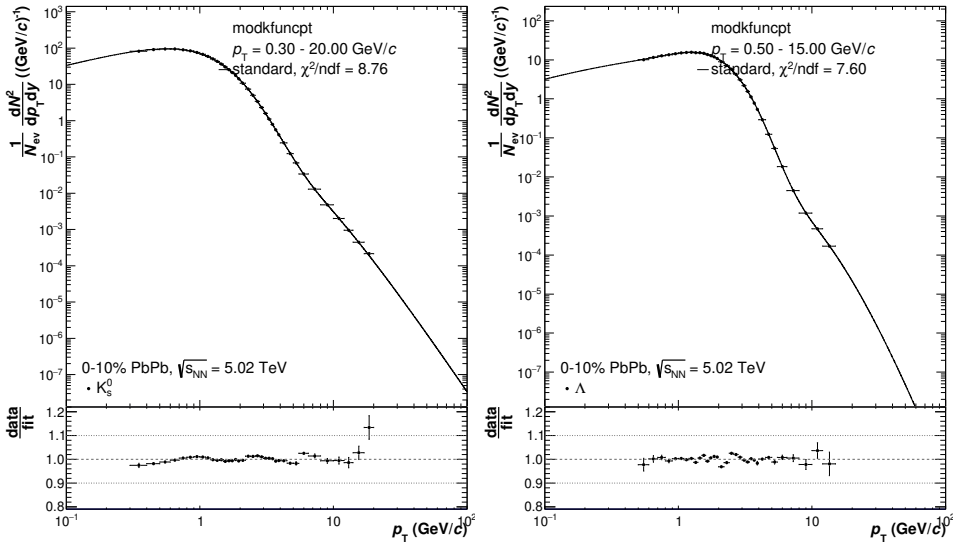

Figure 7.10: Parametrization of K^0_{S} and Λ spectra and the ratio data/parametrization in 0-10% most central events [168]. Other centrality classes are shown in Figure A.27.

tail simulation [169], according to parametrizations of their invariant yields, measured in the same collision system and energy. Afterward, the particle decays are simulated using branching ratios provided by the PDG [161] and as a result, we obtain the invariant yield of secondary π^0 . The most important sources of secondary π^0 are listed in Table 7.5. The spectra of K^0_{S} and Λ,

hadron	decays into	BR [%] to this mode [161]	measured via	$c\tau$	$1-e^{-<R>/c\tau}$
K^0_S	$2\pi^0$	30.69 ± 0.05	mesured [168]	2.68 cm	1
K^0_L	$3\pi^0$	19.52 ± 0.12	take K^0_S	15.34 m	0.0384
	$\pi^+ \pi^- \pi^0$	12.54 ± 0.05	param.		
Λ	$n\pi^0$	35.8 ± 0.5	measured [168]	7.89 cm	0.9995

Table 7.5: Considered hadrons with weak decays to π^0 in the cocktail simulation. Branching ratios and decay lengths $c\tau$ are listed as well. The last column shows the fraction which has decayed after the mean conversion radius $< R >= 60\,\text{cm}$.

measured by ALICE in Pb–Pb collisions at 5.02 TeV were parametrized, as shown in Figure 7.10. In the cocktail simulation, MC particles are generated with random azimuthal angle $0 < \phi < 2\pi$, a random rapidity $-1 < y < 1$ and a random transverse momentum $0 < p_\text{T} < 50\,\text{GeV/c}$. Afterward the p_T parametrizations are used to scale the generated mother particles accordingly. Decays are simulated using PYTHIA [170]. The π^0 which were produced in the considered rapidity range $|y| < 0.85$ are stored together with the information about their mother particle.
The last column in Table 7.5 shows that only 3.8% of the produced K^0_L have decayed after the mean conversion radius $< R >= 60\,\text{cm}$. Therefore we scale down the obtained secondary π^0 spectra from this particular source by this amount. Of K^0_s and Λ only a negligible fraction does not decay. Afterward, the secondary π^0 spectra are converted to raw yields ($N^\text{sec}_{\pi^0}$) with correction factors obtained from the detector simulation, in order to subtract them from the measured raw yields $N^\text{raw}_{\pi^0}$, because the correction factors in Equation 7.4 differ between primary and secondary photons. These factors are shown in Figure 7.11 and the resulting raw secondary yields, displayed in Figure 7.12, show that most secondary π^0 originate from K^0_S decays.

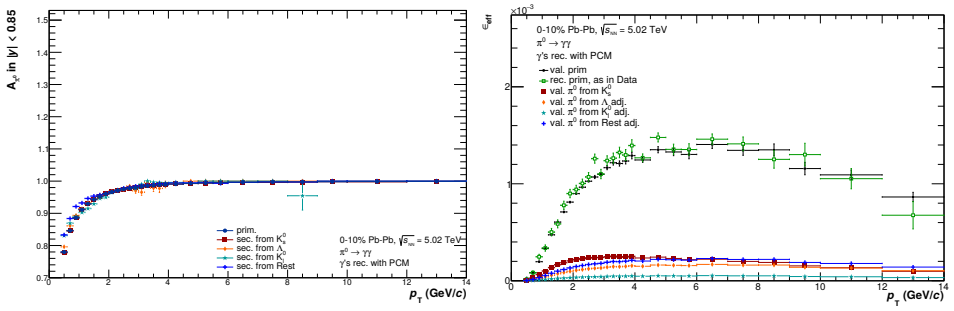

Figure 7.11: Correction factors (acceptance A and efficiency ϵ) from MC for primary and secondary π^0 from different contributions. The rest denotes those from interactions of particles with the detector material.

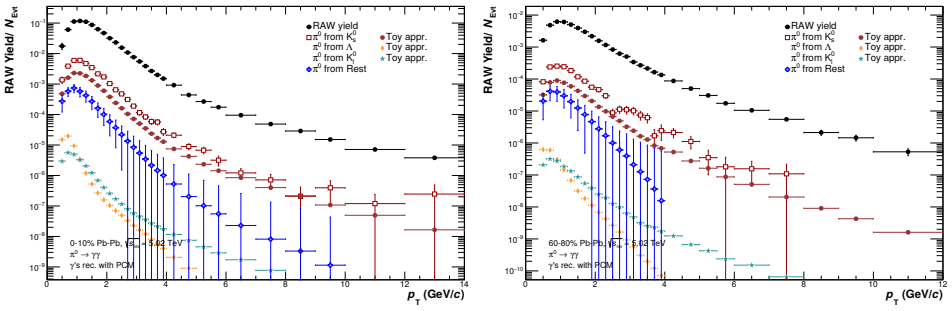

Figure 7.12: Raw yields of secondary π^0 from the different sources, for central and peripheral events. The rest denotes those from interactions of particles with the detector material. Calculated from the data-driven cocktail simulation (filled markers) and from the standard MC simulation relying on model-based particle generation (open markers).

Acceptance and efficiency

In order to determine the number of neutral mesons which have been produced in a collision in the rapidity region $|y| < 0.85$, we need to know how many of the generated particles enter our detectors and how many of those can be reconstructed. For this purpose, we calculate the detector acceptance A and neutral meson reconstruction efficiency ϵ from the normal MC simulation (with HIJING generator, not data-driven like the cocktail simulation). The acceptance is defined as follows:

$$A = \frac{\text{produced mesons in } \Delta\text{y and daughter } \gamma\text{'s in acceptance } |\eta| < 0.9}{\text{produced meson in } \Delta\text{y}} \tag{7.14}$$

In the denominator, we count all generated primary mesons that decay to two photons. In the numerator the condition that the daughters' rapidity is within the acceptance of the TPC has to be fulfilled in addition. The efficiency is defined as follows:

$$\epsilon = \frac{\text{correctly reconstructed mesons}}{\text{produced meson in } \Delta\text{y and daughter } \gamma\text{'s in acceptance } |\eta| < 0.9} \tag{7.15}$$

The denominator is identical to the numerator of the acceptance correction. The numerator counts all mesons after detector simulation, invariant mass analysis, and verification of the correct reconstruction. It takes into account that only part of the photons converts. The acceptance and efficiency corrections are shown in Figure 7.11 for π^0 and Figure 7.13 for η mesons.

p_{T} weighting

The goal of p_{T} weighting is to adjust the p_{T} distributions of mesons from the MC simulation to the ones in actual data. The difference can be seen in the top left panel of Figure 7.14. Here, the π^0 p_{T} spectrum from MC is

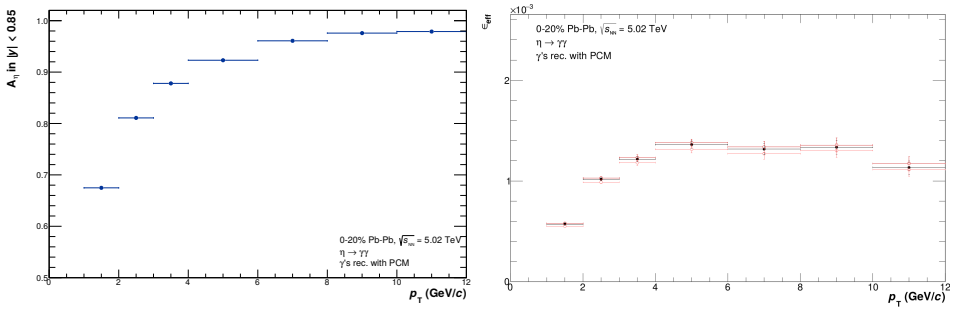

Figure 7.13: Acceptance and reconstruction efficiency for η mesons in central events. As a cross-check, the efficiency is calculated using the standard (black bullets), wide (red circles) and narrow (orange circles) integration ranges (Table 7.4). All reconstruction effciencies for all centrality classes and both mesons are compared in section A.7.

normalized like an invariant yield and plotted together with the spectrum from data. The latter is at this point corrected with an efficiency calculated from all MC productions, added particles rejected. Because the p_{T} distribution from added particles (which are produced flat in p_{T} on purpose) is very different from the one of regular MC particles (which should already now match the data distribution), they are plotted separately (red and green points). Then, the ratio between MC and a fit to data is calculated in every p_{T} bin of the spectrum, the result is shown in the right panel. The quality of the fit to data can be checked in the middle panel. This input for the weighting procedure is saved in a file, for π^0 and η meson, for all centrality classes and for all MC productions separately (even though for a better overview, all productions are merged for this figure). In the second step, during the next analysis train iteration, MC meson p_{T} histograms are filled weighted with this factor. Efficiencies from normal particles (ϵ_{MB}) and from added particles (ϵ_{AS}) are calculated separately and are merged afterward, taking into account the statistical uncertainties ($\Delta\epsilon_{\mathrm{MB}}$, $\Delta\epsilon_{\mathrm{AS}}$) as follows:

$$\epsilon = \frac{\epsilon_{\mathrm{MB}}}{(\Delta\epsilon_{\mathrm{MB}})^2} + \frac{\epsilon_{\mathrm{AS}}}{(\Delta\epsilon_{\mathrm{AS}})^2} \Bigg/ \frac{1}{(\Delta\epsilon_{\mathrm{MB}})^2} + \frac{1}{(\Delta\epsilon_{\mathrm{AS}})^2} \tag{7.16}$$

The result of the first iteration of p_{T} weighting can be seen in Figure the middle row of 7.14. The left panel shows the data yield corrected with the new merged efficiency from weighted MCs. The latter agrees with the fit (orange line) to the new corrected yield within statistical uncertainties. Adding another iteration, meaning weighting the MC to the corrected yield as determined after the first iteration, does not improve the agreement between MC and data anymore (comparing middle and bottom row of 7.14). The same procedure is done for the η meson as shown in Figure 7.15.

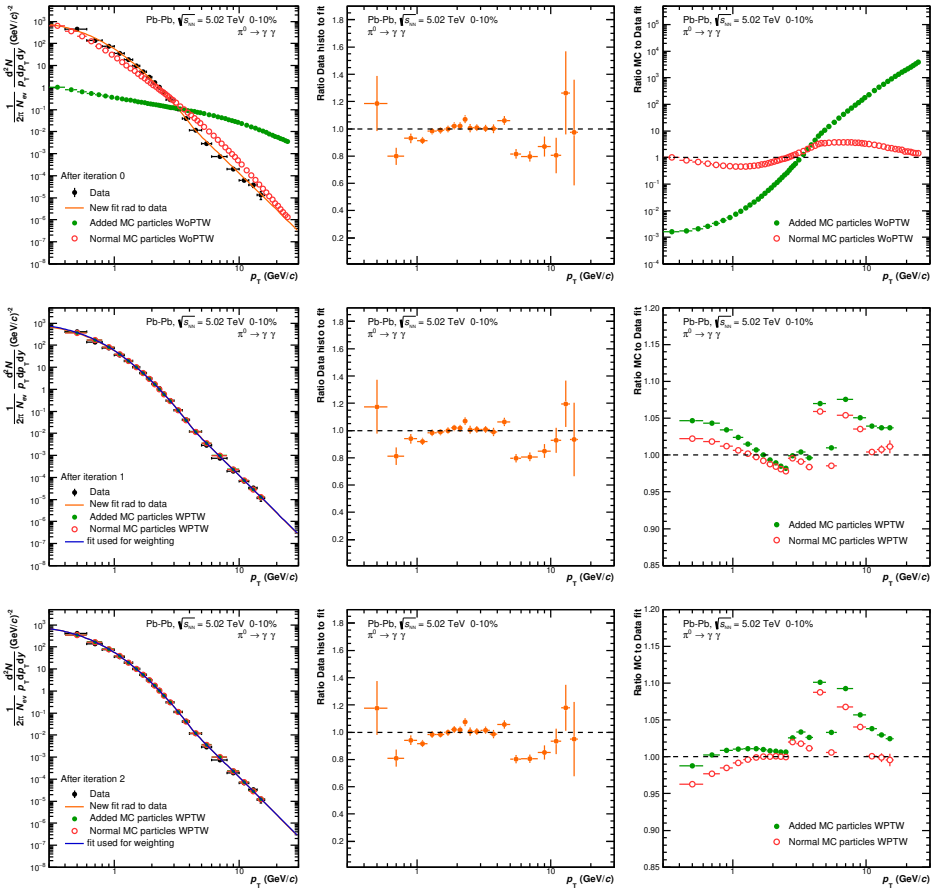

Figure 7.14: π^0 spectra **Top**: Before p_{T} weighting of MC **Middle**: after first and **Bottom**: after second iteration. **Left**: p_{T} spectra from data (with fit) and MC (Min Bias MC productions (red) and MC with added particles (green)). **Middle**: Ratio between data histogram and fit, demonstrating the quality of the fit. **Right**: Ratio between MC histograms and data fit, which are used as weights.

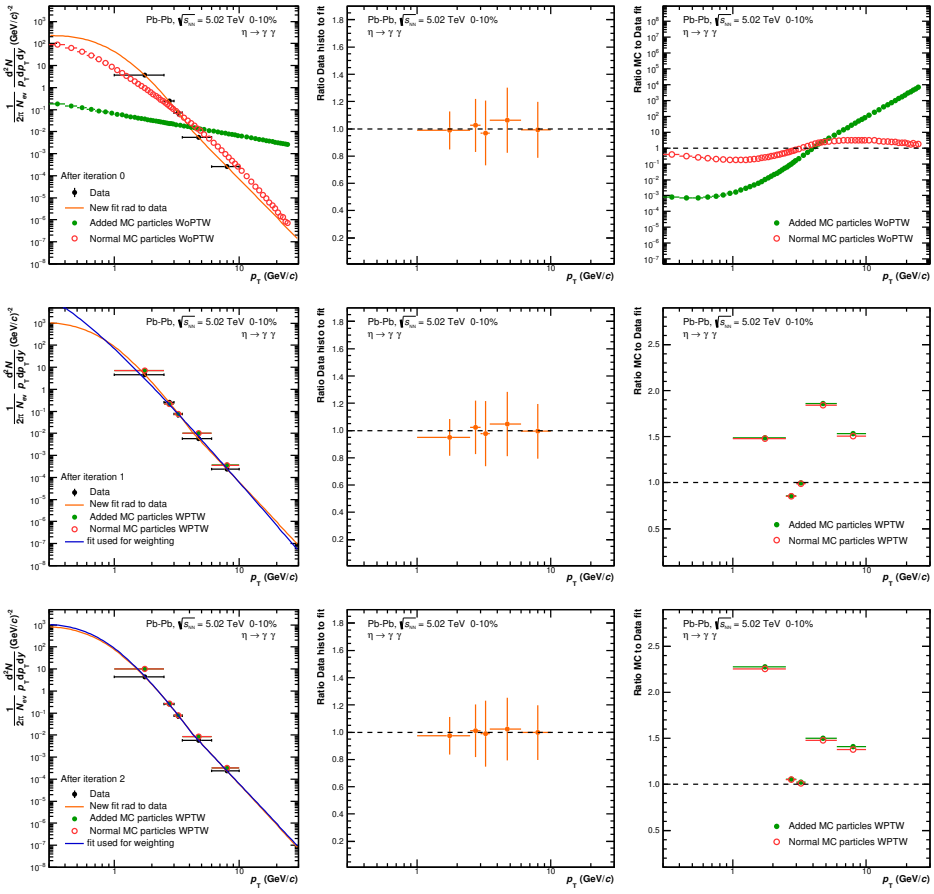

Figure 7.15: η meson spectra **Top**: Before p_{T} weighting of MC **Middle**: after first and **Bottom**: after second iteration. **Left**: p_{T} spectra from data (with fit) and MC (Min Bias MC productions (red) and MC with added particles (green)). **Middle**: Ratio between data histogram and fit, demonstrating the quality of the fit. **Right**: Ratio between MC histograms and data fit, which are used as weights.

7.5 Systematic uncertainties

As described in Section 7.1, photon and meson candidates are selected from the complete list of reconstructed ones, based on cut variables (Table 7.3 and Equation 7.9), which are suited to separate true photons and mesons from falsely reconstructed ones. A good agreement of these cut variables between data and MC simulation output is needed because the cuts strongly affect the efficiency, which is used to correct the data and which is calculated from MC simulations. As a result of an extensive quality assurance procedure, some portions of events were discarded completely because a good agreement could not be ensured. However, small differences between data and MC cannot be avoided. Therefore, every cut introduces a systematic uncertainty, which can be estimated by varying the cut values. The procedure is as follows: the value of one cut at a time was varied in a reasonable way (meaning not making an obvious error). If possible, one stricter and one looser cut was chosen. The invariant yield (here denoted as y) was calculated in the same way as with the standard cuts and the deviation between the two results was evaluated:

$$\Delta_{\mathrm{i}}(p_{\mathrm{T}}) = y_{\mathrm{v_i}}(p_{\mathrm{T}}) - y_{\mathrm{s}}(p_{\mathrm{T}}), \tag{7.17}$$

where s denotes the standard value of a cut and $\mathrm{v_i}$ the variation number i of the same cut. The mean of the absolute value of the deviations Δ_{i} was taken as systematic uncertainty. One further step was to assess whether the difference between standard and variation is significant or caused by variations due to the statistical uncertainty [171]. To do so, the statistical uncertainty of the deviation ($\sigma_{\Delta_{\mathrm{i}}}$) was calculated from the statistical uncertainties of the yield (σ_y):

$$\sigma_{\Delta_{\mathrm{i}}}(p_{\mathrm{T}}) = \sqrt{(\sigma_{y_{\mathrm{v_i}}}(p_{\mathrm{T}}))^2 - (\sigma_{y_{\mathrm{s}}}(p_{\mathrm{T}}))^2} \tag{7.18}$$

and if

$$\Delta_{\mathrm{i}}(p_{\mathrm{T}}) > \sigma_{\Delta_{\mathrm{i}}}(p_{\mathrm{T}}), \tag{7.19}$$

the deviation in that p_{T} bin was considered significant. This assessment was considered in the next step, the smoothing of the systematic uncertainties; Because large fluctuations of the systematic uncertainty as a function of p_{T} (see left panels of Figures 7.16, 7.17 and 7.18) are unphysical, polynomial functions that fit the data points are chosen. The criterion from Equation 7.19 is considered in these choices. For the final values of systematic uncertainties, these functions are evaluated at the p_{T} bin centers. The result is shown in the right panels of Figures 7.16, 7.17, and 7.18.
The complete aforementioned procedure was carried out for all applied track-, photon- and meson cuts. Afterward, the systematic uncertainties from all varied cuts was added quadratically for each p_{T} bin, together with the uncertainties arising from the material budget, the yield extraction, and the mass

resolution, which accounts for the fact that the invariant mass peak positions in data and MC differ. The material budget uncertainty is caused by the imperfect implementation of detector materials and geometry in GEANT; In the simulation of the passage of photons through the detector, the photon conversion probability strongly depends on the traversed material (just the same as in reality), which is implicitly included in the photon reconstruction efficiency. Therefore, an incorrect implementation of material in the simulation introduces an error in the efficiency and therefore also the measured spectra. The magnitude of this error was estimated in [172] to amount to 4.5% on single photon spectra and therefore $2 \times 4.5\% = 9\%$ on neutral meson spectra. Consequently, in this analysis an uncertainty of 9% is added to the systematic uncertainty of the π^0 and η spectra.

In order to estimate the uncertainty of the raw yield extraction procedure,

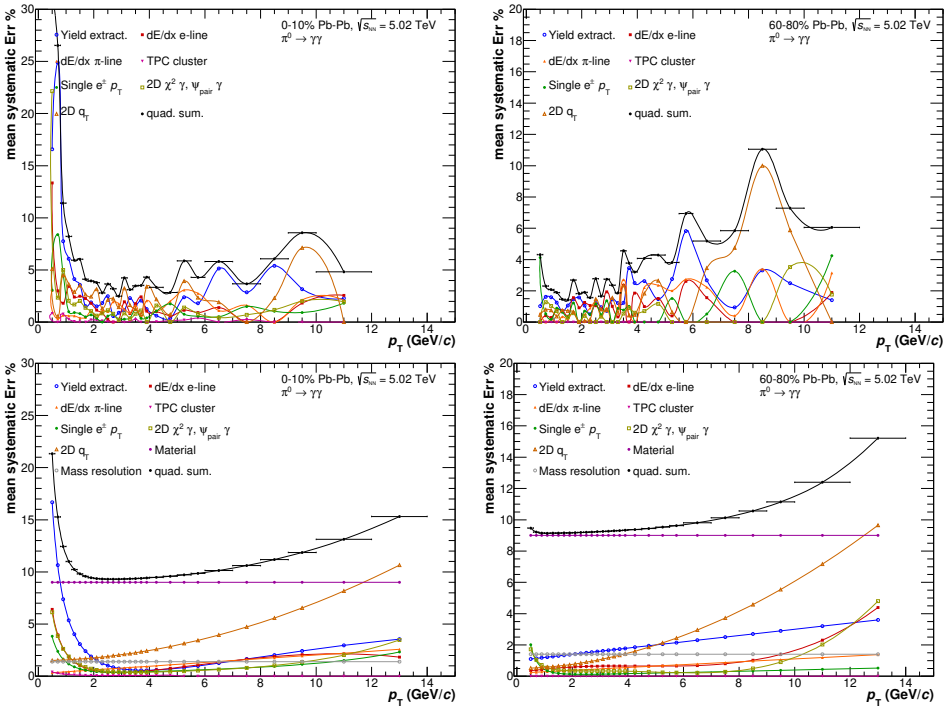

Figure 7.16: Systematic uncertainties of π^0 **Top:** Raw and **Bottom:** Smoothed, with material budget and mass resolution uncertainty and the quadratic sum of all contributions. The left figures show the 0-10% centrality class and the right figures 60-80%.

the integration range was varied (see Table 7.4 and the dashed lines in Figure 7.4 illustrate the variations). In addition, as described in Section 7.3, the combinatorial background invariant mass distributions are normalized in a region on the right side of the peak. The second variation which is

considered in the yield extraction uncertainty is to choose a region on the left side of the peak for the normalization. The uncertainty of the choice of fit function to the remaining background is implicitly included by the variation of integration window. When choosing an appropriate function, that uncertainty is small, when choosing an inappropriate function, it is larger.

Figures 7.16, 7.17 and 7.18 illustrate how the aforementioned procedure

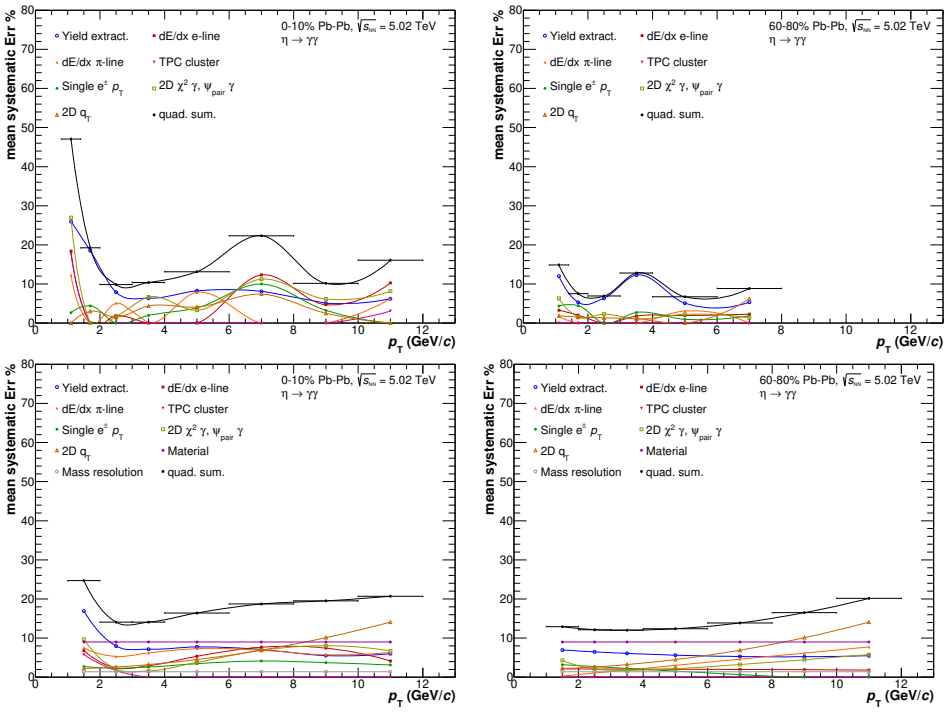

Figure 7.17: Systematic uncertainties of η **Top:** Raw and **Bottom:** Smoothed, with material budget and mass resolution uncertainty and the quadratic sum of all contributions. The left figures show the 0-10% centrality class and the right figures 60-80%.

was carried out in the centrality classes $(0-10)\,\%$ and $(60-80)\,\%$. The values for those in between were determined by linear interpolation. For the π^0 , the systematic uncertainty due to the material budget uncertainty is clearly dominating, whereas for the η meson it is of similar size as the other contributions. For the η/π^0 ratio, the material budget and mass resolution uncertainties cancel out. One can also see that the yield extraction uncertainty is one of the major sources of uncertainty. In central collisions, it gets especially large at low p_{T}, where the signal to background ratio gets worse, whereas in peripheral collisions this uncertainty increases in particular at high p_{T}, where one is running out of statistics (Faster than in central collisions). At low p_{T} the description of the remaining background in the in-

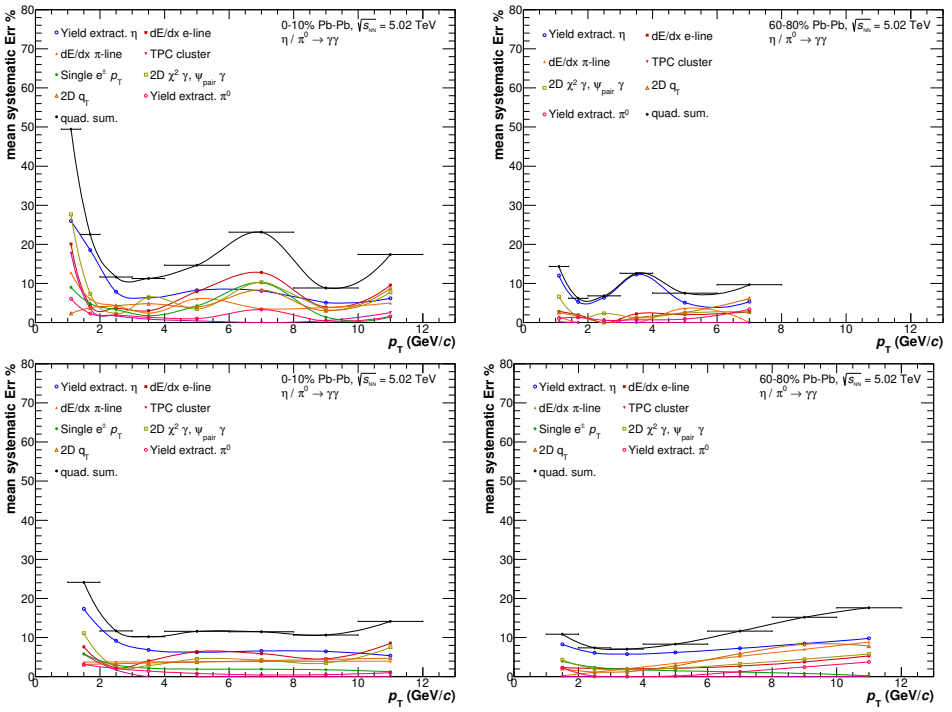

Figure 7.18: Systematic uncertainties of the η/π^0 ratio **Top:** Raw and **Bottom:** Smoothed, with the quadratic sum of all contributions (material budget and mass resolution uncertainties cancel in the ratio). The left figures show the 0-10% centrality class and the right figures 60-80%.

variant mass spectra (after subtracting the mixed event background) plays a crucial role. Compared to the statistical, the systematic uncertainty is dominating. Only in peripheral collisions at high p_{T} the statistical uncertainty is larger than the systematic uncertainty.

7.6 Neutral meson results

The measured fully corrected invariant yields, as defined in Equation 7.4, are shown in Figure 7.19 for different centrality classes, for the π^0 on the left and the η meson on the right. For comparison to theoretical calculations, data points are drawn to visualize the content of the histograms by using the method from [175]; When plotting a histogram containing counts which have been measured in extended bin ranges, according to a certain underlying, unknown, non-linear distribution, the best x (in this case p_{T}) value to plot a data point is not the bin center. Rather, the most accurate x value can be calculated from the expected functional form of the distribution. This introduces an uncertainty because the functional form is not

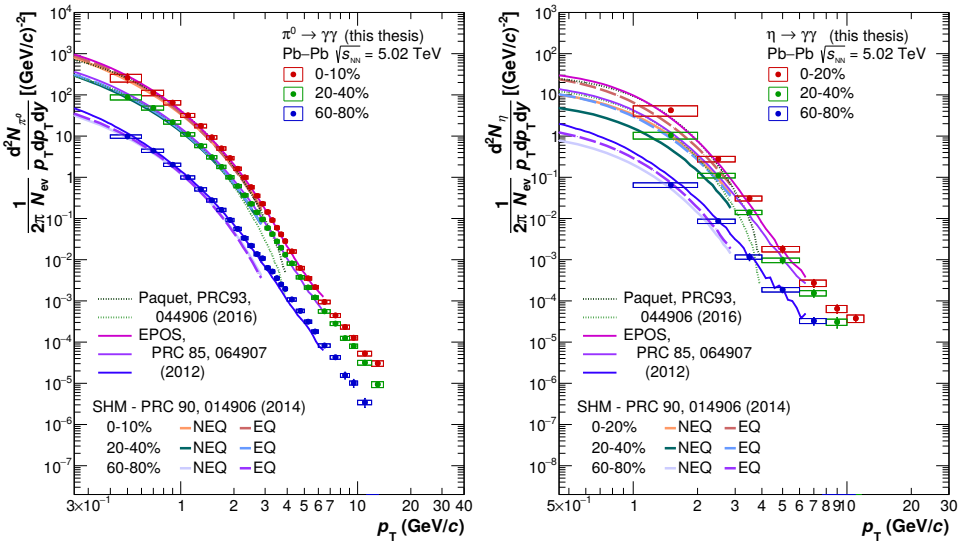

Figure 7.19: Invariant yields in different centrality classes. Vertical error bars indicate statistical uncertainties and the height of the boxes corresponds to the systematic uncertainties. The horizontal extension of the boxes indicate the bin widths. The meson yields N are counted within these bins and then divided by the bin widths Δp_{T}. The data is compared to calculations by J.-F. Paquet *et al.* [129], V. Begun *et al.* [173] and the EPOS model [174].

known before (it is what is supposed to be determined by the measurement), but this uncertainty can be smaller than the error one makes by plotting the point at the center or barycenter. Instead of shifting the x (p_{T}) value, one can shift the y (yield) value accordingly instead, while leaving the x value of the point unchanged, at the bin center. The latter approach was applied to the spectra for plotting as well as before calculating the R_{AA} and η/π^0 ratio.

The π^0 spectra are in good agreement with the calculations by V. Begun *et al.* [173], which focus on explaining effects that are relevant in the low p_{T} region. The calculations are based on a statistical hadronization model (SHM), the Cracow single-freeze-out model [176]. The time and size of the medium at freeze-out are parameters that have been fitted to measurements of charged pion and kaon spectra. A non-equilibrium version was developed in order to try to explain discrepancies of LHC measurements to the previous models, which could reproduce RHIC measurements well. This NEQ version is based on the sudden hadronization of the QGP [173]. The π^0 measurement does not favor one of them within the current uncertainties. Data and SHM differ between $2 < p_{\mathrm{T}} < 3\,\mathrm{GeV/c}$ in peripheral events. The spectra which were measured in central and semi-central events were also compared to calculations by Paquet *et al.* [129]. Here, a viscous hydrodynamics simulation with IP Glasma [110] initial conditions is used. The

results are in good agreement for $p_{\mathrm{T}} < 3\,\mathrm{GeV/c}$. Above that, the calculation is accompanied by significant theoretical uncertainties [177], which have not yet been estimated and therefore are not shown in the figure. The spectra that have been obtained from the EPOS model [174] are in good agreement with the data up to $p_{\mathrm{T}} = 6\,\mathrm{GeV/c}$ for all centrality classes and both mesons. In this approach, the medium, as well as jets and the interaction between the two, are modeled in order to obtain a good description in all p_{T} ranges. The calculation starts with flux tubes from initial collisions (hard scatterings and initial and final state radiation), which contribute to jets and the medium, depending on whether their energy is larger than their energy loss in the medium. The evolution of the medium is modeled with hydrodynamics. Viscosity is mimicked by choosing artificially large values for the radii of the flux tubes, which results in smoother distributions of the initial energy density in the transverse plane.

Figure 7.20 shows the ratio of the π^0 and η spectra. In the left panel, the

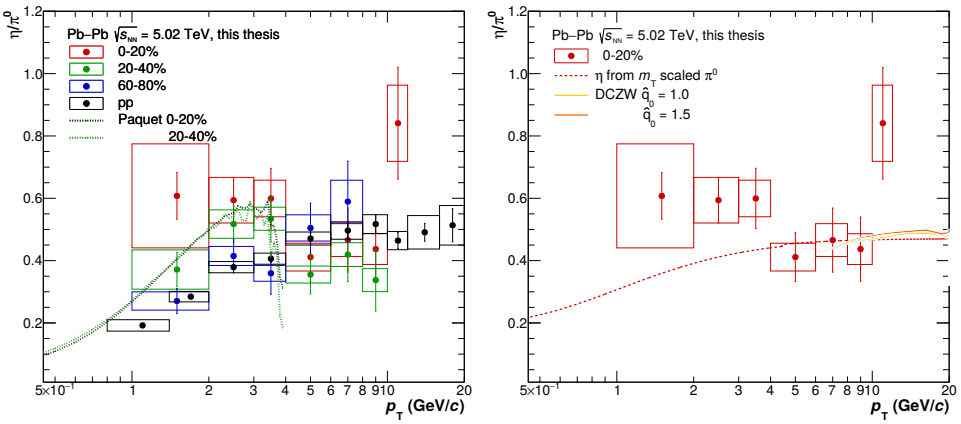

Figure 7.20: Left: η/π^0 ratio in different centrality classes compared to the ratio in pp collisions [178] and to calculations by Paquet *et al.* [129]. **Right:** η/π^0 ratio in 0-20% most central collisions, compared to m_{T}-scaling and calculations from the DCZW model [86] with two different initial values of the jet transport parameter $\hat{q}_0$.

different centrality classes are compared to each other and to the result from pp collisions [178] with the same center-of-mass collision energy. The calculation from Paquet *et al.* agrees up to 3 GeV with our measurement. As mentioned before, the calculation is accompanied by significant theoretical uncertainties for larger p_{T}. The right panel shows only the data from most central events compared to the expected curve in case m_{T}-scaling would hold (see also Equation 8.9). A deviation is seen especially in the region $2 < p_{\mathrm{T}} < 4\,\mathrm{GeV/c}$. The last point could also be a statistical fluctuation. In the DCZW model, medium-modified fragmentation functions are calculated from vacuum FFs for π^0 and η mesons, using the higher-twist approach

[86] in order to incorporate parton energy loss due to multiple scattering via gluon emission. The event-by-event CLVisc (ideal) (3+1)D hydrodynamics model from [179] is used to obtain the space-time evolution of the medium parameters like parton density and temperature. The comparison shows that the current η/π^0 ratio measurement is not yet sensitive to the jet transport coefficient $\hat{q}$.

In Figure 7.21 the nuclear modification factors of π^0 and η mesons are

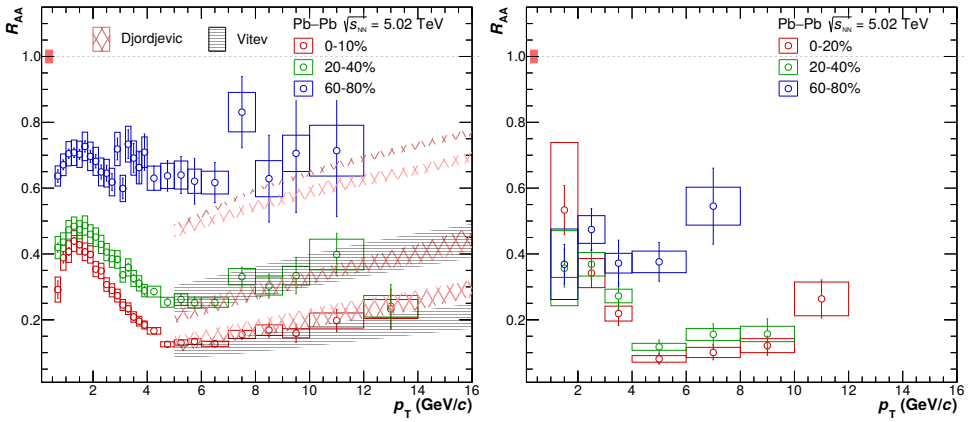

Figure 7.21: Nuclear modification factor R_{AA} for π^0 and η in different centrality classes, with comparison to theoretical calculations by Djordjevic *et al.* [180] and Vitev *et al.* [181].

plotted. They have been calculated from the yields in Pb-Pb from this work and the π^0 and η meson cross sections in pp collisions from [178] according to Equation 4.1. The expected centrality-dependent suppression is observed for the π^0 as well as for the η meson. The π^0 R_{AA} is compared to theoretical calculations by Djordjevic *et al.* [180] and Vitev *et al.* [181] in Figure 7.21. The results by Vitev *et al.*, based on the soft collinear effective theory $\mathrm{SCET_G}$ for the propagation of jets in matter, are plotted as bands, illustrating the variation of the coupling ($1.9 < g < 2.2$). The authors of [180] have provided two calculations, one with a constant temperature medium and a new development with Bjorken expansion, which are plotted in orange and red respectively. In peripheral events the π^0 R_{AA} favors the calculation with Bjorken expansion.

Chapter 8

Measurement of direct photons

Most of the photons which enter our detectors originate from the decay $\pi^0 \rightarrow \gamma\gamma$ because pions are abundantly produced and the majority of neutral pions decays to two photons. Direct photons however are defined as photons not originating from hadron decays. Because of the very short decay length of the π^0 , $c\tau = 25.5\,\mathrm{nm}$ [161], there is no way to distinguish decay and direct photons individually, photon by photon, in the reconstruction or analysis. Therefore, we use a statistical method and measure the ratio of inclusive photons over decay photons, differential in p_{T} and collision centrality. Any excess over 1 can then be interpreted as direct photon signal. In order to eliminate some of the experimental uncertainties, we measure the double ratio:

$$R_\gamma = \frac{\gamma_{\mathrm{I}}/\pi^0_{\mathrm{M}}}{\gamma_{\mathrm{D}}/\pi^0_{\mathrm{G}}} = \frac{\gamma_{\mathrm{I}}}{\gamma_{\mathrm{D}}} \tag{8.1}$$

How the inclusive photon invariant yield γ_{I} is obtained, will be described in Section 8.1. The decay photon spectra γ_{D} are provided by a Monte Carlo simulation which is based on the measured π^0 and η meson spectra, which are the most important sources of decay photons. The quantity π^0_{M} in the formula is the measured π^0 invariant yield, which was presented in chapter 7. π^0_{G} is the p_{T} distribution of π^0 generated by the simulation, according to the parametrization of π^0_{M}. The simulation will be described in greater detail in Section 8.2.

8.1 Inclusive photons

Inclusive photons are all produced photons, in our case measured with the photon conversion method as described before. It is the same photon sample that we use to build pairs for the invariant mass analysis of the neutral meson measurement. The corrections (Secondaries N_γ^{sec}, purity P, reconstruction

efficiency ϵ, conversion probability C), which have to be applied to the raw photon yield N_γ^{raw}, in order to obtain the inclusive photon invariant yield γ_{I} according to the following formula, will be described in the following paragraphs.

$$\gamma_{\mathrm{I}} = E\frac{\mathrm{d}^3N_\gamma}{\mathrm{d}p^3} = \frac{\mathrm{d}^2N}{2\pi p_{\mathrm{T}}\mathrm{d}p_{\mathrm{T}}\mathrm{d}y} = \frac{P\left(N_\gamma^{\mathrm{raw}} - N_\gamma^{\mathrm{sec}}\right)}{2\pi\ N_{\mathrm{ev}}\ \epsilon\ C\ p_{\mathrm{T}}\Delta p_{\mathrm{T}}\ \Delta y} \tag{8.2}$$

Here, N_{ev} is the number of analyzed collision events. The considered range in (pseudo)rapidity is $\Delta y = 1.6$ ($y = \eta$ for photons and $|\eta| < 0.8$). The bin widths and centers enter as Δp_{T} and p_{T}.

8.1.1 Correction for secondaries

Decay photons can come from decays of primary or secondary hadrons. The latter category we label secondary photons. It is subtracted at this point just like we have subtracted secondary π^0 from the sample of all measured ones. To do so, we use a cocktail simulation, similar to the previously described one (Section 7.4), based on measured spectra of particles which decay via the weak force into particles with photon decays. The most important considered chains are listed in Table 7.5. This time, not only the weak decays to secondary hadrons, but also the subsequent electromagnetic decays are simulated. The resulting secondary gamma spectra are converted to raw yields (N_γ^{sec}) with correction factors obtained from the detector simulation, in order to subtract them from the inclusive photon raw yields N_γ^{raw}, because the correction factors in Equation 8.2 differ between primary and secondary photons (see Figure 8.1). The resulting raw secondary gamma spectra are

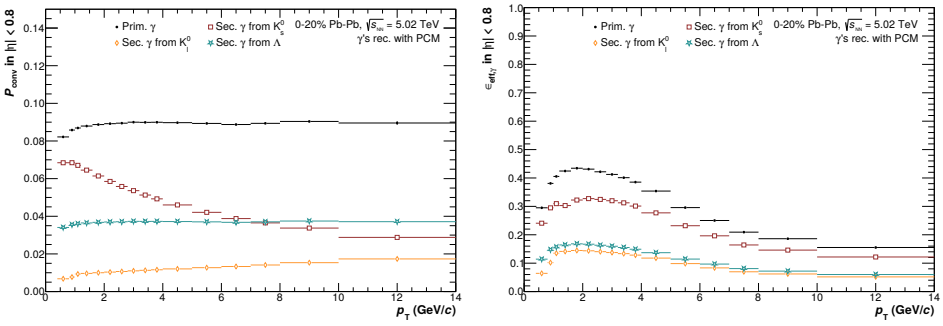

Figure 8.1: Correction factors (conversion probability C and efficiency ϵ) for secondary photons, calculated from MC for the 0-20% centrality class, compared to those of primary photons.

displayed in Figure 8.2.

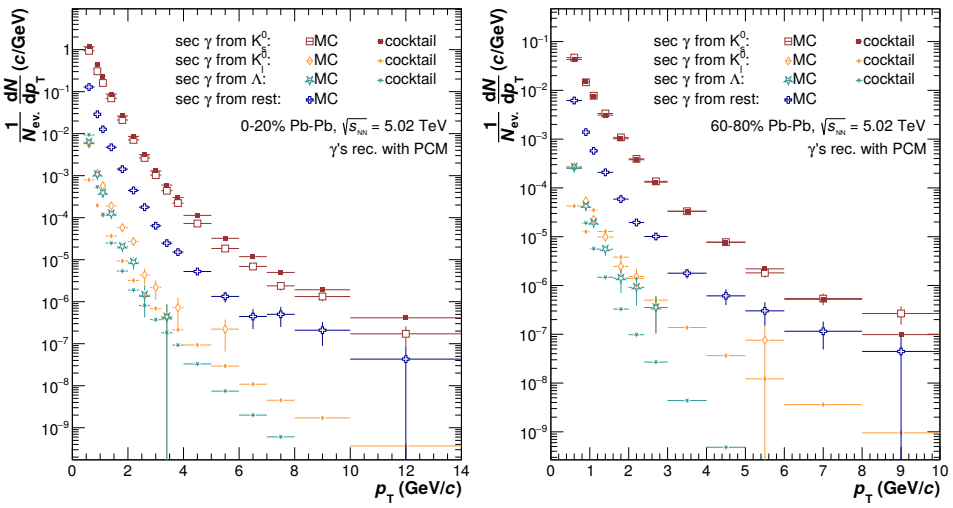

Figure 8.2: Raw spectra of secondary photons N_γ^{sec} in two centrality classes, from the data-driven cocktail simulation (filled markers) and from the standard MC simulation relying on model-based particle generation (open markers). The rest denotes photons from interactions of particles with the detector material.

8.1.2 Cut studies for purity enhancement

To take into account the fact that not all reconstructed photons are true photons, but some are falsely reconstructed from randomly paired tracks, we calculate a purity correction P from the MC simulation,

$$P = \frac{N_\gamma^{\text{true primary}}}{N_\gamma^{\text{primary}}} \tag{8.3}$$

which is used in Equation 8.2. After all MC photons have been reconstructed, we check for each candidate if the two associated tracks are truly an electron and a positron with the same mother photon in order to obtain the distribution of true photons. If a photon is a primary can also be checked with MC information.
When choosing selection cuts, we have to consider the trade-off between purity and efficiency. Ideally, the cut variables separate signal and background. In reality, the overlap region is kept if one wants to maximize the efficiency and it is removed if the purity should be maximized. In particular, if the distribution of a quantity in data is well described by MC, one can tolerate a moderate loss in efficiency in order to gain purity. When analyzing photons we use different cuts than in the neutral meson analysis because the photon purity is more important: In the meson analysis the invariant mass of a photon pair including a falsely reconstructed V_0 is not at the π^0 (or η) mass and is therefore not considered in the yield. In the photon analysis however, the purity enters as a factor in the corrected yield. At low p_T in central

events, this would be a 25% correction with consequently large uncertainties, because it is calculated from MC, which does not perfectly describe particle abundancies, p_{T} spectra, and flow effects of real data. For example, the number of $K^0_{\mathrm{s}} \rightarrow \pi^+\pi^-$ processes that are falsely reconstructed as photon conversions is a quantity that depends on the K^0_{s} abundancy, which is not perfectly reproduced by MC. Therefore, to keep the measurement uncertainties as small as possible, the photon purity needs to be as high as possible. Within this work, the effects of cut variations on the photon purity and efficiency have been studied as described in the following. Figure 8.3

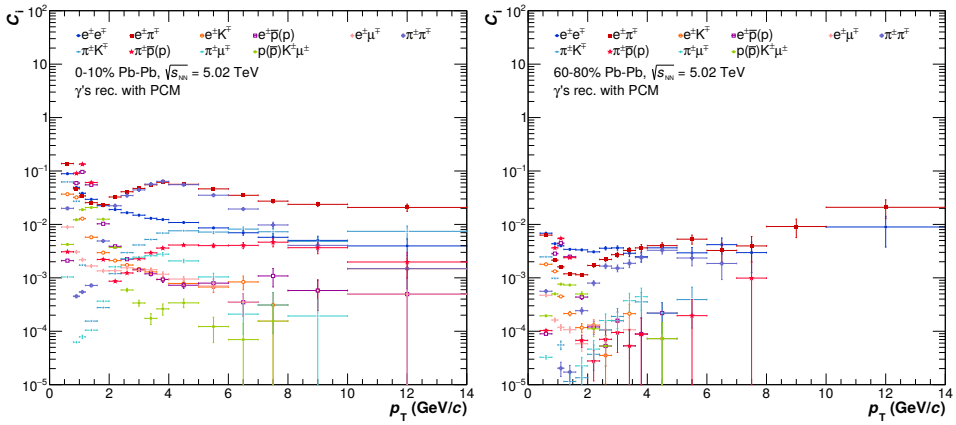

Figure 8.3: Ratio c_{i} of falsely reconstructed over true photons by contribution i, when using the same cuts that are used in the neutral meson analysis (see Table 7.3), in two centrality classes. In the legend, the particle species of the two tracks, that are falsely used instead of e^+ e^- pairs from photon conversions, are denoted.

shows the ratio of falsely reconstructed V_0 from different contributions to true photons, with the cuts from the neutral meson analysis. It shows the large contributions from e-π pairs, π-π, π-p, e-p, and e-e. A small portion of pions, kaons, and protons can pass the PID cuts which are supposed to identify electrons and positrons, and therefore enter the V_0 reconstruction. Therefore, the effect of different PID cuts on the photon purity was tested. In the TPC dEdx vs p_{T} distribution, the pion, kaon, and proton lines cross the electron line between 0.1 and 1 GeV track momentum and approach it again at higher p_{T} (see Figure 6.6). We use a 3σ cut around the electron expectation line, which improves the purity and the signal to background ratio for $p_{\mathrm{T}} < 2\,\mathrm{GeV}/c$ photon momentum compared to the $-3 < n\sigma_{\mathrm{e}} < 5$ cut used in the neutral meson analysis. At 3σ away from the electron expectation, the number of true electron tracks in MC has decreased to 1% of the maximum number.

In addition, we use a strict rejection of tracks that are too close to the pion expectation (3σ) up to $8\,\mathrm{GeV}/c$ (instead of only up to $2\,\mathrm{GeV}/c$) and a less strict cut afterward (2σ) where the $\mathrm{d}E/\mathrm{d}x$ separation is weaker and we have

to make sure that the efficiency does not decrease too much.
For the TOF PID (see Figure 6.7) the arrival time of a particle in the detector is measured relative to the time of the collision, and compared to the expectation for the different particle species, as a function of p_{T}. In a similar way as for the TPC PID, we select tracks with are not more than 4σ away from the electron line. The cut is only applied in the region $0.4 < p_{\mathrm{T}} < 2.5$ GeV/c because at high p_{T} the purity is not enhanced by a large factor which could justify the loss of efficiency, and at low p_{T} we found that the corrected π^0 yield was changed by the cut, which should not be the case because it is corrected for reconstruction efficiency, which accounts for different cut selections.

The purity and efficiency ratios with different PID cuts are shown in Figure 8.4. One can see that the TPC pion rejection cut improves the purity around 4 GeV/c by 13 %. The TOF cut combined with the stricter TPC electron selection cut enhances the purity at low $p_{\mathrm{T}} \approx 1$ GeV/c by 14 %. When analyzing the dataset at hand with cuts that have been used in previous photon analyses [164], the purity was lower than in [164]. A reason can be differences in the datasets and MC productions. With respect to that cut selection, the purity could be improved by 5% around $p_{\mathrm{T}} = 1$ GeV/c. After the PID cut modifications the combinatorial ee contamination dominates for $p_{\mathrm{T}} > 2$ GeV/c.

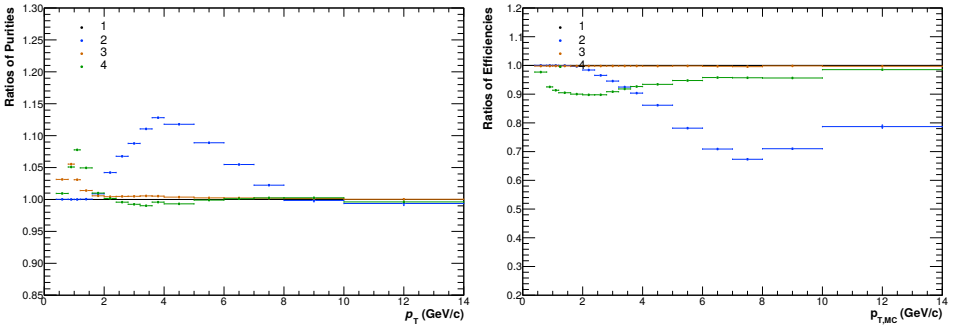

Figure 8.4: Effect of different modifications to PID cuts on the photon purity and efficiency (ratio to 1) for the most central events (0-10%).
1: Neutral meson analysis cuts as in Table 7.3
2: 3σ around the pion line for $0.4\,\mathrm{GeV}/c < p_{\mathrm{T}} < 8\,\mathrm{GeV}/c$, 1σ above
3: TPC electron selection cut 3σ
4: TOF 4σ cut for $0.4 < p_{\mathrm{T}} < 2.5$ GeV/c.

In a further step, the distribution of photon cut quantities for true and non-true photons was investigated with MC information to evaluate their separation power. In particular, we were interested in the pion and proton contamination, which is strong at low $p_{\mathrm{T}} < 2\,\mathrm{GeV}/c$ where we are especially interested in direct photons. Two examples are shown in Figure 8.5. In the χ^2 - Ψ_{pair} plane, the signal is distributed over the colored shape, whereas

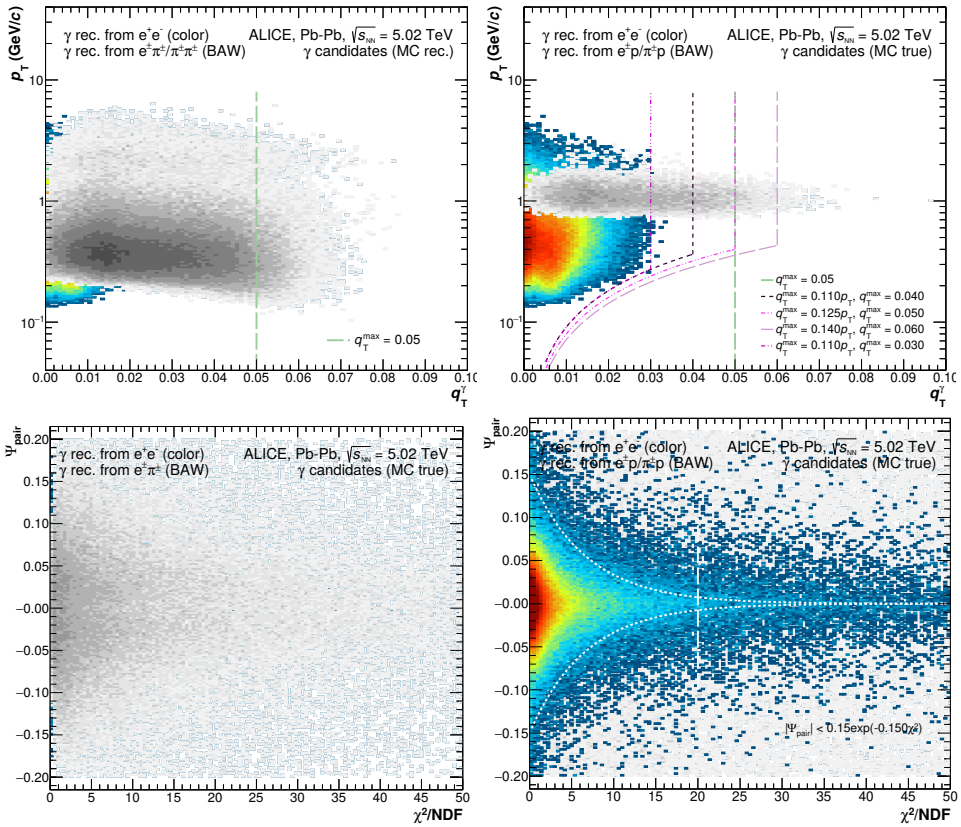

Figure 8.5: Signal-background separation power of q_{T}-p_{T} cut (**top**) and the χ^2-Ψ_{pair} cut (**bottom**) in the most central events (0-10%). True photons (the color visualizes the number) are plotted together with falsely reconstructed photons (grey) from electrons and pions (left) as well as from e-p and π-p (right). The green, magenta and white lines denote different cut options.

the background including pions and protons extends towards higher values of both variables. An exponential cut is used instead of a triangular shaped one, in order to follow the shape of the distribution of true photons. In the Armenteros-Podolanski plot we do the same q_{T} - α cut as in the meson analysis, but here the $q_{\mathrm{T,max}}$ depends in addition on the p_{T}, for the same reason. As it can be seen in the figure, this will mostly reduce the pion contamination because the proton contamination is located at higher p_{T}. The final cuts are summarized in Table 8.1. The resulting purities and efficiencies are shown in Figure 8.6 and Figure 8.8 .

Track selection	
Pion rejection	$n\sigma_\pi > 3$ for $0.4 < p < 8$ GeV/c
	$n\sigma_\pi > 2$ for $p > 8$ GeV/c
Electron selection	$-3 < n\sigma_e < 3$
TOF PID	$-4 < n\sigma_e < 4$ for $0.4 < p_T < 2.5$ GeV/c
Acceptance	$\lvert\eta\rvert < 0.8$
Photon selection	
Photon quality	$\chi^2 < 30$
PsiPair	$\lvert\Psi_{pair}\rvert < 0.15 * \exp(-0.15 * \chi^2)$
Armenteros-Podolanski	$(\alpha/\alpha_{max})^2 + (q_T/q_{T,max})^2 < 1$
	$q_{T,max} = 0.11 p_T$, $q_{T,max} = 0.04$, $\alpha_{max} = 0.95$
Acceptance	$\lvert\eta_{V_0}\rvert < 0.8$

Table 8.1: Cuts which were modified with respect to the neutral meson analysis cuts presented in Table 7.3.

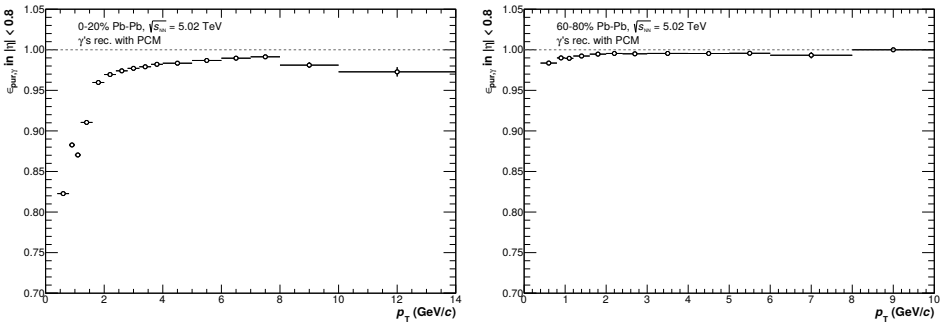

Figure 8.6: Purity with the final cuts for the 0-20% and 60-80% centrality classes. The other centrality classes are shown in section B.1.

8.1.3 Unfolding

In the next step, the fact that the reconstructed p_T of a photon can differ from the true p_T is taken into account by iterative Bayesian unfolding [182] of the measured spectra. Figure 8.7 shows the correlation of true and reconstructed p_T which is obtained from the MC simulation. The straight diagonal line is broadened by the limited detector resolution. At higher p_T where the width is small, one can see the effect of conversion electrons loosing energy due to Bremsstrahlung. This information is used in the unfolding procedure as it gives the probability to reconstruct a certain p_T, given the true p_T. In the first iteration, the distribution of MC photons as a function of true p_T is taken as a prior for the distribution of true p_T in data. As a result, we obtain the probability distribution for a true p_T, given the reconstructed p_T, which is then used as a prior in the next iteration. Four iterations are carried out.

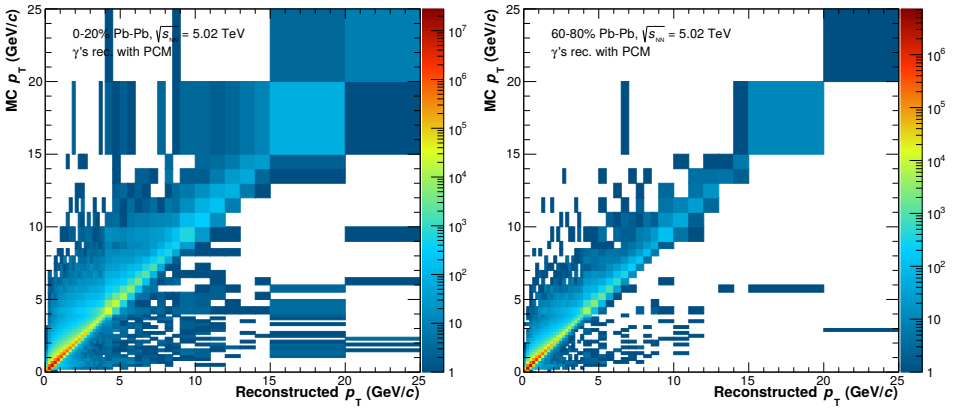

Figure 8.7: Correlation of true and reconstructed p_{T} of photons from MC in two different centrality classes. The color visualizes the number of photons in the respective bin.

8.1.4 Reconstruction efficiency and conversion probability

In the next step, we correct the measured photon spectra for reconstruction inefficiencies. The efficiency ϵ is defined as the ratio of reconstructed and validated primary photons over all generated and converted primary ones, where in both numerator and denominator the MC photon distributions as a function of the true p_{T} are used. It is shown in Figure 8.8.

$$\epsilon = \frac{N_{\gamma}^{\text{true primary}}}{N_{\gamma}^{\text{conv primary}}} \tag{8.4}$$

The conversion probability enters as a separate factor, calculated as the

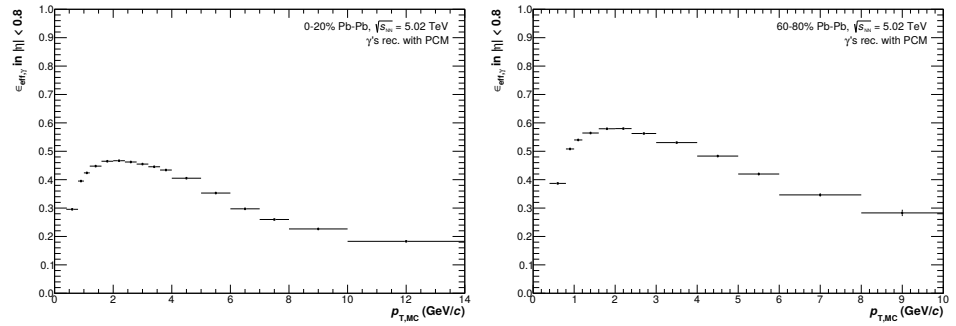

Figure 8.8: Reconstruction efficiency ϵ of primary photons in two different centrality classes. The other centrality classes are shown in section B.2.

ratio of the converted primary photons over all primary photons which were generated in the considered rapidity window.

$$C = \frac{N_{\gamma}^{\text{conv primary}}}{N_{\gamma}^{\text{gen primary}}} \tag{8.5}$$

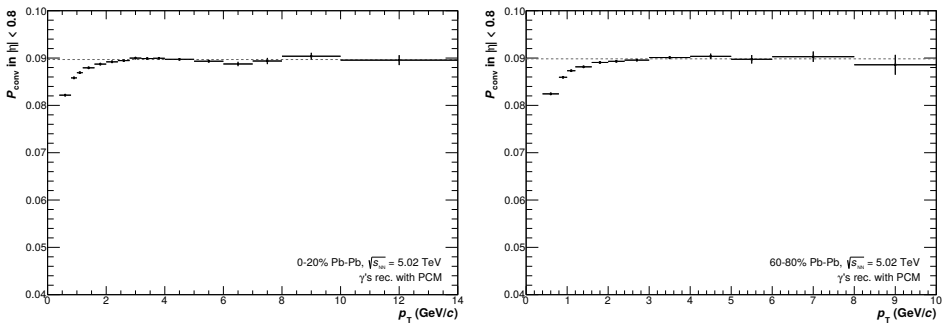

Figure 8.9: Conversion probability C of primary photons in two different centrality classes.

8.2 Decay photons

In the last section, it was described how the invariant yield of inclusive photons γ_{I}, needed for Equation 8.1, is measured. This section is concerned with obtaining the decay photon yield γ_{D}. As it was described before, decay photons originate mostly from π^0 decays, but also from other hadrons like for example η mesons. In the employed method, these hadrons with known photon decays are generated in a cocktail simulation, according to parametrizations of their invariant yields, measured in the same collision system and energy. Afterward, the particle decays are simulated using branching ratios provided by the PDG [161] and as a result, we obtain the invariant yield of decay photons.

8.2.1 Cocktail input

For the parametrization of the π^0 and the η, we use the invariant yield measured with the invariant mass method and photons from PCM as described in the previous Section 7. For the η meson, we parametrize the measured ratio η/π^0 and then multiply it with the π^0 parametrization. This intermediate step is done instead of parametrizing the measured η spectra directly because the η meson measurement has fewer points with larger uncertainties than the one of the π^0 and it is difficult to constrain the parametrization. When parametrizing the ratio however, we can use previous knowledge on the expected shape, for example that it should not change dramatically in the region $p_{\mathrm{T}} > 4\,\mathrm{GeV/c}$, like it was observed in previous measurements of η/π^0 for exampe in [87] and [88].

The following function [183] is used to parametrize the π^0 :

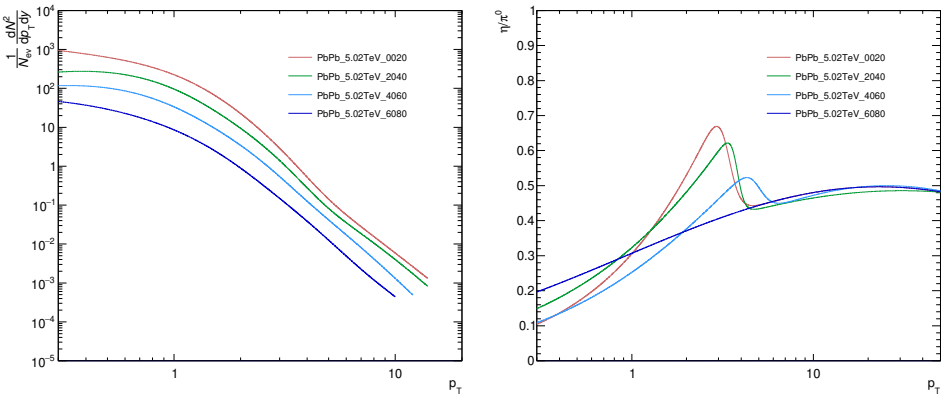

Figure 8.10: Parametrizations of measured π^0 spectra and η/π^0 ratios in all centrality classes.

$$p(p_{\mathrm{T}}) = N_0 p_{\mathrm{T}} \frac{\sqrt{p_{\mathrm{T}}^2 + m^2} - p_{\mathrm{T}}\beta}{\sqrt{1-\beta^2}} \exp\left(\frac{-\sqrt{p_{\mathrm{T}}^2 + m^2} + p_{\mathrm{T}}\beta}{\sqrt{1-\beta^2} T_{\mathrm{kin}}}\right) + N_1 \left(\frac{a}{1+p_{\mathrm{T}}}\right)^{n_1} + N_2 \left(\frac{b}{1+p_{\mathrm{T}}}\right)^{n_2} \tag{8.6}$$

It has 9 free parameters and is motivated phenomenologically. The first part of the sum describes an expanding particle source, where β is the flow velocity and T_{kin} the kinetic freeze-out temperature. The other two components are identical functions describing particles created in hard scatterings. The particle mass m is a fixed parameter in the fit. The η/π^0 ratio is fitted with the function q_1/q_2 with another phenomenologically motivated function:

$$q_{\mathrm{i}}(p_{\mathrm{T}}) = A_{\mathrm{i}} \left(p_{\mathrm{T}}^{-\left(a_{\mathrm{i}} + \frac{b_{\mathrm{i}}}{p_{\mathrm{T}}^{c_{\mathrm{i}}} + d_{\mathrm{i}}}\right)} \right) \tag{8.7}$$

Figure 8.10 shows the obtained parametrizations. They agree with the measured points within 10 % deviation and in particular within the statistical uncertainties (see section B.3).

Table 8.2 shows a list of considered mother particles with known decays including at least one photon. The second column lists the most relevant decay and the third column its branching ratio. Only hadrons that have at least one photon in the first step of the decay chain are considered. Photons from a decay chain like $\eta \to 3\pi^0 \to 6\gamma$ are included in the decay photons from π^0 because the measured π^0 spectrum contains those from η decays. Secondary photons like those from $K_{\mathrm{L}}^0 \to 3\pi^0 \to 6\gamma$ are not included in the cocktail simulation and have been removed consistently from the measured inclusive photon and π^0 spectra. In the fourth column of Table 8.2 it is indicated if a parametrization is based on a fit to a measurement or if it has been obtained from transverse mass (m_{T}) scaling, a concept which

hadron	decays into	BR [%] to this mode [161]	measured via	$C_{m_{\mathrm{T}}}$
π^0	$\gamma\gamma$	98.82 ± 0.03	$M_{\gamma\gamma}$, PCM	
η	$\gamma\gamma$	39.41 ± 0.20	$M_{\gamma\gamma}$, PCM, η/π^0	
η'	$\rho^0\gamma$	28.99 ± 0.50	m_{T} scaling from π^0	0.4 [184],[170]
ω	$\pi^0\ \gamma$	8.40 ± 0.22	m_{T} scaling from π^0	0.85 [184]
$\rho^0(770)$	$\pi^+\pi^-\gamma$	< 0.01	m_{T} scaling from π^0	1.0 [184],[170]
$\rho^\pm$	$\pi^\pm\gamma$	< 0.001	m_{T} scaling from π^0	1.0
ϕ	$\eta\gamma$	1.30 ± 0.03	measured [185] [a]	0.35 [184]
K^0_{S}	$\pi^+\pi^-\gamma$	< 0.01	measured [168]	
K^0_{L}	$\pi^\pm e^\pm\nu\gamma$	< 0.01	take K^0_{S} param.	
Σ^0	$\Lambda\gamma$	100	m_{T} scaling from p	0.49 [186]
Δ^0	$n\gamma$	$0.55 - 0.65$	m_{T} scaling from p [187]	1.0 [186]
Δ^+	$p\gamma$	$0.001 - 0.035$	m_{T} scaling from p	1.0 [186]
Λ	$n\gamma$	< 0.01	measured [168]	

Table 8.2: Considered hadrons with photon decays in the cocktail simulation. For every hadron, the most probable one is listed here together with its branching ratio.

was mentioned in Section 4.1. For the cocktail simulation, it is used to calculate the parametrizations of hadrons that have not been measured for $\sqrt{s_{\mathrm{NN}}} = 5.02\,\mathrm{TeV}$ according to formula 8.9, which follows from equation 8.8.

$$\mathrm{P}_{\mathrm{m/b}}(m_{\mathrm{T}}) = C_{m_{\mathrm{T}}} \cdot \mathrm{P}_{\pi^0\ /\mathrm{p}}(m_{\mathrm{T}}) \tag{8.8}$$

$$E\frac{\mathrm{d}^3 N_{\mathrm{m/b}}}{\mathrm{d}p^3} = \mathrm{P}_{\mathrm{m/b}}(p_{\mathrm{T}}) = C_{m_{\mathrm{T}}} \cdot \mathrm{P}_{\pi^0\ /\mathrm{p}}\left(\sqrt{p_{\mathrm{T}}^2 + m_{\mathrm{m/b}}^2}\right) \tag{8.9}$$

Parametrizations of these unexplored mesons ($\mathrm{P_m}$) are obtained from the π^0 parametrization P_{π^0} . For baryons ($\mathrm{P_b}$), the proton parametrization ($\mathrm{P_p}$) is used instead. The factors $C_{m_{\mathrm{T}}}$, which have been determined from particle ratios in other measurements, or predicted by PYTHIA, are also listed in Table 8.2. As mentioned before, deviations from m_{T} scaling in AA collisions are reasonable and have been observed in this thesis (see Figure 7.20) and in [87] at intermediate p_{T} ($2 < p_{\mathrm{T}} < 5\,\mathrm{GeV/c}$)) (as well as at low $p_{\mathrm{T}} < 3.5\,\mathrm{GeV/c}$ in pp [188] and $p_{\mathrm{T}} < 4\,\mathrm{GeV/c}$ in p-Pb [189] collisions). The largest contribution to the decay photon cocktail originating from a m_{T} scaled hadron comes from the ω meson and amounts to a few percent (see Figure 8.11).

8.2.2 Cocktail simulation

In the MC cocktail simulation, particles are generated with a random transverse momentum within $0 < p_{\mathrm{T}} < 50\,\mathrm{GeV/c}$ in the direction of random

azimuthal angle ϕ and random rapidity within $-1 < y < 1$. Afterward, the p_{T} parametrizations are used to scale the generated mother particles accordingly. Decays are simulated using PYTHIA [170]. The decay photon spectra γ_{D} that were produced in the rapidity range which is considered for analysis of direct photons ($|y| < 0.8$) are stored together with the information about its mother. The contributions of the different mother particles to all decay photons are plotted in Figure 8.11. It shows that most decay photons originate from neutral pions, followed by η, ω and η' mesons.

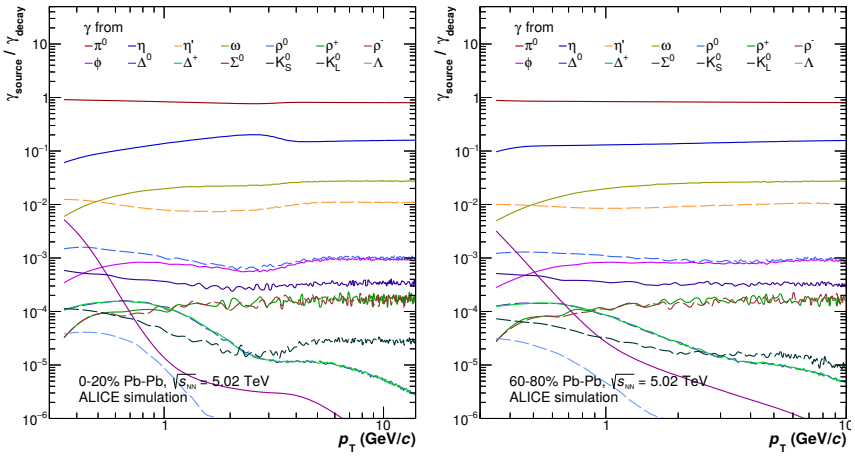

Figure 8.11: Ratio of photons from a given source to all decay photons for two centrality classes.

8.3 Direct photons

In order to determine the direct photon double ratio R_γ according to Equation 8.1, the π^0 analysis was repeated with the same cuts and in the same p_{T} binning as used in the inclusive photon measurement. From these two components, the $\gamma_{\mathrm{I}}/\pi^0_{\mathrm{M}}$ ratio was calculated. In addition, the $\gamma_{\mathrm{D}}/\pi^0_{\mathrm{G}}$ ratio is estimated from the decay photons and π^0 generated by the cocktail simulation. The results are presented in Section 8.5.
Direct photon spectra are calculated from the inclusive photon spectra and the double ratio using the following equation:

$$\gamma_{\mathrm{dir}} = \gamma_{\mathrm{I}} \cdot (1 - \frac{1}{R_\gamma}) \tag{8.10}$$

which follows from the definition of direct photons as inclusive minus decay photons:

$$\begin{aligned} \gamma_{\mathrm{dir}} &= \gamma_{\mathrm{I}} - \gamma_{\mathrm{D}} \\ &= \gamma_{\mathrm{I}} - \frac{\gamma_{\mathrm{I}}}{R_\gamma} \end{aligned} \tag{8.11}$$

8.4 Systematic uncertainties

The systematic uncertainties were estimated in a similar way as those for the neutral mesons. The analysis was repeated with varied cuts and the differences of the physics observables were calculated. These are the inclusive photon spectra γ_{I} and the R_γ. By calculating the difference of the ratio directly, some of the uncertainties (and also possible errors) which affect the numerator and the denominator cancel out. Smoothing of the uncertainties as a function of p_{T} was also applied as described in Section 7.5. Due to the moderate dependency on the centrality class, the systematic uncertainty values estimated in the 0-20% class were used as an estimate for those in 20-40% and the ones from 60-80% were used for the 60-80% centrality class. One exception is the π^0 yield extraction. The effect on the direct photon observables of varying the latter was evaluated in all centrality classes. The uncertainties of the direct photon spectra γ_{dir} follow from error propagation using those of γ_{I} and R_γ according to Equation 8.10. One can see from the

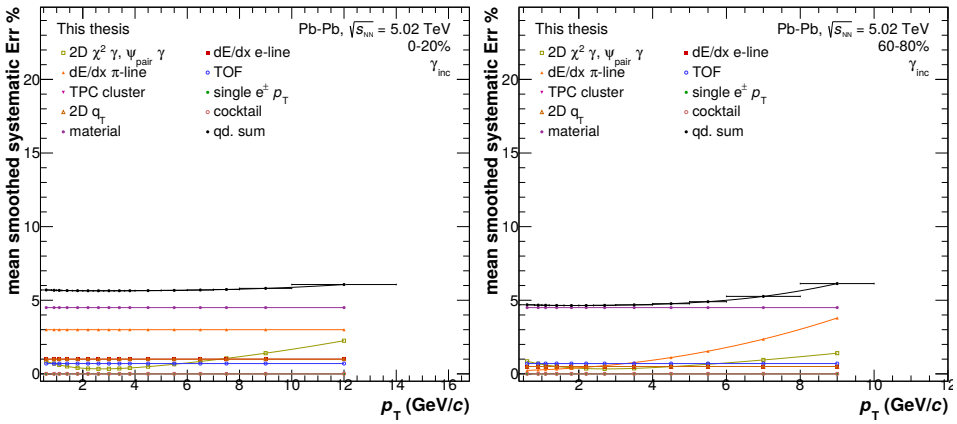

Figure 8.12: Smoothed systematic uncertainties of inclusive photons (single contributions separately and the quadratic sum) for 0-20% and 60-80%.

Figures 8.12 and 8.13 that the material budget is the origin of the largest systematic uncertainty. In central events, the next largest contribution is caused by the PID cuts. For the R_γ, the uncertainty due to the yield extraction is a relevant contribution because the π^0 spectra enter the calculation of R_γ. The cocktail contribution accounts for the uncertainty in the choice of parametrizations for the η/π^0 ratio and π^0 , as well as the deviation from m_{T} scaling for the ω meson. Of those, the η/π^0 ratio uncertainty dominates. It is chosen to decrease for increasing p_{T}, because the shape of the η/π^0 ratio is known better at higher p_{T}. The value at low p_{T} is estimated using the uncertainty of the η measurement multiplied with the percentage of decay photons originating from η mesons.

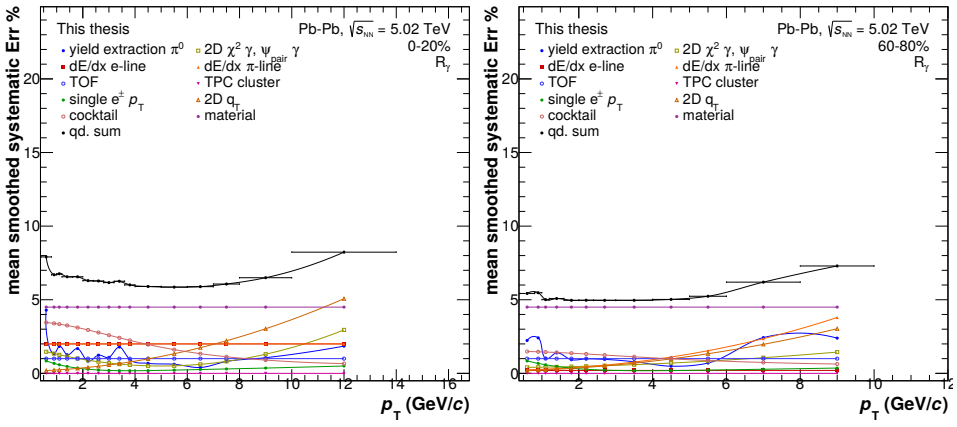

Figure 8.13: Smoothed systematic uncertainties of R_γ (single contributions separately and the quadratic sum) for 0-20% and 60-80%.

8.5 Direct photon results

The measured inclusive photon and simulated decay photon spectra (γ_I and γ_D from Equation 8.1, Equation 8.2, and Equation 8.11) are compared in Figure 8.14. The two ratios which enter the double ratio (numerator and denominator of Equation 8.1) are compared in Figure 8.15. The double

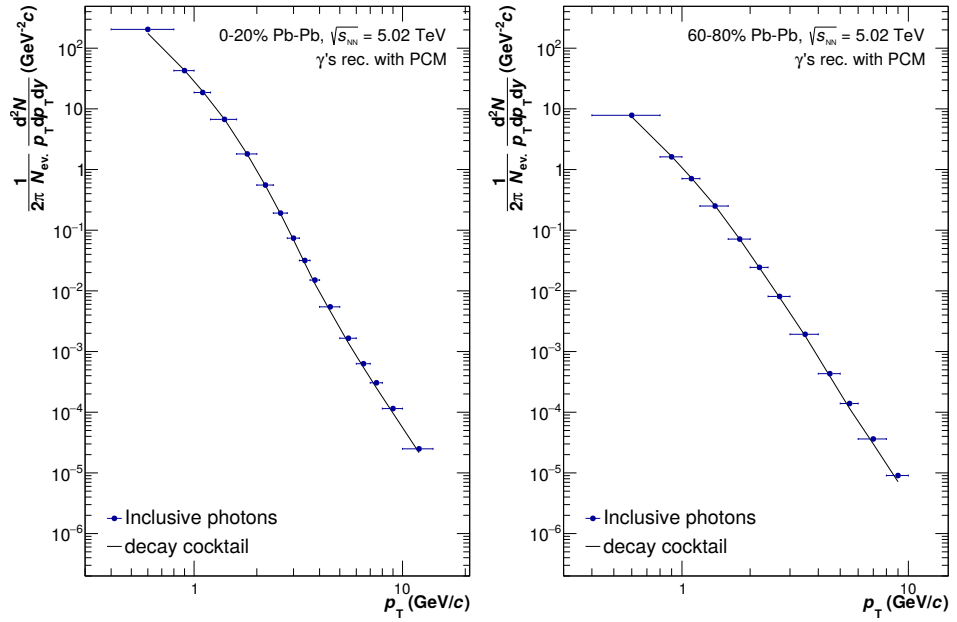

Figure 8.14: Inclusive and decay photon spectra in central and peripheral events. For other centrality classes see Figure B.9.

ratio R_γ itself is presented in Figure 8.16 for the centrality classes 0-20%,

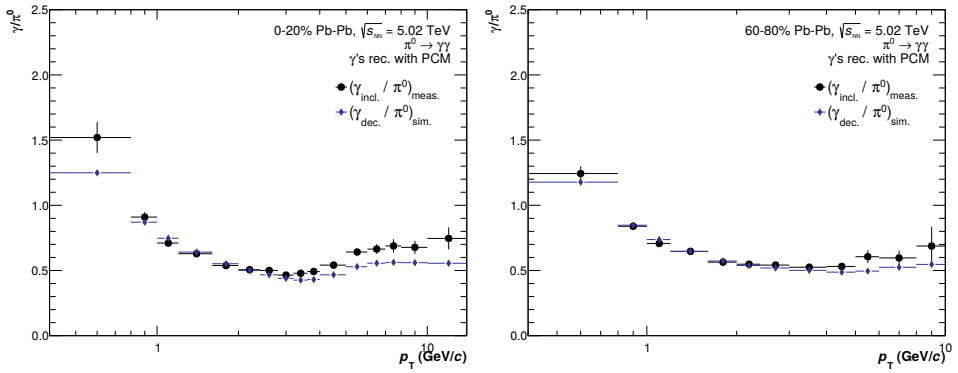

Figure 8.15: Comparison of γ_I/π^0_M and γ_D/π^0_G in central and peripheral events. For other centrality classes see Figure B.10.

20-40%, 40-60% and 60-80%. In the high p_T region of most central events, a clear direct photon signal is found. At lower p_T and in the other centrality classes, the measurement is consistent with a small or no direct photon contribution.

The right panel shows that the results from this thesis are in agreement with

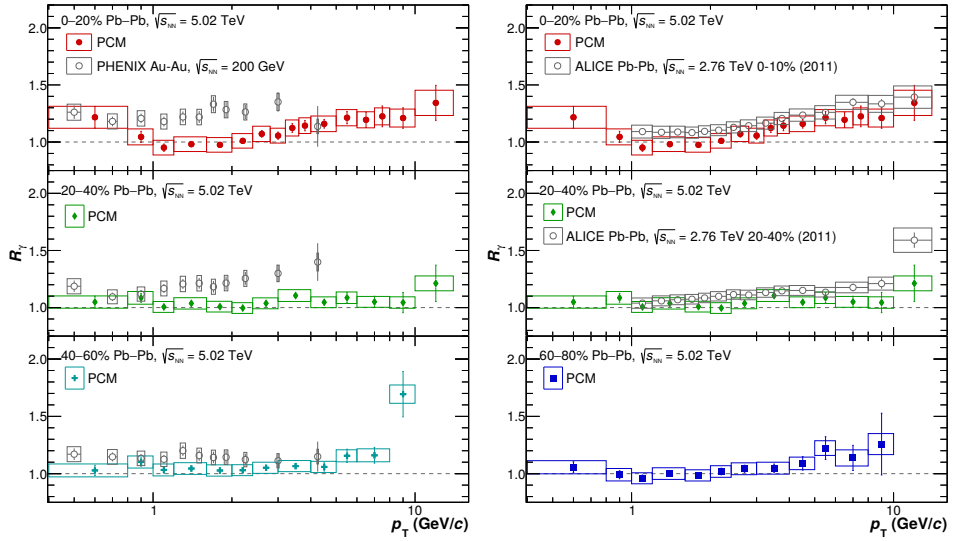

Figure 8.16: Direct photon double ratios in different centrality classes with comparisons to PHENIX [121] and ALICE 2.76 TeV results [164]. The vertical lines represent statistical and the heights of the boxes systematic uncertainties. The widths of the boxes indicate the bin widths. Note that in the top right panel the 0-20% centrality class of 5.02 TeV is plotted with the 0-10% of 2.76 TeV.

those which were measured at the lower collision energy $\sqrt{s_{NN}} = 2.76$ TeV [164] within the uncertainties, but all data points lie below. The expected higher temperature, longer lifetime, and larger volume of a medium that is

produced with a higher collision energy is expected to also result in a larger thermal photon yield. In the calculations of [190], a larger direct photon signal was found for $\sqrt{s_{\mathrm{NN}}} = 5.02\,\mathrm{TeV}$ than for 2.76 TeV. This expectation can neither be confirmed (the measured points with 5.02 TeV lie consistently below those measured with 2.76 TeV) nor excluded (the measured points are in agreement with [190] and other calculations for for 5.02 TeV). The fact that different centrality classes are compared (0-10% of 2.76 TeV to 0-20% of 5.02 TeV) is not expected to have a large influence, due to the moderate centrality dependence of the R_γ at low p_{T} which is observed over the other centrality classes.

The current measurement extends the p_{T} coverage with respect to the previously published ALICE direct photon result in Pb–Pb collisions at $\sqrt{s_{\mathrm{NN}}} = 2.76\,\mathrm{TeV}$ [123] from $p_{\mathrm{T}} > 0.9\,\mathrm{GeV}$ to $p_{\mathrm{T}} > 0.4\,\mathrm{GeV}$, which corresponds to the p_{T} reach of the PHENIX measurement in Au–Au collisions at $\sqrt{s_{\mathrm{NN}}} = 200\,\mathrm{GeV}$ [121]. In most central events, there is a clear discrepancy to the PHENIX measurement in the region 1-4 GeV/c, as can be seen in the top left panel of Figure 8.16.

In the left panel of Figure 8.17 the measured double ratios are compared to

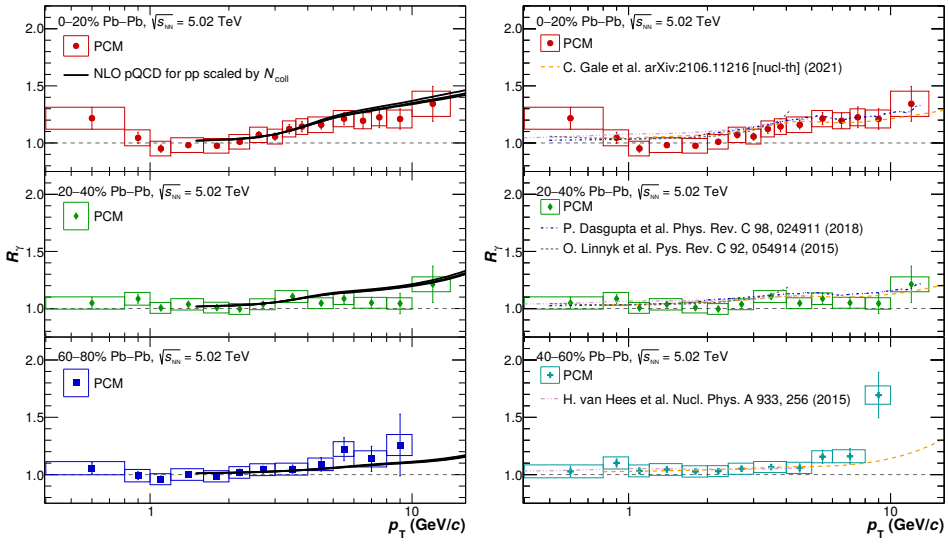

Figure 8.17: Direct photon double ratios in different centrality classes with results from theoretical calculations. **Left:** pQCD calculation of prompt photons [94]. To illustrate the theoretical uncertainty, for each centrality class three curves are drawn with different values for the renormalization and factorization scales $\mu_{\mathrm{R}} = \mu_{\mathrm{F}} = p_{\mathrm{T}}$, $p_{\mathrm{T}}/2$ and $2p_{\mathrm{T}}$. Parton distribution functions from [191] and fragmentation functions from [96] were used for this calculation. **Right:** Comparison to models combining the medium evolution and photon emission rates by C. Gale *et al.* [192], P. Dasgupta *et al.* [190], O. Linnyk *et al.* [106], and H. van Hees *et al.* [193].

calculations from [94]: The authors compute prompt photon production in

hadron-hadron collisions with pQCD to next-to-leading order in the strong coupling constant α_s. That includes the processes depicted in Figure 4.1. For comparison to the R_γ which was measured in this thesis, the prompt photon contribution in Pb–Pb collisions is calculated as:

$$R_{\gamma_p} = \frac{\gamma_D + \gamma_p \cdot N_{coll}}{\gamma_D} \tag{8.12}$$

where γ_p is the above-mentioned theoretically calculated prompt photon cross section in pp collisions, converted to an invariant yield and N_{coll} is the average number of nucleon-nucleon collisions in the respective centrality class, taken from [65]. The quantity γ_D denotes the decay photon contribution. Here, the same cocktail simulation output is used to calculate the theoretical R_γ which is used for the experimental one. Figure 8.17 shows that down to the p_T where the prompt photon contribution can be calculated with pQCD, the measured direct photon R_γ is consistent with the prompt photon R_{γ_p} within the uncertainties.
As mentioned in Section 4.2, in order to compare direct photon measurements to theoretical calculations at lower p_T, one has to combine photon emission rates from different sources, prompt and thermal photons, with the space-time evolution of the medium. This is done in the models from which calculations for R_γ are plotted in the right panel of Figure 8.17. The calculations by P. Dasgupta *et al.* [190] use a longitudinally boost invariant (2+1) dimensional ideal hydrodynamic framework. The initial conditions are generated by a MC Glauber model with a smooth energy density, however the authors suggest using fluctuating initial conditions with inhomogeneous energy density profiles in future calculations, like in their previous work [194]. The hydrodynamic simulation is starting at time $\tau_0 = 0.14\,\mathrm{fm/c}$, switching from QGP to hadron gas at $T = 170\,\mathrm{MeV}$. Thermal photons from the QGP and hadron gas as well as prompt photons from calculations in [195], based on the JETPHOX MC program (NLO pQCD), are included. Also in the calculations by van Hees *et al.* [193], a boost invariant ideal hydrodynamic framework with Glauber initial conditions is used to model the medium evolution. Prompt photons are obtained from the measured spectra in pp collisions, using the x_T-scaling ansatz [196]. In the calculations by C. Gale *et al.* the description of the heavy-ion collision and medium evolution starts with IP-Glasma initial conditions [110]. In [192] the effect of including a pre-equilibrium phase is studied, described using the KøMPøST approach [197], before switching to modeling the QGP with relativistic hydrodynamics. The latter is done by using the MUSIC approach [198], which accounts for shear and bulk viscosity. The pre-equilibrium phase starts at time $\tau = 0.1\,\mathrm{fm/c}$, which corresponds to a saturation scale of $Q_s = 2\,\mathrm{GeV}$ and evolves into the hydrodynamic phase at $\tau_0 = 0.8\,\mathrm{fm/c}$. In order to obtain photon yields, photon emission rates are folded with the development of medium properties over time, obtained from KøMPøST and MUSIC. In

the pre-equilibrium phase, the required temperature is calculated from the energy density and the QCD equation of state. The hadronic phase, which starts when the medium reaches a temperature of $T = 145\,\text{MeV}$, is modeled with UrQMD [199]. However, since photons are not produced in this package, hydrodynamics is used up to T = 105 MeV for the calculation of photon production. Prompt photons, calculated with NLO pQCD, are also included. All models above use the same QGP photon emission rates [102], different additions to the basic photon rates in the hadronic phase [103], and different thermalization times τ_0. The model used by O. Linnyk *et al.* [106] is a microscopic transport approach called Parton-Hadron-String Dynamics (PHSD) [200], which is able to describe the partonic as well as the hadronic phase, both in and out of equilibrium, in one model.
All calculations are consistent within the uncertainties of the measurement, which therefore cannot discriminate between them. Also, we cannot claim a significant thermal photon signal. However, the tension of the direct photon puzzle, which was describing the discrepancy between PHENIX data and theoretical models, is further reduced.
Direct photon spectra are shown in Figure 8.18 for all centrality classes. For

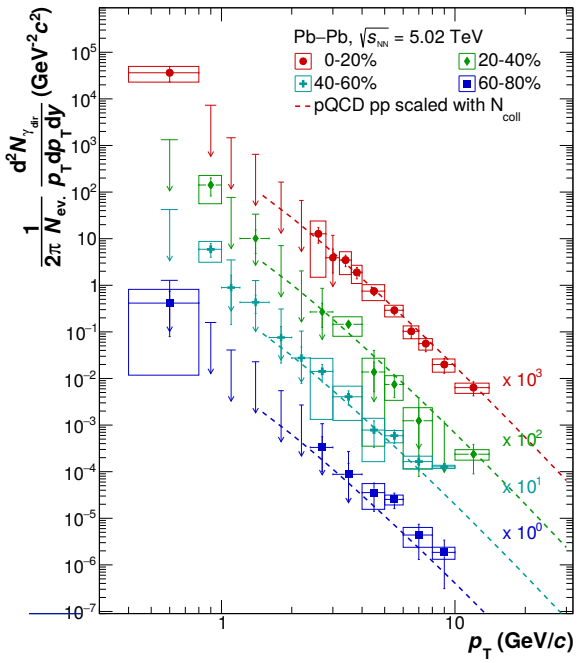

Figure 8.18: Direct photon spectra points and upper limits in different centrality classes with pQCD calculation [94] for prompt photons in pp collisions, scaled with N_{coll} [65]. The vertical lines represent statistical and the heights of the boxes systematic uncertainties.

data points that are consistent with a value of 0 within the quadratic sum of statistical and systematic uncertainties, upper limits (95% confidence level)

are calculated and drawn as arrows. A data point is drawn in addition to the arrow if $\gamma_{\mathrm{dir}} = 0$ is not excluded when considering only either the statistical or systematic uncertainty. One can see the similar shapes of the spectra in Figure 8.18, which are consistent with the pQCD calculation. In the region $1 \lessapprox p_{\mathrm{T}} \lessapprox 2\,\mathrm{GeV}$ only upper limits could be measured in most central and peripheral events, due to the small or absent direct photon signal. Figure

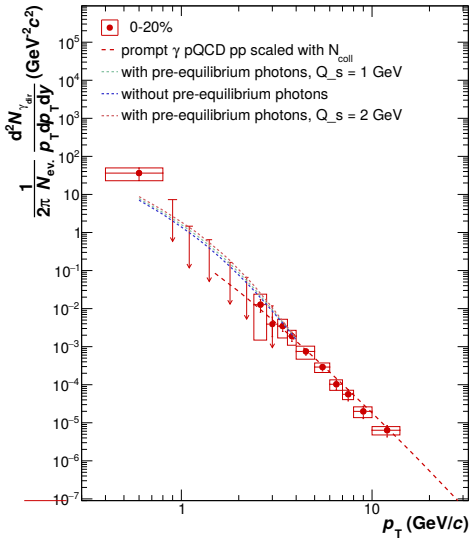

Figure 8.19: Comparison to a theoretical calculation of direct photons with and without pre-equilibrium photons [201] with different values for the saturation scale Q_{s}, in the 0-20% centrality class.

8.20 shows a comparison to all theoretical models mentioned above, which indicates a good agreement.
The lowest point of the direct photon spectrum and R_γ ($0.4 < p_{\mathrm{T}} < 0.8\,\mathrm{GeV}$) disagrees slightly with the theoretical calculations: the direct photon signal in this bin is larger than in the adjacent bins. This could be either a result of an actual increase in direct photon production, (for example due to an additional source of photons, in addition to prompt and thermal photons, or due to a different p_{T} dependency and number of thermal photons than expected) or otherwise, it can be a result of a p_{T} -independent error/uncertainty or a statistical fluctuation; the value is consistent with a small thermal photon signal predicted by the models within 2σ.
In Figure 8.19 the measured direct photon spectra in most central events are compared to the calculation in [201]. Here, a pre-equilibrium phase is described using effective kinetic theory based on the relativistic Boltzmann equation, starting at time $\tau = Q_{\mathrm{s}}^{-1}$ with only gluons (from which quarks are then produced in the following evolution). The medium expansion is described using the Bjorken model. The photon rate is calculated using the small-angle approximation like in [111]. The parton dynamics

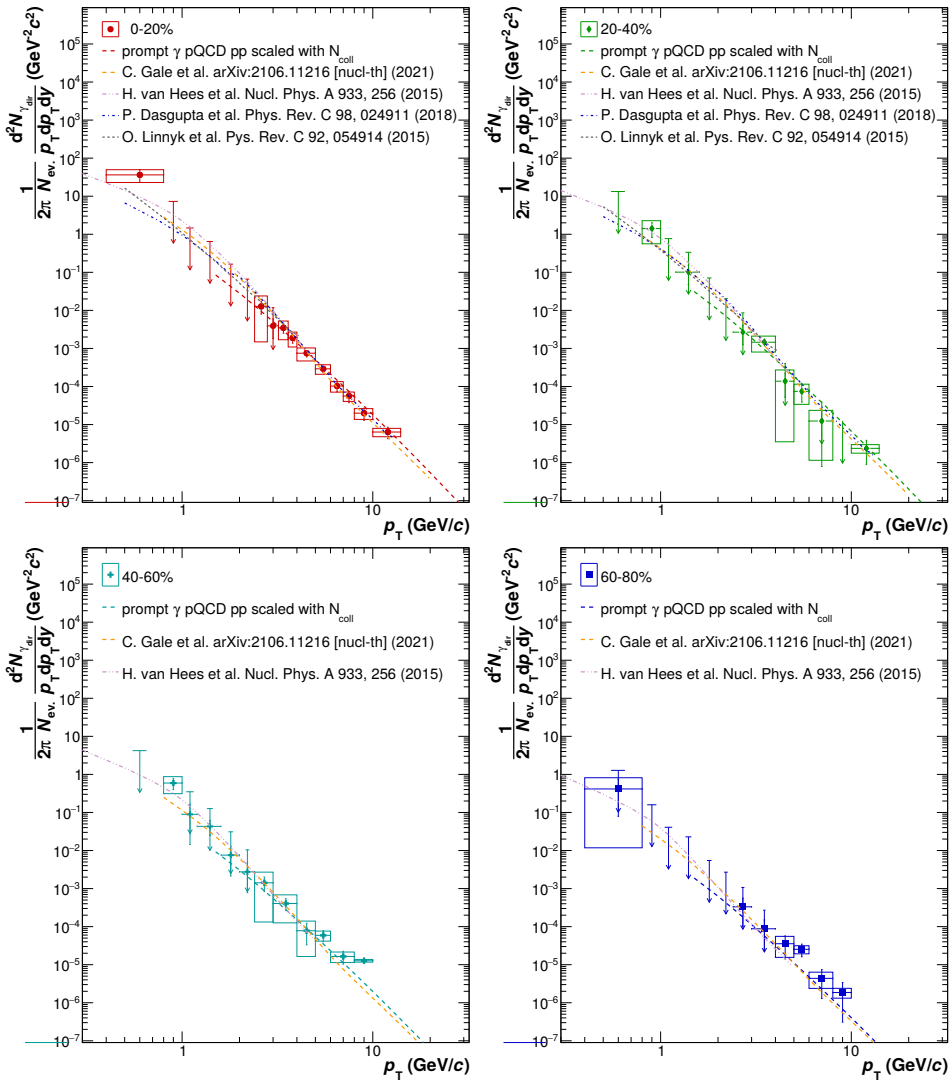

Figure 8.20: Direct photon spectra in different centrality classes with different model calculations for prompt photons by W. Vogelsang [94] and for direct photons by C. Gale *et al.* [192], P. Dasgupta *et al.* [190], O. Linnyk *et al.* [106], and H. van Hees *et al.* [193].

of the pre-equilibrium phase are stopped at time $\tau_0 = 0.4\,\mathrm{fm/c}$. Prompt photons and thermal photons (from viscous hydrodynamics modeling up to $T = 105\,\mathrm{MeV}$), calculated by J.-F. Paquet, are included in this direct photon calculation. Two versions with different values for the saturation scale, $Q_\mathrm{s} = 1\,\mathrm{GeV}$ and $Q_\mathrm{s} = 2\,\mathrm{GeV}$ are compared. It is found that a direct photon measurement can be sensitive to the initial stages of the heavy-ion collision, however not within the current experimental uncertainties.

Chapter 9

Summary, conclusion and outlook

Summarizing, direct photon spectra and R_γ, as well as π^0 and η meson spectra, nuclear modification factors R_{AA} and η/π^0 ratios have been measured with the photon conversion method in central, semi-central, and peripheral Pb–Pb collisions at $\sqrt{s_{\mathrm{NN}}} = 5.02\,\mathrm{TeV}$.

New methods in this thesis
In order to measure neutral mesons as precisely as possible for the decay photon simulation, the description of background in the invariant mass spectra was investigated within this work and improved in the case of the neutral pion. Furthermore, for a more realistic estimate of systematic uncertainties of neutral mesons at high p_{T}, where also statistical uncertainties are large, the "Barlow criterion" was considered in the step of smoothing the distributions of uncertainties obtained from cut variations as a function of p_{T}. A new approach to reject pile-up events (which was not developed within this thesis) was applied to both neutral meson and direct photon analyses, which allowed to omit a further correction to meson and photon spectra. For the direct photon analysis, the effect of different particle identification cuts on the purity of the measured inclusive photons was studied. In particular, it was found that a PID cut using the TOF detector in addition to the TPC PID can be very useful in the p_{T} range around $1\,\mathrm{GeV/c}$.

Conclusion and outlook
No significant low p_{T} direct photon signal, which could be interpreted as thermal photon signal, could be found. However, the fact that the measurement is in agreement with the theoretical models, which describe the whole system evolution of a heavy-ion collision, from the initial conditions to the pre-equilibrium, QGP and hadronic phases, is an important ingredient for better understanding strongly interacting matter under extreme conditions.

The presented direct photon measurement is the first one using the highest available heavy-ion collision energy of $\sqrt{s_{\mathrm{NN}}} = 5.02\,\mathrm{TeV}$, which is a factor 1.8 higher than the one used for the previous ALICE measurement, 2.76 TeV [123]. The expected collision energy dependency of direct photon production [190] could neither be confirmed nor excluded. The fact that the R_γ in 5.02 TeV collisions is systematically smaller than the one in 2.76 TeV could be caused by one of the changes to the analysis procedure which were described above.
The R_γ measured by PHENIX using a *lower* collision energy ($\sqrt{s_{\mathrm{NN}}} = 200\,\mathrm{GeV}$ Au–Au collisions) is significantly larger than the one presented in this thesis in the p_{T} region 1-4 GeV/c, in the 0-20% centrality class. Therefore, our results contribute to solving the direct photon puzzle, a term which was coined because theoretical models were not able to simultaneously describe the large direct photon yield measured by PHENIX and the large measured v_2.
Neutral pion spectra could be measured with sufficient precision in order to well constrain the parametrizations for the decay photon cocktail simulation. However, the statistics of the dataset at hand is just high enough to perform a measurement of the η meson. By parametrizing the η/π^0 ratio, it was possible to obtain a satisfying estimate of the number of decay photons from η mesons, however, the choice of parametrization causes a relatively large uncertainty on the direct photon measurement. The measured η/π^0 confirms that using m_{T} scaling is not a good alternative to using a direct measurement of the η meson for the cocktail simulation.
The suppression of high p_{T} particles due to parton energy loss, which is expected from the measurements of other hadrons, was observed in the nuclear modification factors of π^0 and η, ordered in strength by centrality class. However, studying high p_{T} effects like the sensitivity to the initial value of the jet quenching parameter or differences in suppression between different particle species is not the strong suit of this analysis and dataset due to the limited p_{T} reach and the large uncertainties of the η meson. By combining PCM measurements with those using the calorimeters with their higher reconstruction efficiency and triggering capability at higher p_{T}, it is possible to measure neutral mesons up to higher transverse momenta [87][178].
Also, the η meson measurement uncertainties will greatly benefit from higher statistics in datasets that will be analyzed in the future. Looking at the invariant mass distributions around the η meson mass (section A.3) it becomes clear that it is difficult to distinguish the peak from a statistical fluctuation in the lowest and highest p_{T} bins. This statistics-effect also enhances the systematic uncertainty that is assigned to the yield extraction. Partially, because the signal and background shapes can be determined more realistically with more statistics and therefore varying the integration window will result in a smaller variation of the corrected yield. Therefore, both statistical and systematic uncertainties can be reduced by increasing the statistics

of the dataset.
The dataset at hand (recorded in 2015) contains more events than the dataset used for the previously published ALICE measurement of direct photons [123] which used part of the 2.76 TeV Pb–Pb data (recorded in 2010). After event selection, 80 million events compared to 13 million events were available for the PCM analysis. In the analysis presented in this thesis, direct photons could be measured down to 0.4 GeV/c instead of 0.9 GeV/c in [123]. Furthermore, the statistics in the 2015 dataset is also larger than in the data used for the previously published ALICE measurement of neutral mesons in 2.76 TeV Pb–Pb collisions (recorded in 2011) [87] ([5] with 2010 data). However, in the 2011 dataset, a centrality trigger was used which enhanced the number of recorded events in semi-central events with respect to peripheral events and in central events with respect to semi-central events. Therefore, in the most central class (0-10%) fewer events were available for the PCM analysis in this thesis (10 million), compared to 19 million in [87]. Only the analysis of peripheral events benefits from the larger overall statistics and it was possible to measure the η meson in the 60-80% centrality class, which was in [87] only measured up to 50% centrality.
Going forward, not all of the data from 5.02 TeV Pb–Pb collisions, which were recorded in LHC run 2, was analysed yet (so far about 20% of the total integrated luminosity). Furthermore, the heavy-ion data taking of LHC Run 3 will start in 2022, where an about 7 times higher interaction rate will be recorded by the upgraded ALICE experiment. This will also reduce the statistical uncertainty of the direct photon measurement, which helps especially for $p_{\mathrm{T}} < 1\,\mathrm{GeV/c}$ and $p_{\mathrm{T}} > 5\,\mathrm{GeV/c}$ where it is comparable to or larger than the systematic uncertainty.
However, for a more precise measurement with the goal to disentangle and characterize different direct photon sources, and to extract an effective temperature, it is crucial to reduce the systematic uncertainties as well. The largest contribution to the systematic uncertainty of the R_γ, the 'material', is caused by the imperfect implementation of detector materials and geometry in GEANT combined with the fact that the probability for pair production depends on the type of the traversed material, as described in section 7.5 and chapter 5. By weighting the efficiency in radial bins, using a detector region with well-known material, the TPC gas, to calibrate the rest of the detector [202], the assigned value of 4.5% can be reduced to 2.5% [203]. Furthermore, in the upgraded ALICE detector for LHC run 3, a dedicated wire for conversions was installed in the ITS, made out of 99.9% pure tungsten material with precise thickness measurements available. In addition to the material and the π^0 and η yield extraction and cocktail parametrization uncertainties, which were discussed previously in this chapter, the particle identification in the TPC is accompanied by sizeable uncertainties as well, despite recalibration of the nσ values in data and checking that for MC no recalibration was needed. The reason for this can be related to the contam-

ination being different in data and MC and has to be investigated further in future work. Generally speaking, a good description of cut quantities by MC simulation is crucial for small systematic uncertainties because the reconstruction efficiency is calculated from MC.
In order to avoid the overestimation of systematic uncertainties, it is left for future work to check the Barlow criterion not only for the cut variations in the neutral meson analysis but also in the direct photon measurement and for the yield extraction. Moreover, it would be correct to generate a new π^0 parametrization and cocktail simulation for every cut variation. However, this was not feasible technically at the time. This might cause an overestimation of the q_T uncertainty on the R_γ at high p_{T} and is also left for future work.
When detecting only a small direct photon signal, like it is the case with ALICE compared to the PHENIX measurements, it is particularly difficult to extract their flow coefficients with reasonable uncertainties (the smaller the value and the larger the uncertainty of R_γ, the larger the uncertainty of the v_2 [126]). The triangular flow coefficient v_3 could so far only be measured by PHENIX, however with large uncertainties [204]. With ALICE it is expected, with the aforementioned new datasets and planned improvements to the analysis procedure, to measure v_2 also in 5.02 TeV Pb–Pb collisions and v_3 in the future. With their complementary information, these measurements can provide new insights into the mechanisms of direct photon production.

Appendix A

Additional neutral meson figures

A.1 Invariant mass distributions around the π^0 mass corresponding to Figure 7.5 for 20-40% and 60-80%

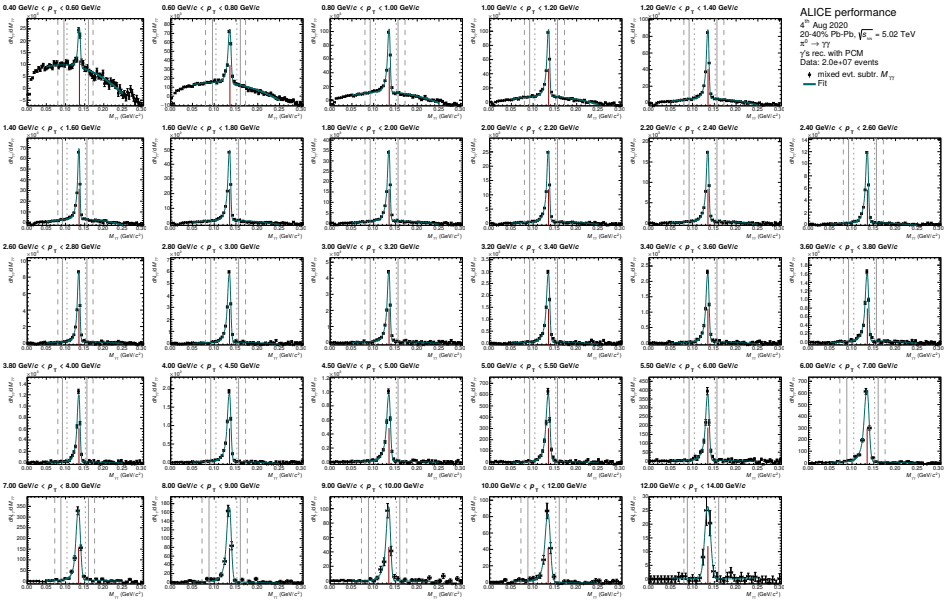

Figure A.1: Data 20-40%

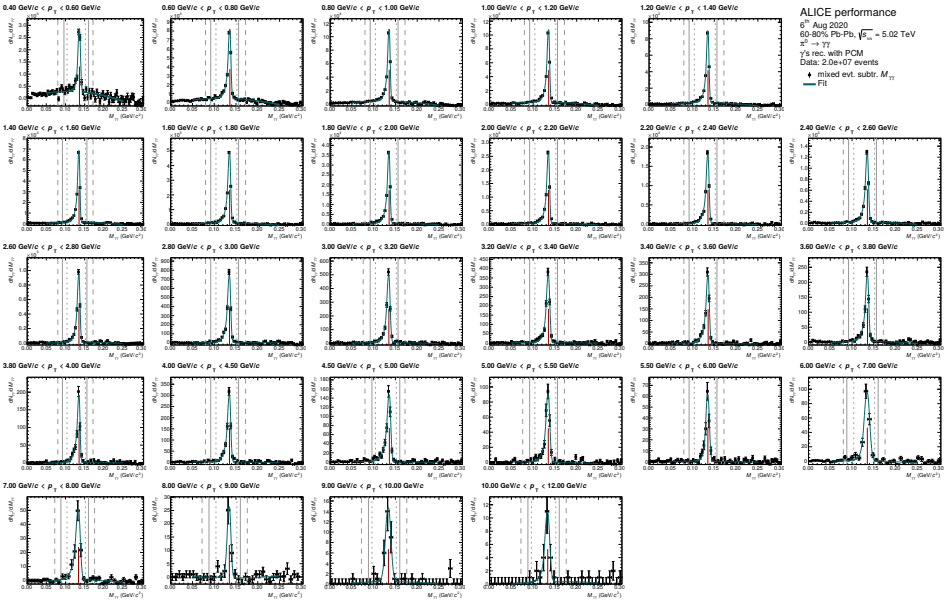

Figure A.2: Data 60-80%

A.2 Invariant mass distributions around the π^0 mass in validated MC

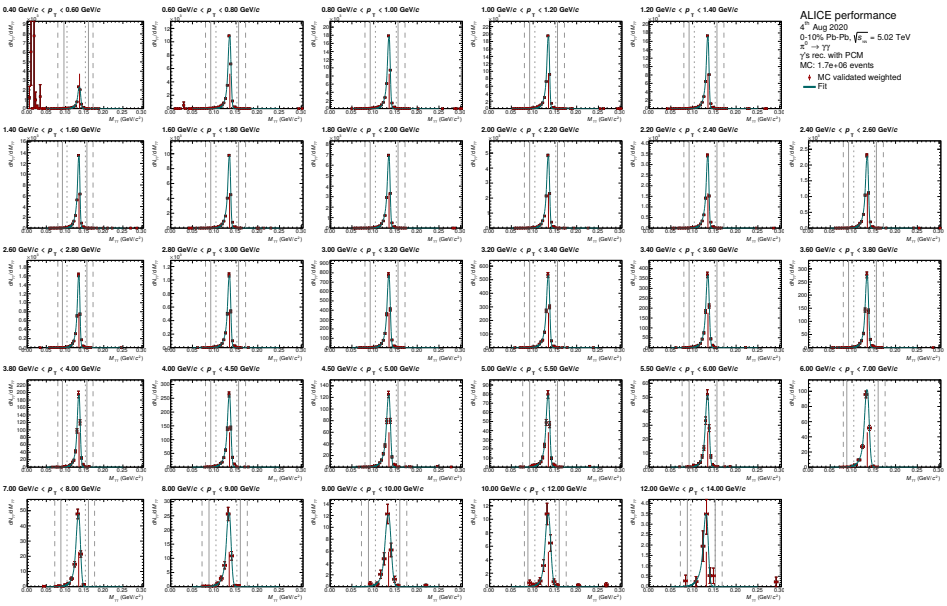

Figure A.3: Validated MC (LHC18∗ and LHC16i∗ from Table 7.2), 0-10%

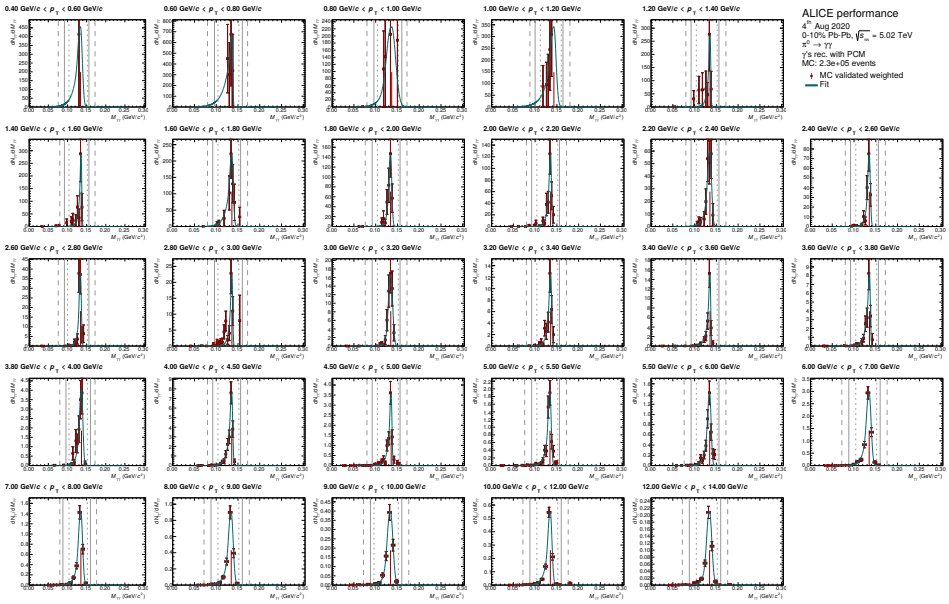

Figure A.4: MC with added signals (LHC16h4 from Table 7.2), validated, 0-10%

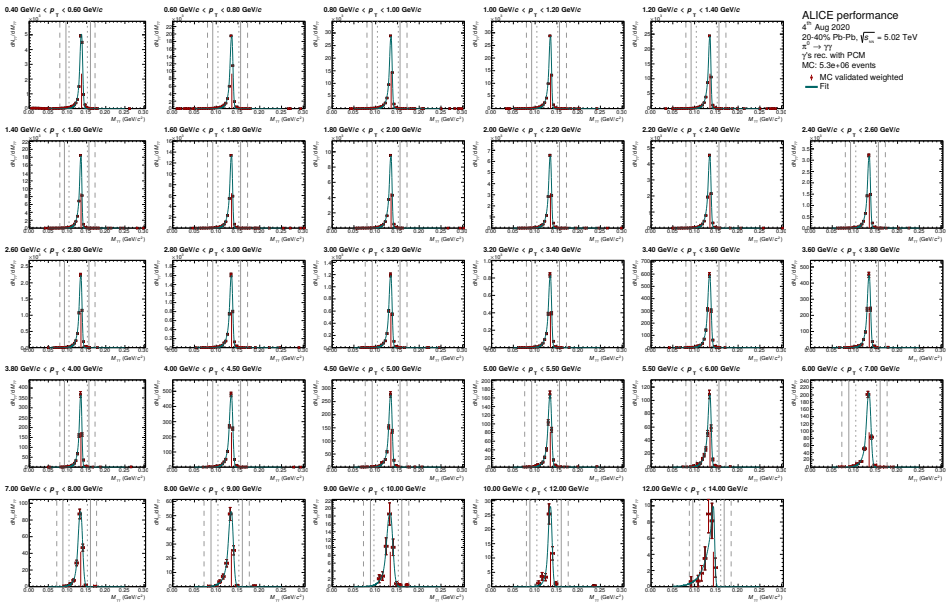

Figure A.5: Validated MC (LHC18∗ and LHC16i∗ from Table 7.2), 20-40%

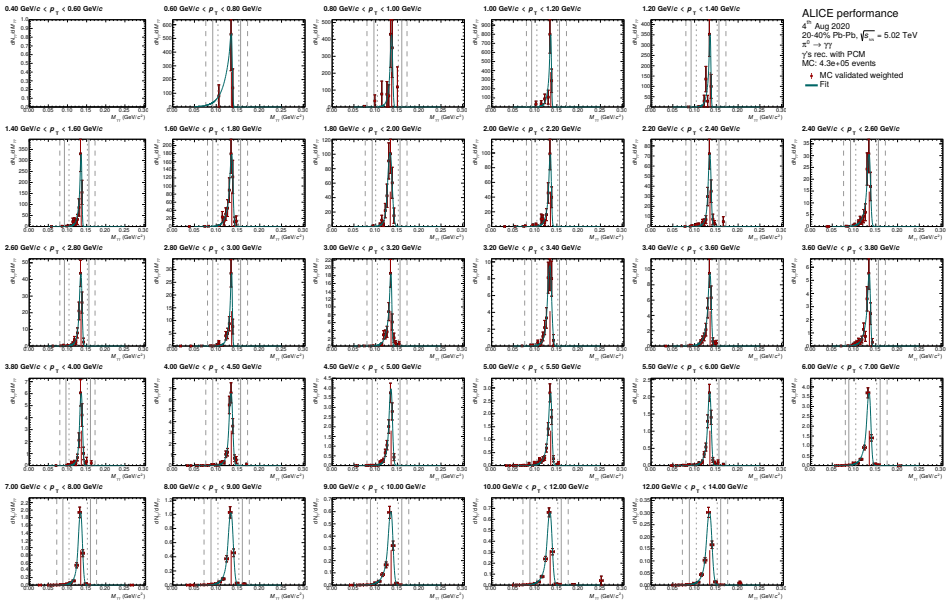

Figure A.6: MC with added signals (LHC16h4 from Table 7.2), validated, 20-40%

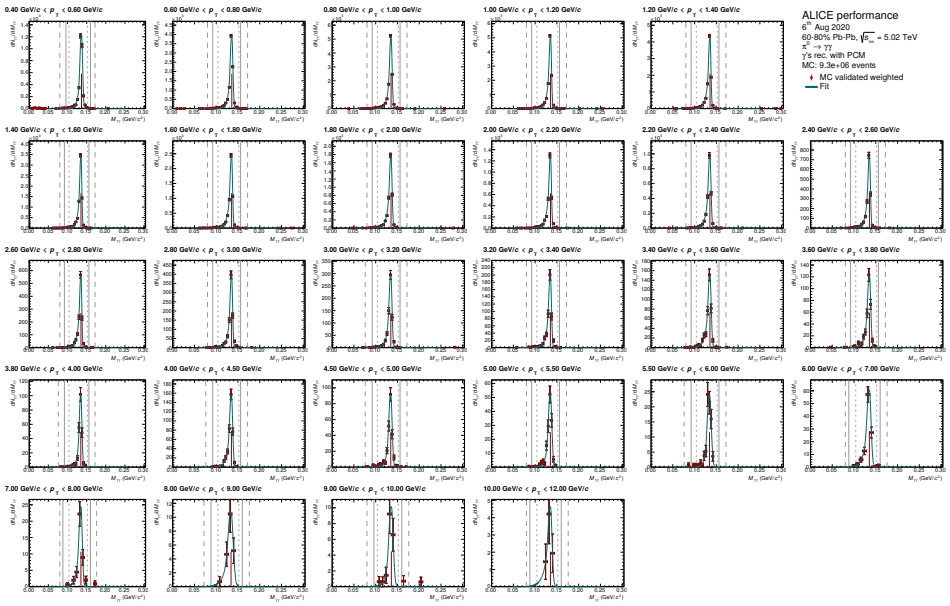

Figure A.7: Validated MC (LHC18∗ and LHC16i∗ from Table 7.2), 60-80%

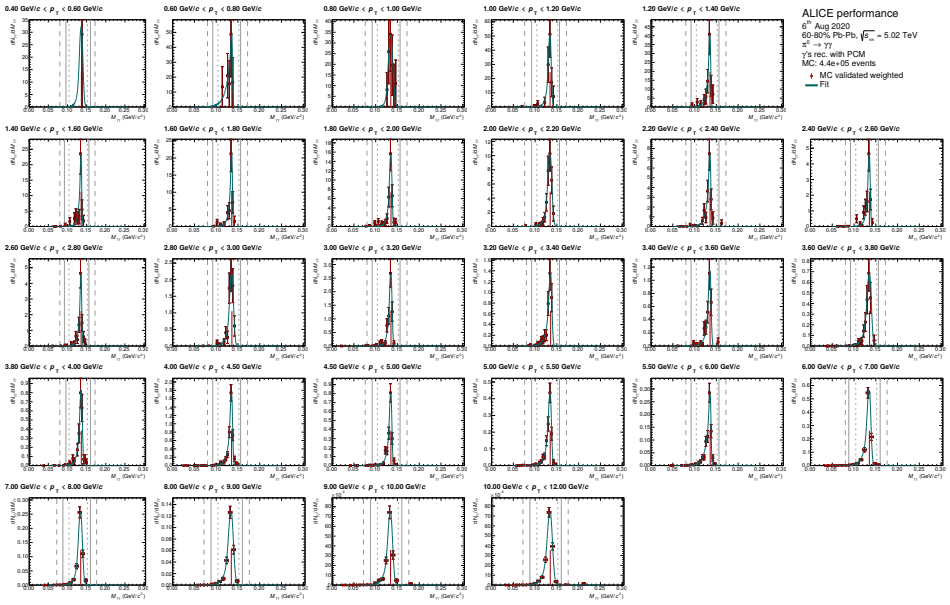

Figure A.8: MC with added signals (LHC16h4 from Table 7.2), validated 60-80%

A.3 Invariant mass distributions corresponding to Figure 7.5 around the η mass for all centrality classes

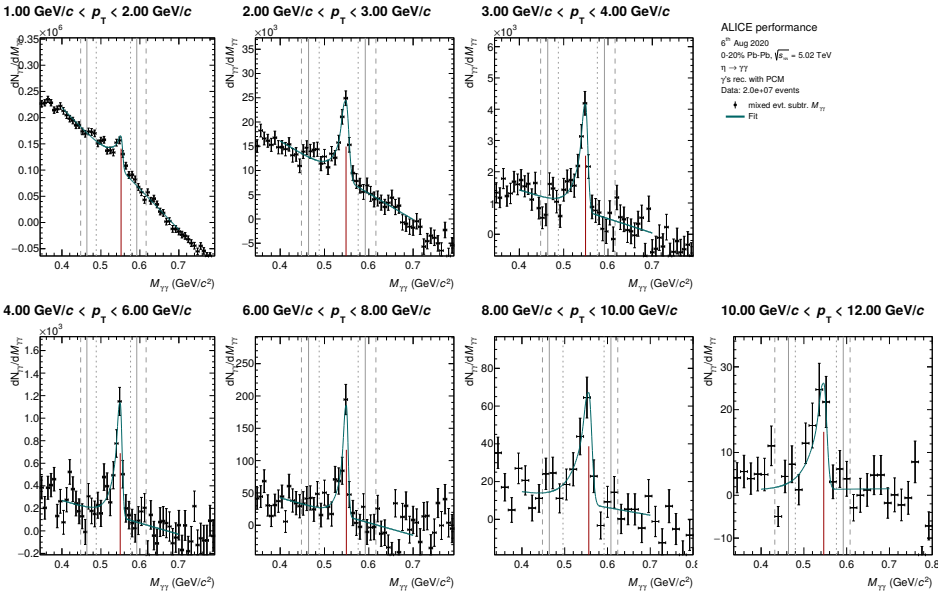

Figure A.9: 0-20%

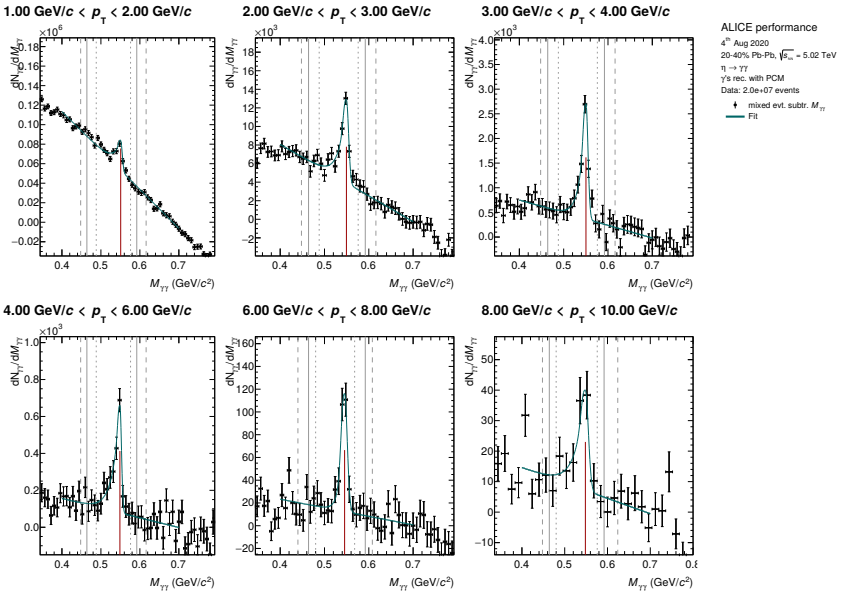

Figure A.10: 20-40%

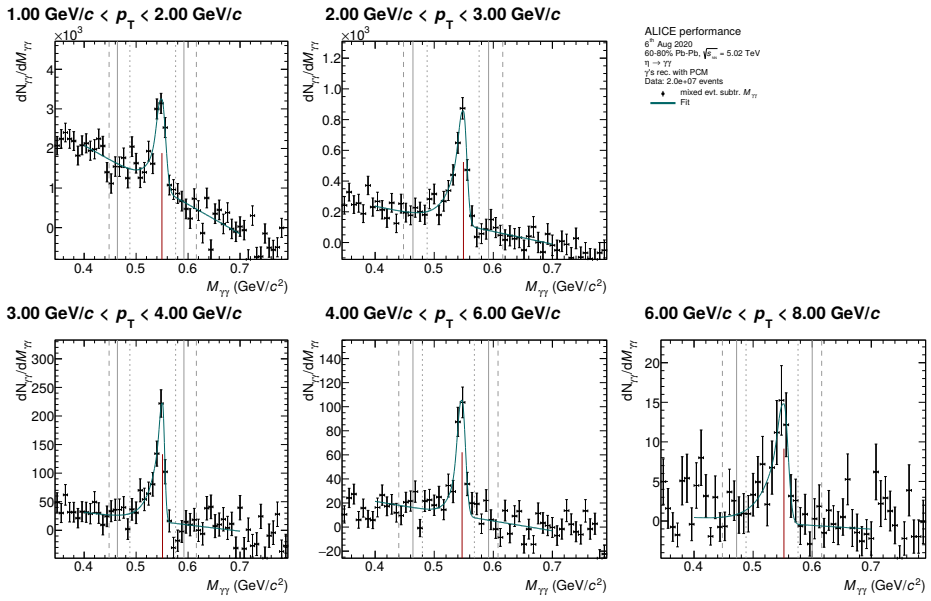

Figure A.11: 60-80%

A.4 Invariant mass distributions around the η meson mass in validated MC

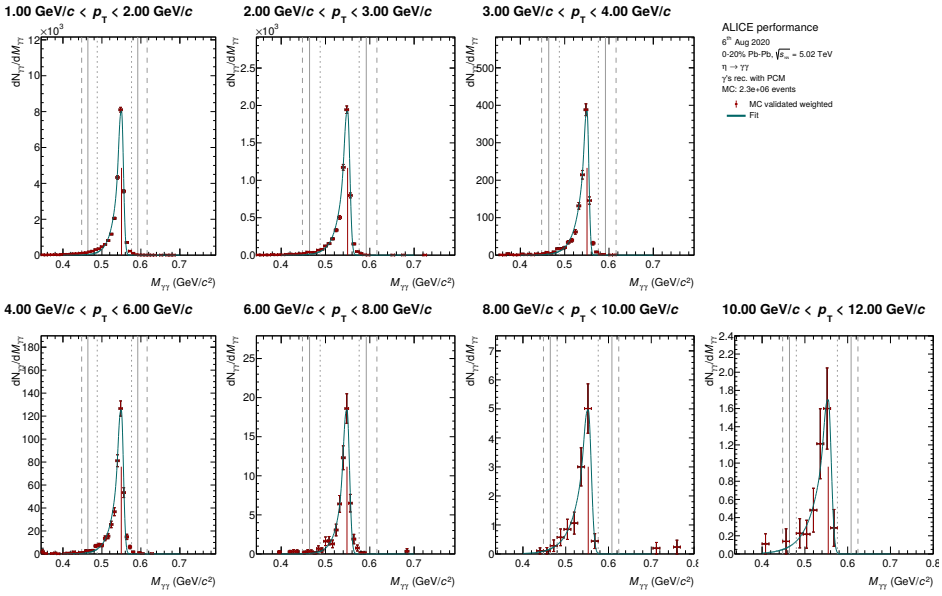

Figure A.12: Validated MC (LHC18∗ and LHC16i∗ from Table 7.2), 0-10%

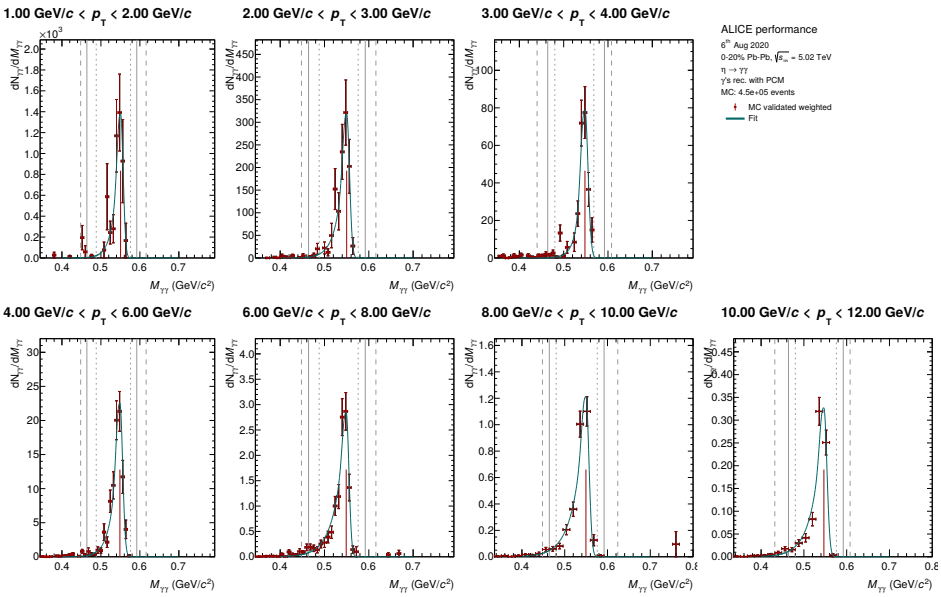

Figure A.13: MC with added signals (LHC16h4 from Table 7.2), validated, 0-10%

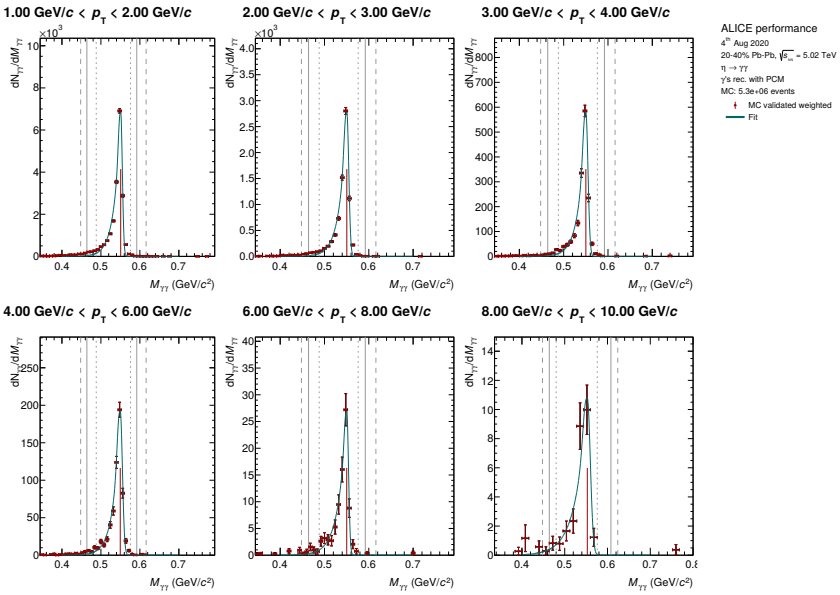

Figure A.14: Validated MC (LHC18∗ and LHC16i∗ from Table 7.2), 20-40%

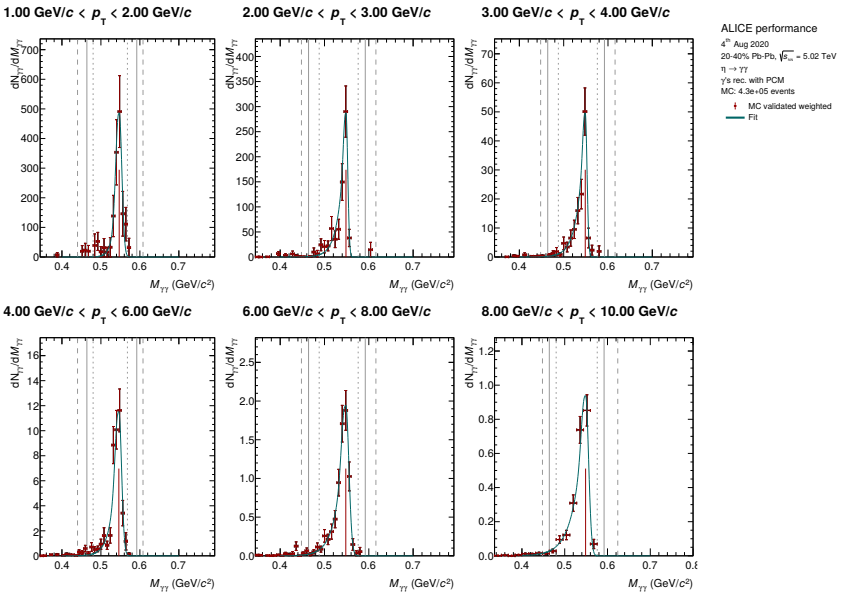

Figure A.15: MC with added signals (LHC16h4 from Table 7.2), validated, 20-40%

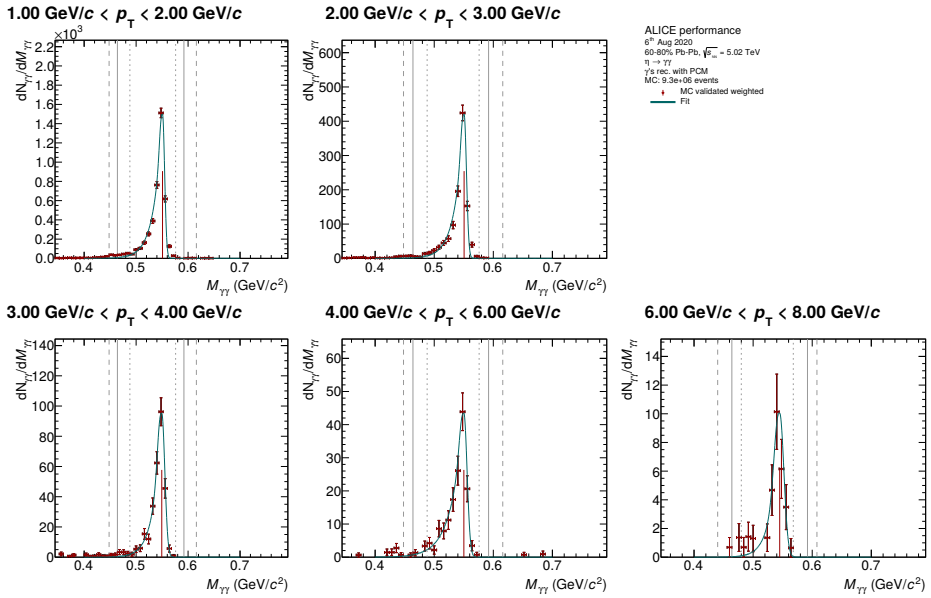

Figure A.16: Validated MC (LHC18∗ and LHC16i∗ from Table 7.2), 60-80%

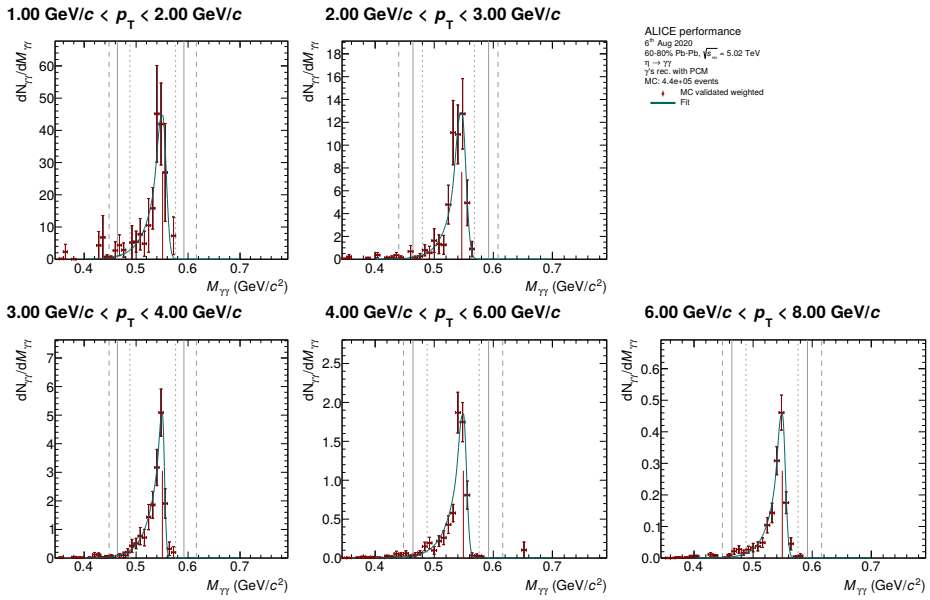

Figure A.17: MC with added signals (LHC16h4 from Table 7.2), validated, 60-80%

A.5 Merging of π^0 efficiencies

See Equation 7.16: ϵ is the merged efficiency, ϵ_{MB} the efficiency from LHC18$*$ and LHC16i$*$ (Min Bias), and ϵ_{AS} is the efficiency from LHC16h4 (Add Sig).

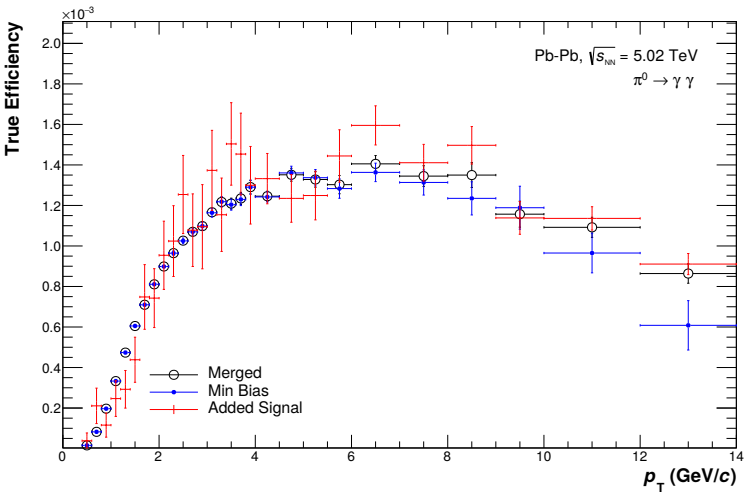

Figure A.18: Merging of π^0 efficiencies, 0-10%

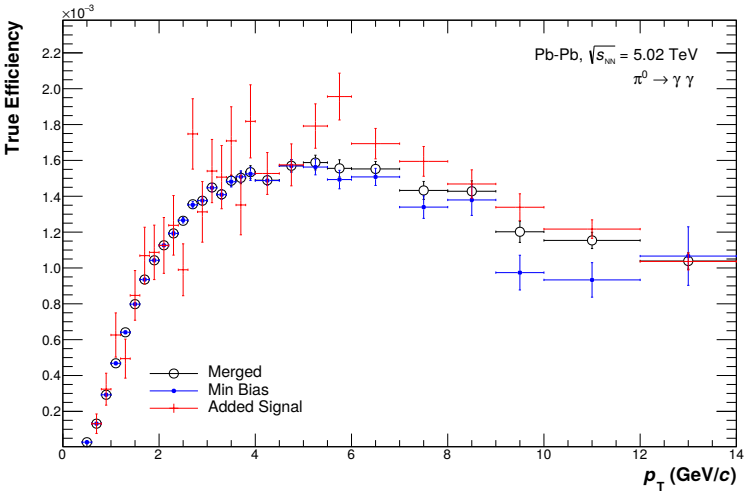

Figure A.19: Merging of π^0 efficiencies, 20-40%

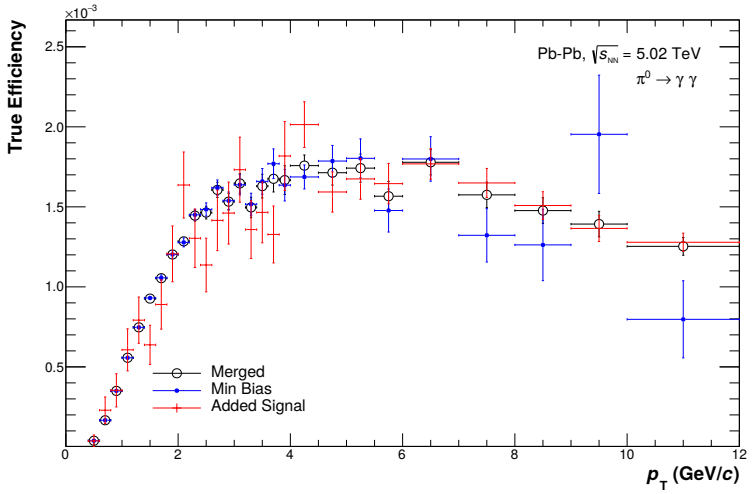

Figure A.20: Merging of π^0 efficiencies, 60-80%

A.6 Merging of η meson efficiencies

See Equation 7.16: ϵ is the merged efficiency, ϵ_{MB} the efficiency from LHC18$*$ and LHC16i$*$ (Min Bias), and ϵ_{AS} is the efficiency from LHC16h4 (Add Sig).

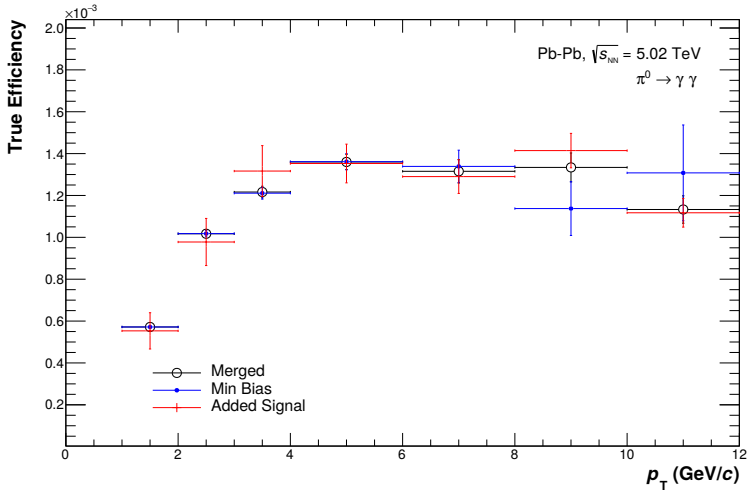

Figure A.21: Merging of η meson efficiencies, 0-20%

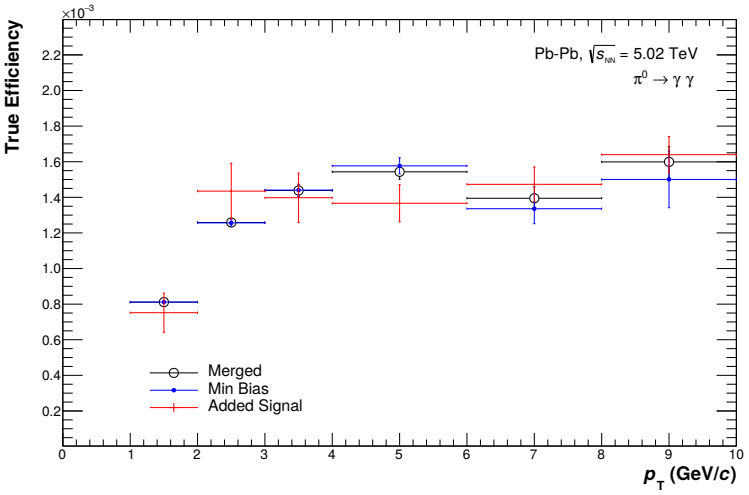

Figure A.22: Merging of η meson efficiencies, 20-40%

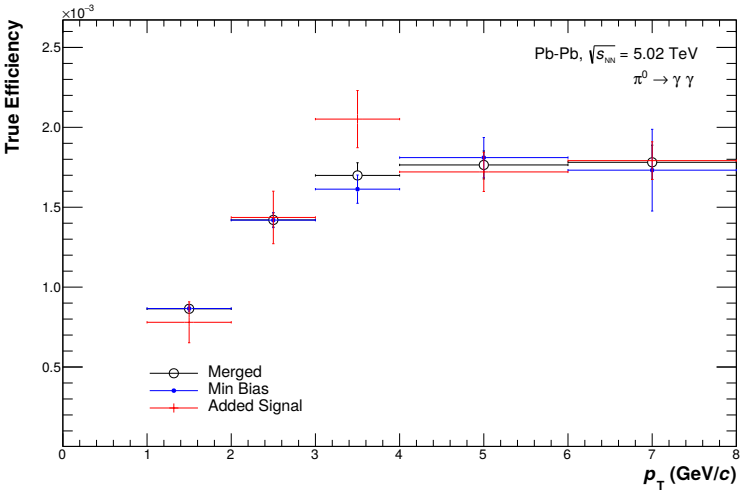

Figure A.23: Merging of η meson efficiencies, 60-80%

A.7 Reconstruction efficiencies corresponding to the right panel of Figure 7.13 for π^0 and η for all centrality classes

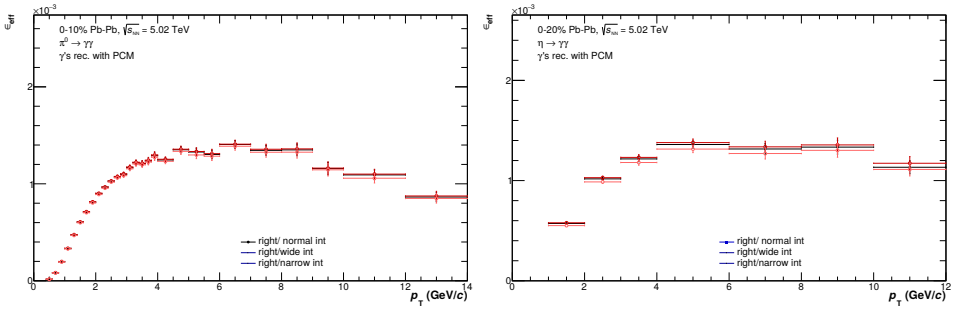

Figure A.24: 0-10% for π^0 and 0-20% for η

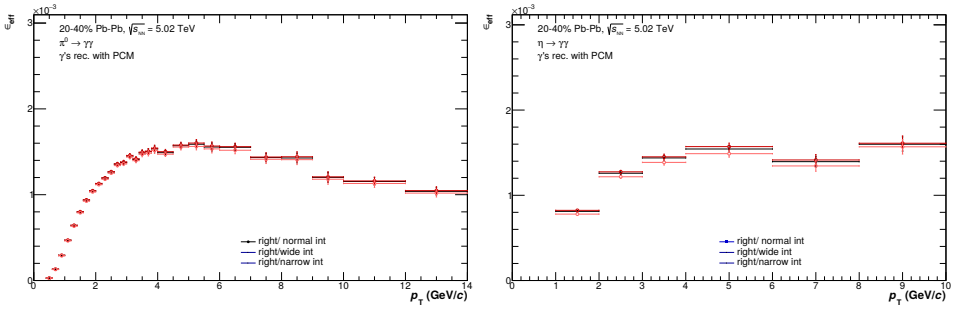

Figure A.25: 20-40% for π^0 and η

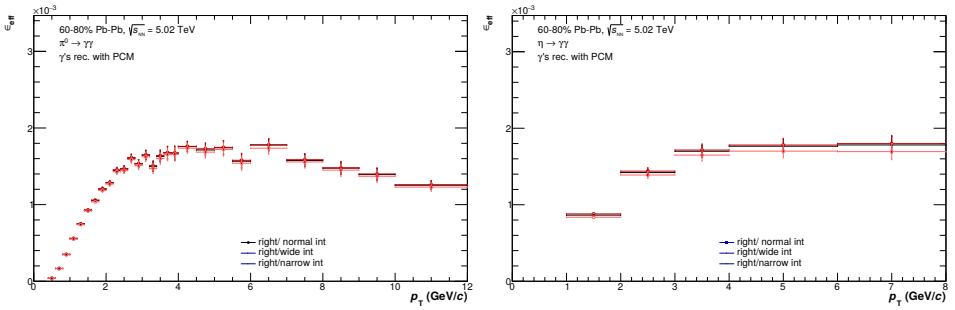

Figure A.26: 60-80% for π^0 and η

A.8 Cocktail parametrizations for the secondary π^0 correction corresponding to Figure 7.10 for 20-40% and 60-80%

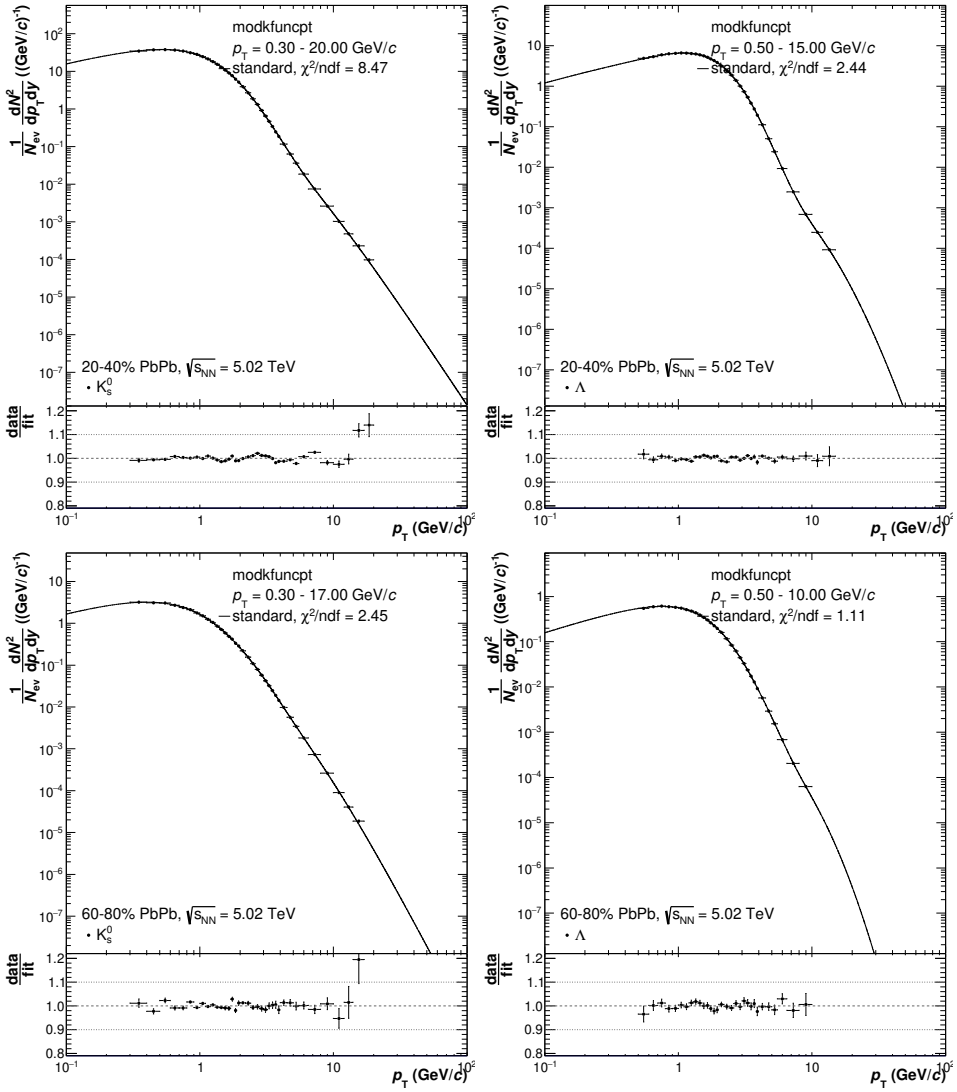

Figure A.27: 20-40% and 60-80%

A.9 Results without theory comparison

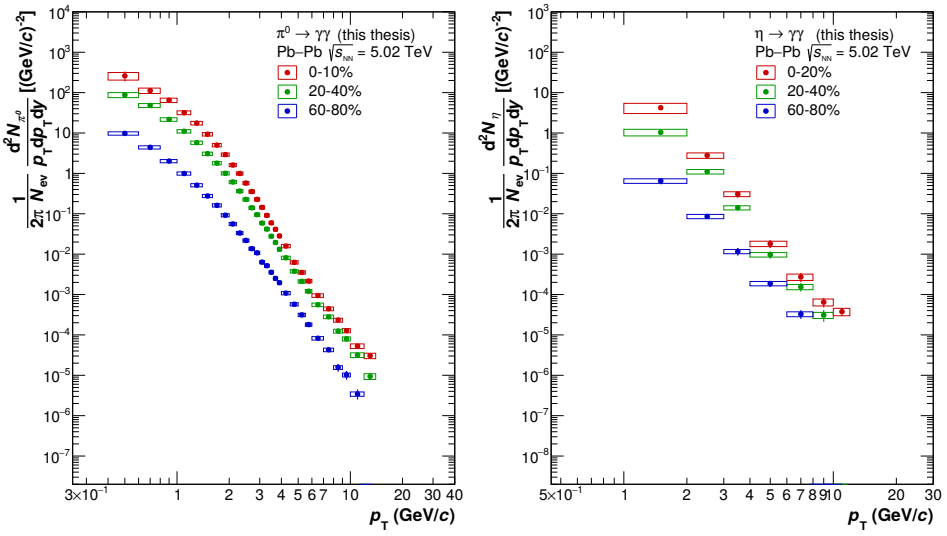

Figure A.28: Neutral meson spectra

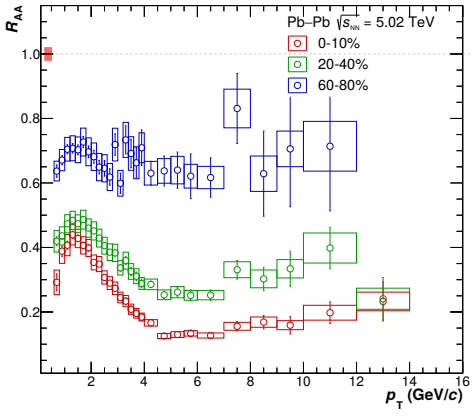

Figure A.29: π^0 R_{AA}

Appendix B

Additional direct photon figures

B.1 Purity of inclusive photons for 20-40% and 40-60% corresponding to Figure 8.6

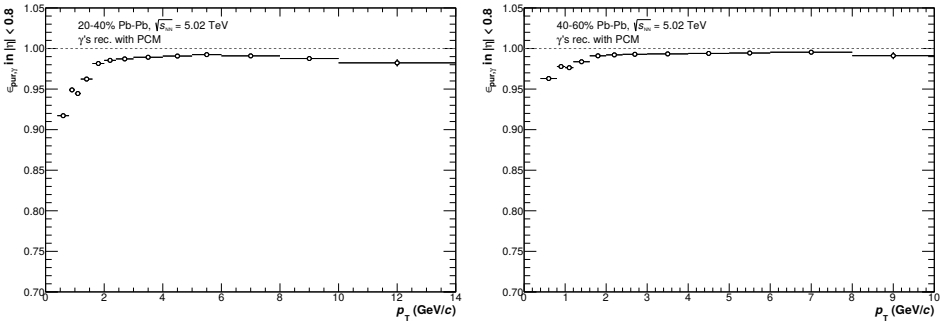

Figure B.1: 20-40% and 40-60%

B.2 Efficiency of inclusive photons for 20-40% and 40-60% corresponding to Figure 8.8

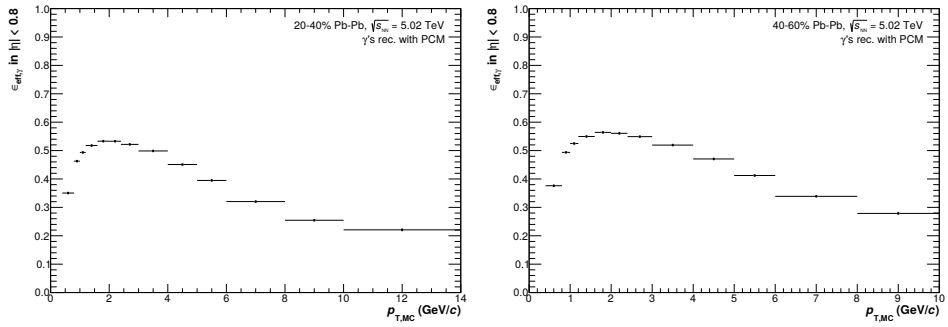

Figure B.2: 20-40% and 40-60%

B.3 Parametrizations for the decay photon cocktail for all centrality classes

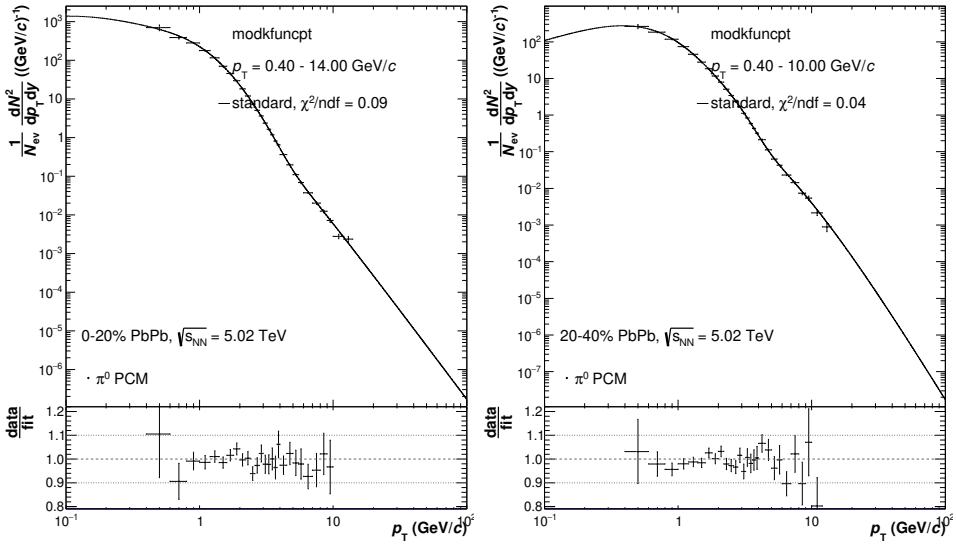

Figure B.3: π^0 0-20% and 20-40%

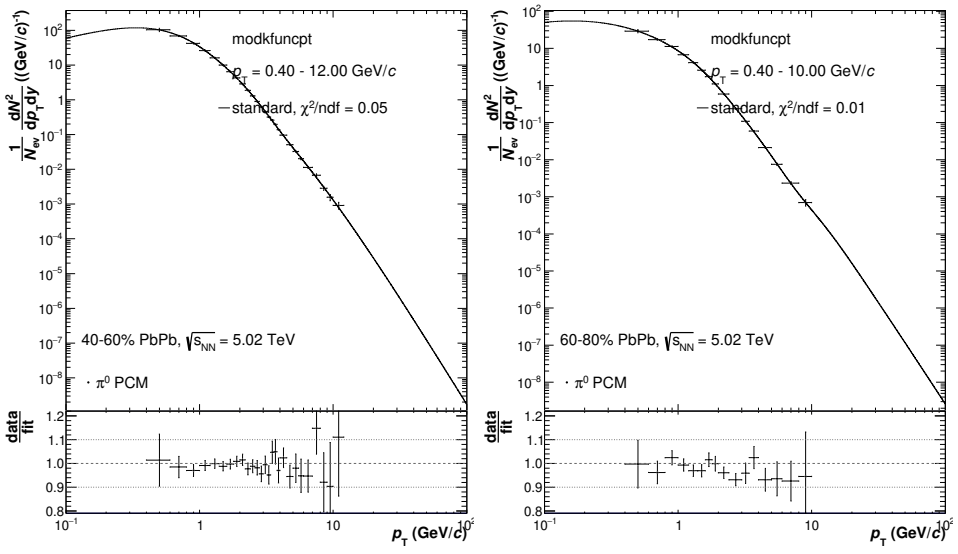

Figure B.4: π^0 40-60% and 60-80%

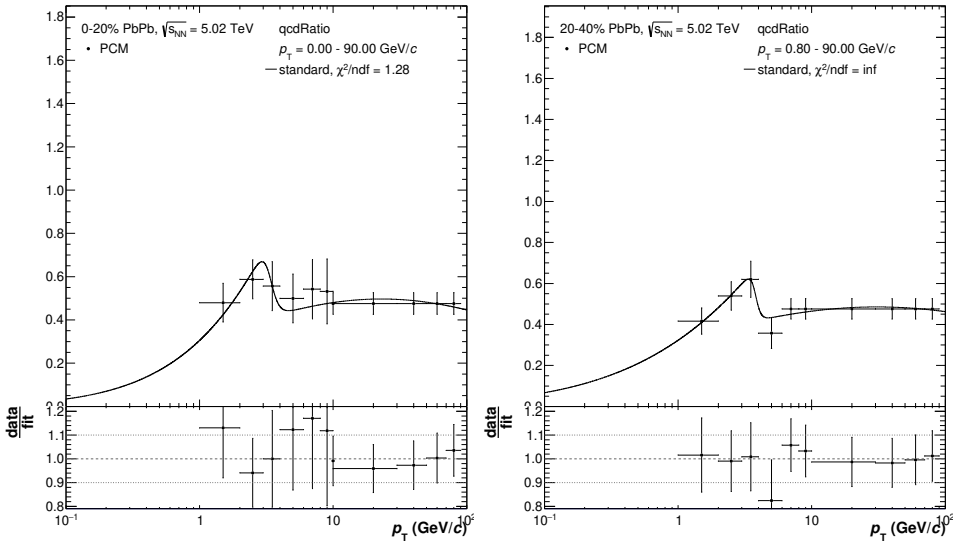

Figure B.5: η/π^0 0-20% and 20-40%

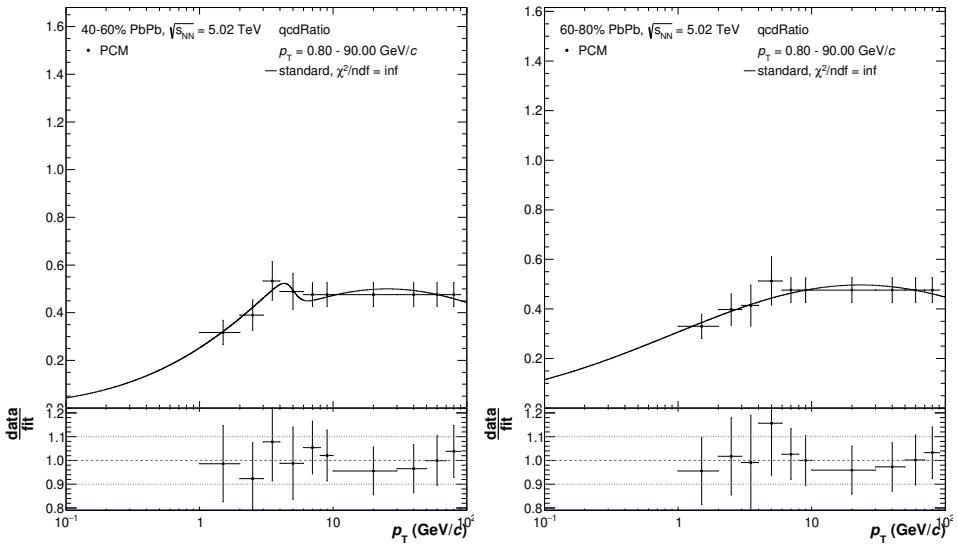

Figure B.6: η/π^0 40-60% and 60-80%

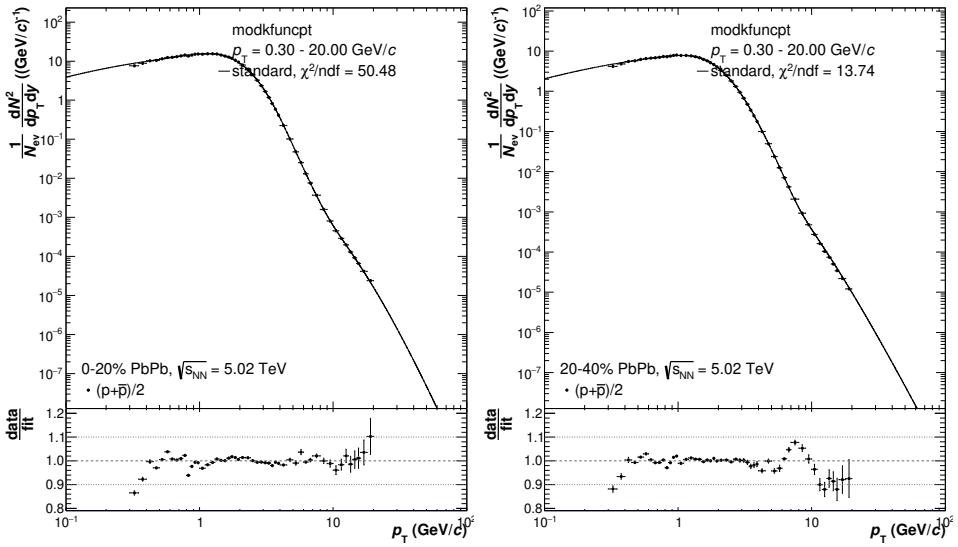

Figure B.7: Proton 0-20% and 20-40%

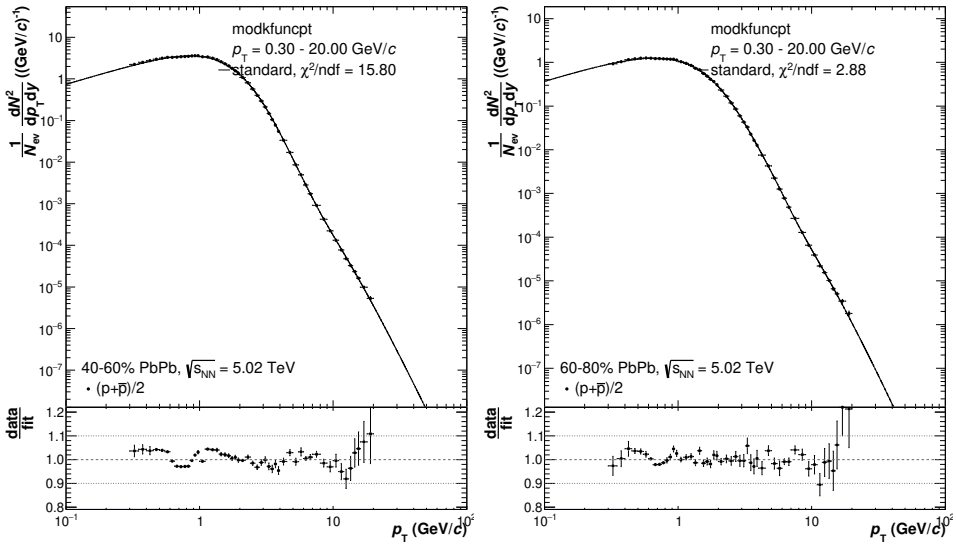

Figure B.8: Proton 40-60% and 60-80%

B.4 Inclusive and decay photon spectra for 20-40% and 40-60% corresponding to Figure 8.14

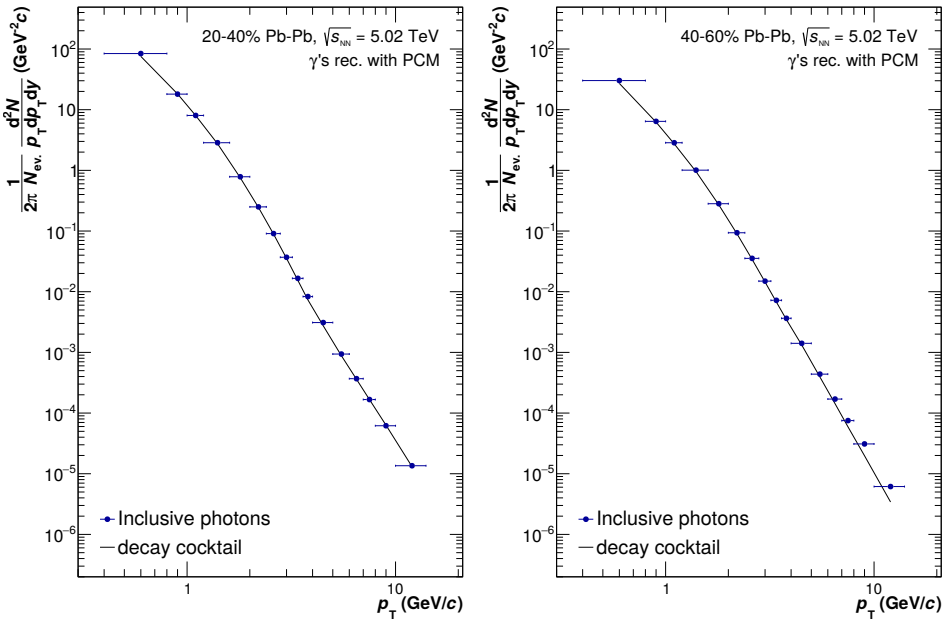

Figure B.9: 20-40% and 40-60%

B.5 γ/π^0 for 20-40% and 40-60% corresponding to Figure 8.15

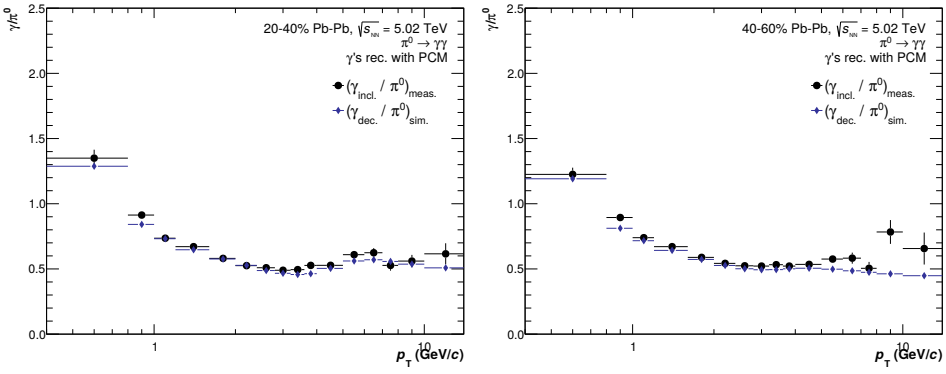

Figure B.10: 20-40% and 40-60%

B.6 Results without theory comparison

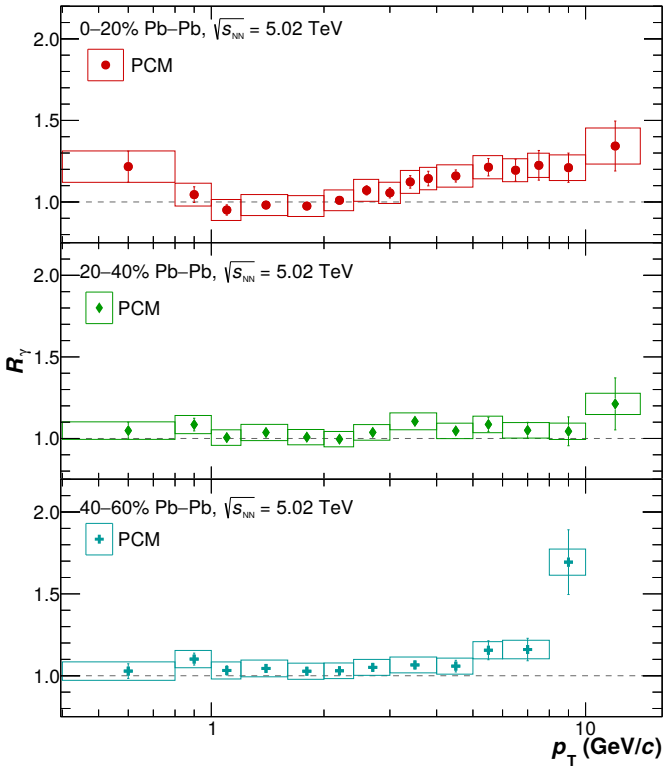

Figure B.11: Direct photon double ratio R_γ

List of Figures

List of Tables

Bibliography

[1] "New State of Matter created at CERN," 2000. https://home.cern/news/press-release/cern/new-state-matter-created-cern.

[2] U. Heinz and M. Jacob, "Evidence for a New State of Matter: An Assessment of the Results from the CERN Lead Beam Programme," 2000. https://arxiv.org/abs/nucl-th/0002042.

[3] B. Müller and J. L. Nagle, "Results from the Relativistic Heavy Ion Collider," *Annu. Rev. Nucl. Part. Sci. 56:93135* (2006) .

[4] "RHIC Detects Liquid State of Quark-Gluon Matter," 2005. https://www.aps.org/publications/apsnews/200506/rhic-liquid.cfm.

[5] ALICE Collaboration, "Neutral pion production at midrapidity in pp and Pb–Pb collisions at $\sqrt{s_{\mathrm{NN}}} = 2.76\,\mathrm{TeV}$," *Eur. Phys. J. C 74, 3108* (2014) .

[6] M. C. Danisch, "Neutral meson production measured with the Photon Conversion Method in Pb–Pb collisions at $\sqrt{s_{\mathrm{NN}}} = 5.02\,\mathrm{TeV}$," https://alice-notes.web.cern.ch/node/904 (2015) .

[7] M. C. Danisch, "Direct photon and light neutral meson production in the era of precision physics at the LHC." arXiv:2004.06906 [hep-ex], 2020.

[8] R. Hofstadter and R. W. McAllister, "Electron Scattering from the Proton," *Phys. Rev. 98, 217* (1955) .

[9] R. Hofstadter and R. W. McAllister, "Elastic Scattering of 188-Mev Electrons from the Proton and the Alpha Particle," *Phys. Rev. 102, 851* (1956) .

[10] M. Gell-Mann, "A Schematic Model of Baryons and Mesons," *Phys. Lett. 8, 214* (1964) .

[11] G. Zweig, "An SU(3) model for strong interaction symmetry and its breaking," *CERN-TH-401, CERN-TH-410* (1964) .

[12] J. D. Bjorken, "Applications of the Chiral U(6) ⊗ (6) Algebra of Current Densities," *Phys. Rev. 148, 1467* (1966) .

[13] E. D. Bloomet et al., "High-Energy Inelastic e–p Scattering at 6° and 10°," *Phys. Rev. Lett. 23, 930* (1969) .

[14] J. D. Bjorken and E. A. Paschos, "Inelastic Electron–Proton and γ–Proton Scattering and the Structure of the Nucleon," *Phys. Rev. 185, 1975* (1969) .

[15] R. P. Feynman, "Very high-energy collisions of hadrons," *Phys. Rev. Lett. 23, 1415* (1969) .

[16] Wikipedia: 'Standard Model of Elementary Particles' PBS NOVA, Fermilab, Particle Data Group (2019).

[17] H. D. Politzer, "Reliable Perturbative Results for Strong Interactions?," *Phys. Rev. Lett. 30, 1346* (1973) .

[18] D. J. Gross and F. Wilczek, "Ultraviolet Behavior of Nonabelian Gauge Theories," *Phys. Rev. Lett. 30, 1343* (1973) .

[19] C. H. Llewellyn Smith, "Inelastic Lepton Scattering In Gluon Models," *Phys. Rev. D 4, 2392* (1971) .

[20] J. I. Friedman and H. W. Kendall, "Deep inelastic electron scattering," *Ann. Rev. Nucl. Sci. 22, 203* (1972) .

[21] R. Brandelik et al. (TASSO Collaboration), "Evidence for Planar Events in e^+e^- Annihilation at High-Energies," *Phys. Lett. B 86, 243* (1979) .

[22] D. P. Barber et al., "Discovery of Three Jet Events and a Test of Quantum Chromodynamics at PETRA Energies," *Phys. Rev. Lett. 43, 830* (1979) .

[23] C. Berger et al. (PLUTO Collaboration), "Evidence for Gluon Bremsstrahlung in e^+e^- Annihilations at High-Energies," *Phys. Lett. B 86, 418* (1979) .

[24] W. Bartel et al. (JADE Collaboration), "Observation of Planar Three Jet Events in e^+e^- Annihilation and Evidence for Gluon Bremsstrahlung," *Phys. Lett. B 91, 142* (1980) .

[25] J. C. Collins and M. J. Perry, "Superdense matter: Neutrons or asymptotically free quarks?," *Phys. Rev. Lett. 34, 1353* (1975) .

[26] N. Cabibbo and G. Parisi, "Exponential hadronic spectrum and quark liberation," *Phys. Lett. B 59, 1, 67-69* (1975) .

[27] E. V. Shuryak, "Quantum chromodynamics and the theory of superdense matter," *Physics Reports 61, 2, 71-158* (1980) .

[28] K. G. Wilson, "Confinement of Quarks," *Phys. Rev. D 10, 2445* (1974) .

[29] M. Creutz, "Monte Carlo study of quantized SU(2) gauge theory," *Phys. Rev. D 21, 2308* (1989) .

[30] S. Dürr et al., "Ab-Initio Determination of Light Hadron Masses," *Science 322:1224-1227* (2008) .

[31] S. Gottlieb, A. Krasnitz, U. M. Heller, A. D. Kennedy, J. B. Kogut, R. L. Renken, D. K. Sinclair, R. L. Sugar, D. Toussaint, and K. C. Wang, "Thermodynamics of lattice QCD with two light quarks on a $16^3 \times 8$ lattice," *Phys. Rev. D 47, 3619* (1993) .

[32] A. Bazavov et al. (HotQCD Collaboration), "The equation of state in (2+1)-flavor QCD," *Phys. Rev. D 90, 094503* (2014) .

[33] R. Bellwied, S. Borsanyi, Z. Fodor, S. D Katz, C. Ratti, "Is There a Flavor Hierarchy in the Deconfinement Transition of QCD?," *Physical Review Letters 111, 202302* (2013) .

[34] A. Bazavov, H.-T. Ding, P. Hegde, O. Kaczmarek, F. Karsch, E. Laermann, Y. Maezawa, Swagato Mukherjee, H. Ohno, P. Petreczky, C. Schmidt, S. Sharma, W. Soeldner, and M. Wagner, "Strangeness at High Temperatures: From Hadrons to Quarks," *Phys. Rev. Lett. 111, 082301* (2013) .

[35] H.-T. Ding, F. Karsch, and S. Mukherjee, "Thermodynamics of strong-interaction matter from lattice QCD," *International Journal of Modern Physics E Vol. 24, No. 10, 153000* (2015) .

[36] Z. Fodor and S. Katz, "Critical point of QCD at finite T and μ, lattice results for physical quark masses," *J. High Energy Phys. 04, 050* (2004) .

[37] D. Boyanovsky, H. J. de Vega and D. J. Schwarz, "Phase transitions in the early and the present universe," *Annu. Rev. Nucl. Part. Sci. 56, 441500* (2006) .

[38] Y. Aoki, G. Endrodi, Z. Fodor, S. D. Katz, and K. K. Szabo, "The Order of the quantum chromodynamics transition predicted by the standard model of particle physics," *Nature 443, 675-678* (2006) .

[39] T. Bhattacharya et al., "QCD Phase Transition with Chiral Quarks and Physical Quark Masses," *Phys. Rev. Lett. 113, 8, 082001* (2014) .

[40] A. Bazavov et al., "Chiral crossover in QCD at zero and non-zero chemical potentials," *Phys. Lett. B 795* (2019) .

[41] M. Arneodo, "Nuclear effects in structure functions," *Physics Reports 240, 5, 301-393* (1994) .

[42] R. Snellings, "Collective Expansion at the LHC: selected ALICE anisotropic flow measurements," *Journal of Physics G, 41, 12* (2014) .

[43] S. Shi, "Event anisotropy v_2 at STAR," *PhD thesis. College of Physical Science and Technology, Central China Normal University* (2010) .

[44] C. Loizides, "Experimental overview on small collision systems at the LHC," *Nuclear Physics A 956, 200* (2016) .

[45] I. Arsene et al., "Quark-gluon plasma and color glass condensate at RHIC? The perspective from the BRAHMS experiment," *Nucl. Phys. A 757:1* (2005) .

[46] K. Adcox et al. (PHENIX Collaboration), "Formation of dense partonic matter in relativistic nucleus–nucleus collisions at RHIC: Experimental evaluation by the PHENIX Collaboration," *Nucl. Phys. A 757:184* (2005) .

[47] B.B. Back et al. (BRAHMS Collaboration), "The PHOBOS perspective on discoveries at RHIC," *Nucl. Phys. A 757:28* (2005) .

[48] J. Adams et al. (STAR Collaboration), "Experimental and theoretical challenges in the search for the quark–gluon plasma: The STAR Collaborations critical assessment of the evidence from RHIC collisions," *Nucl. Phys. A 757:102* (2005) .

[49] K. Reygers (PHENIX Collaboration), "High-p_{T} direct-photon results from PHENIX," *Acta Phys. Polon. B 37 727-732* (2006) .

[50] A. Andronic, P. Braun-Munzinger, K. Redlich and J. Stachel, "Decoding the phase structure of QCD via particle production at high energy," *Nature 561:321330* (2018) .

[51] R. Hagedorn, "Statistical thermodynamics of strong interactions at high-energies," *Nuovo Cim. Suppl. 3:147186* (1965) .

[52] K. Redlich and H. Satz, "The Legacy of Rolf Hagedorn: Statistical Bootstrap and ultimate Temperature," 2015. `https://arxiv.org/abs/1501.07523`.

[53] S. Borsanyi et al., "QCD equation of state at nonzero chemical potential: continuum results with physical quark masses at order μ^2," *J. High Energy Phys. 8, 53* (2012) .

[54] A. Andronic, P. Braun-Munzinger, M. K. Köhler, A. Mazeliauskas, K. Redlich, J. Stachel and V. Vislavicius, "The multiple-charm hierarchy in the statistical hadronization model," *J. High Energy Phys. 2021, 35* (2021) .

[55] P. Braun-Munzinger, J. Stachel, J. Wessels, and N. Xu, "Thermal equilibration and expansion in nucleus-nucleus collisions at the AGS," *Phys. Lett. B344, 4348* (1995) .

[56] J. Cleymans, H. Oeschler, and K. Redlich, "Influence of impact parameter on thermal description of relativistic heavy ion collisions at $(1-2)A\,\mathrm{GeV}$," *Phys. Rev. C 59, 1663* (1999) .

[57] P. Braun-Munzinger, I. Heppe, and J. Stachel, "Chemical equilibration in Pb+Pb collisions at the SPS," *Phys.Lett.B 465:15-20* (1999) .

[58] J. Manninen and F. Becattini, "Chemical freeze-out in ultrarelativistic heavy ion collisions at $\sqrt{s_{\mathrm{NN}}} = 130$ and $200\,\mathrm{GeV}$," *Phys. Rev. C 78, 054901* (2008) .

[59] A. Andronic, P. Braun-Munzinger, and J. Stachel, "Thermal hadron production in relativistic nuclear collisions: the hadron mass spectrum, the horn, and the QCD phase transition," *Phys. Lett. B 673, 142145* (2009) .

[60] STAR Collaboration, "Identified particle production, azimuthal anisotropy, and interferometry measurements in Au+Au collisions at $\sqrt{s_{\mathrm{NN}}} = 9.2\,\mathrm{GeV}$," *Phys. Rev. C 81, 024911* (2010) .

[61] L. Adamczyk et al. (STAR Collaboration), "Bulk properties of the medium produced in relativistic heavy-ion collisions from the beam energy scan program," *Phys. Rev. C 96, 044904* (2017) .

[62] M. Lisa, S. Pratt, R. Soltz, and U. Wiedemann, "Femtoscopy in relativistic heavy ion collisions," *Ann. Rev. Nucl. Part. Sci. 55, 357-402* (2005) .

[63] ALICE Collaboration, "Two-pion Bose–Einstein correlations in central Pb–Pb collisions at $\sqrt{s_{\mathrm{NN}}} = 2.76\,\mathrm{TeV}$," *Phys. Lett. B 696, 4, 328-337* (2011) .

[64] STAR Collaboration, "Beam-energy-dependent two-pion interferometry and the freeze-out eccentricity of pions measured in

heavy ion collisions at the STAR detector," *Phys. Rev. C 92, 1, 014904* (2015) .

[65] ALICE Collaboration, "Centrality determination in heavy ion collisions." ALICE-PUBLIC-2018-011, 2018. `https://cds.cern.ch/record/2636623/files/`.

[66] B. Abelev et al. (ALICE Collaboration), "Measurement of inelastic, single- and double-diffraction cross sections in proton–proton collisions at the LHC with ALICE," *Eur. Phys. J. C 73, 2456* (2013) .

[67] S. Tripathy, "Inelastic Normalization Factors for pp collisions at $\sqrt{s} = 5.02$, 8, and 13 TeV." ALICE-ANA-665, 2018. `https://alice-notes.web.cern.ch/node/665`.

[68] D. Amati, R. Petronzio, and G. Veneziano, "Relating hard QCD processes through universality of mass singularities (II)," *Nucl. Phys. B 146:29-49* (1978) .

[69] A. H. Mueller, "Cut vertices and their renormalization: A generalization of the Wilson expansion," *Phys. Rev. D 18, 3705* (1978) .

[70] S. Libby and G. Sterman, "Jet and lepton-pair production in high-energy lepton-hadron and hadron-hadron scattering," *Phys. Rev. D 18, 3252* (1978) .

[71] R. K. Ellis, H. Georgi, M. Machacek, H. D. Politzer, and G. G. Ross, "Perturbation theory and the parton model in QCD," *Nucl. Phys. B 152, 285-329* (1979) .

[72] D. de Florian et al., "Parton-to-Pion Fragmentation Reloaded," *Phys. Rev. D 91.1:014035* (2015) .

[73] S. Albino, B. A. Kniehl, and G. Kramer, "AKK Update: Improvements from New Theoretical Input and Experimental Data," *Nucl. Phys. B 803, 42104* (2008) .

[74] C. A. Aidala, F. Ellinghaus, R. Sassot, J. P. Seeleand M. Stratmann, "Global Analysis of Fragmentation Functions for Eta Mesons," *Phys. Rev. D 83, 034002* (2011) .

[75] H.-L. Lai, M. Guzzi, J. Huston, Z. Li, P. M. Nadolsky, J. Pumplin, and C.-P. Yuan, "New parton distributions for collider physics," *Phys. Rev. D 82, 074024* (2010) .

[76] S. Dulat et al., "New parton distribution functions from a global analysis of quantum chromodynamics." arXiv:1506.07443 [hep-ph], 2016.

[77] K. J. Eskola, P. Paakkinen, H. Paukkunen and C. A. Salgado, "EPPS16: Nuclear parton distributions with LHC data," *Eur. Phys. J. C 77, 3, 163* (2017) .

[78] JET Collaboration, "Extracting the jet transport coefficient from jet quenching in high-energy heavy-ion collisions," *Phys. Rev. C 90, 1, 014909* (2014) .

[79] K. Adcox et al. (PHENIX Collaboration), "Suppression of Hadrons with Large Transverse Momentum in Central Au + Au Collisions at $\sqrt{s_{\mathrm{NN}}} = 130\,\mathrm{GeV}$," *Phys. Rev. Lett. 88, 022301* (2001) .

[80] C. Adler et al. (STAR Collaboration), "Centrality Dependence of High-p_{T} Hadron Suppression in Au + Au Collisions at $\sqrt{s_{\mathrm{NN}}} = 130\,\mathrm{GeV}$," *Phys. Rev. Lett. 89, 202301* (2002) .

[81] S. S. Adler et al. (PHENIX), "Common Suppression Pattern of η and π^0 Mesons at High Transverse Momentum in Au+Au Collisions at $\sqrt{s_{\mathrm{NN}}} = 200\,\mathrm{GeV}$," *Phys. Rev. Lett. 96, 202301* (2006) .

[82] K. Aamodt et al. (ALICE Collaboration), "Suppression of charged particle production at large transverse momentum in central Pb–Pb collisions at $\sqrt{s_{\mathrm{NN}}} = 2.76\,\mathrm{TeV}$," *Physics Letters B 696:3039* (2011) .

[83] CMS Collaboration, "Study of high-p_{T} particle suppression in Pb–Pb compared to pp collisions at $\sqrt{s_{\mathrm{NN}}} = 2.76\,\mathrm{TeV}$," *Eur. Phys. J. C, 72:1945* (2012) .

[84] ATLAS Collaboration, "Measurement of charged-particle spectra in Pb+Pb collisions at $\sqrt{s_{\mathrm{NN}}} = 2.76\,\mathrm{TeV}$ with the ATLAS detector at the LHC," *J. High Energy Phys. 09, 050* (2015) .

[85] X.-N. Wang, "Energy dependence of jet quenching and lifetime of dense matter in high-energy heavy-ion collisions," *Phys. Rev. C 70, 031901(R)* (20014) .

[86] W. Dai, X.-F. Chen, B.-W. Zhang, E. Wang, "η meson production of high-energy nuclear collisions at NLO," *arXiv:1506.00838 [nucl-th]* (2015) .

[87] S. Acharya et al. (ALICE Collaboration), "Neutral pion and η meson production at mid-rapidity in Pb–Pb collisions at $\sqrt{s_{\mathrm{NN}}} = 2.76\,\mathrm{TeV}$," *Phys. Rev. C 98, 044901* (2018) .

[88] S. S. Adler et al. (PHENIX Collaboration), "High transverse momentum η meson production in p+p, d+Au, and Au+Au collisions at $\sqrt{s_{\mathrm{NN}}} = 200\,\mathrm{GeV}$," *Phys. Rev. C 75, 024909* (2007) .

[89] M. Bourquin and J.-M. Gaillard, "A Simple Phenomenological Description of Hadron Production," *Nucl. Phys. B 114:334–364* (1976) .

[90] R. Albrechtet al. (WA80 Collaboration), "Production of η mesons in 200 A GeV S+S and S+Au reactions," *Phys. Lett. B 361, 14* (1995) .

[91] C. Klein-Bösing, "Production of Neutral Pions and Direct Photons in Ultra-Relativistic Au+Au Collisions," *PhD thesis. Universität Münster* (2005) .

[92] P. Aurenche, A. Douiri, R. Baier, M. Fontannaz, D.Schiff, "Prompt photon production at large p_{T} in QCD beyond the leading order," *Phys. Lett. B, 140: 87-92* (1984) .

[93] L. Gordon and W. Vogelsang, "Polarized and unpolarized prompt photon production beyond the leading order," *Phys. Rev. D 48, 3136* (1993) .

[94] W. Vogelsang and M.R. Whalley, "A compilation of data on single and double prompt photon production in hadron hadron interactions," *J. Phys. G 23: A1A69* (1997) .

[95] M. Klasen, C. Klein-Bösing, F. König, and J. Wessels, "How robust is a thermal photon interpretation of the ALICE low-p_{T} data?," *J. High Energy Phys. 10, 119* (2013) .

[96] M. Glück, E. Reya and A. Vogt, "Parton fragmentation into photons beyond the leading order," *Phys. Rev. D 48, 116* (1993) .

[97] L. Bourhis, M. Fontannaz, and J. Guillet, "Quarks and gluon fragmentation functions into photons," *Eur. Phys. J. C 2, 529537* (1998) .

[98] R. J. Fries, B. Mueller, D. K. Srivastava, "High-energy photons from passage of jets through quark-gluon-plasma," *Phys. Rev. Lett. 90, 13, 132301* (2003) .

[99] T. Renk, "Photon Emission from a Medium-Modified Shower Evolution," *Phys. Rev. C 88, 034902* (2013) .

[100] J. Kapusta, P. Lichard, and D. Seibert, "High-energy photons from quark-gluon plasma versus hot hadronic gas," *Phys. Rev. D 44: 2774-2788* (1991) .

[101] R. Baier, H. Nakkagawa, A. Niegawa, and K. Redlich, "Production rate of hard thermal photons and screening of quark mass singularity," *Z. Phys. C 53* (1992) .

[102] P. Arnold, G. D. Moore, and L. G. Yaffe, "Photon emission from quark gluon plasma: Complete leading order results," *J. High Energy Phys. 12, 009* (2001) .

[103] S. Turbide, R. Rapp and C. Gale, "Hadronic production of thermal photons," *Phys. Rev. C 69, 014903* (2004) .

[104] K. L. Haglin, "Rate of photon production from hot hadronic matter," *J. Phys. G 30, L27L33* (2004) .

[105] W. Liu and R. Rapp, "Low-energy thermal photons from meson-meson bremsstrahlung," *Nucl. Phys. A 796, 1-4, 101-121* (2007) .

[106] O. Linnyk, V. Konchakovski, T. Steinert, W. Cassing, and E. L. Bratkovskaya, "Hadronic and partonic sources of direct photons in relativistic heavy-ion collisions," *Phys. Rev. C 92, 054914* (2015) .

[107] N. P. M. Holt, R. Rapp, "Baryonic Sources of Thermal Photons," *arXiv:2008.00116 [hep-ph]* (2020) .

[108] S. Turbide, C. Gale, E. Frodermann, and U. Heinz, "Electromagnetic radiation from nuclear collisions at ultrarelativistic energies," *Phys. Rev. C 77, 024909* (2008) .

[109] T. Lappi, L. McLerran, "Some Features of the Glasma," *Nucl. Phys. A 772, 200-212* (2006) .

[110] B. Schenke, P. Tribedy, and R. Venugopalan, "Fluctuating Glasma Initial Conditions and Flow in Heavy Ion Collisions," *Phys. Rev. Lett. 108, 252301* (2012) .

[111] J. Berges, K. Reygers, N. Tanji, and R. Venugopalan, "Parametric estimate of the relative photon yields from the glasma and the quark-gluon plasma in heavy-ion collisions," *Phys. Rev. C 95, 054904* (2017) .

[112] J. Churchill, L. Yan, S. Jeon, C. Gale, "Electromagnetic radiation from the pre-equilibrium/pre-hydro stage of the quark-gluon plasma." arXiv:2001.11110 [hep-ph], 2020.

[113] C. Gale, J.-F. Paquet, B. Schenke, C. Shen, "Probing Early-Time Dynamics and Quark-Gluon Plasma Transport Properties with Photons and Hadrons." arXiv:2002.05191 [hep-ph], 2020.

[114] M. Greif, F. Senzel, H. Kremer, K. Zhou, C. Greiner, and Z. Xu, "Nonequilibrium photon production in partonic transport simulations," *Phys. Rev. C 95, 054903* (2017) .

[115] K. Tuchin, "Photon decay in strong magnetic field in heavy-ion collisions," *Phys. Rev. C 83, 017901* (2011) .

[116] B. G. Zakharov, "Synchrotron contribution to photon emission from quark-gluon plasma," *JETP Lett. 104, 4, 213217, Pisma Zh. Eksp. Teor. Fiz. 104, 4, 215* (2016) .

[117] A. Ayala et al., "Prompt photon yield and elliptic flow from gluon fusion induced by magnetic fields in relativistic heavy-ion collisions," *Phys. Rev.D96, 11, 119901* (2017) .

[118] M. M. Aggarwal et al. (WA98 Collaboration), "Observation of Direct Photons in Central 158A GeV ^{208}Pb + ^{208}Pb Collisions," *Phys Rev. Lett., 85(17):3595* (2000) .

[119] S. S. Adler et al. (PHENIX Collaboration), "Centrality Dependence of Direct Photon Production in $\sqrt{s_{\mathrm{NN}}} = 200\,\mathrm{GeV}$ Au + Au Collisions," *Phys. Rev. Lett 94:232301* (2005) .

[120] A. Adare et al. (PHENIX Collaboration), "Enhanced production of direct photons in Au + Au collisions at $\sqrt{s_{\mathrm{NN}}} = 200\,\mathrm{GeV}$ and implications for the initial temperature," *Phys. Rev. Lett. 104: 132301* (2010) .

[121] A. Adare et al. (PHENIX Collaboration), "Centrality dependence of low-momentum direct-photon production in Au + Au collisions at $\sqrt{s_{\mathrm{NN}}} = 200\,\mathrm{GeV}$," *Phys. Rev. C 91: 064904* (2015) .

[122] M. Wilde (ALICE Collaboration), "Measurement of direct photons in pp and Pb–Pb collisions with ALICE," *Nucl. Phys. A 904, 573c* (2013) .

[123] J. Adam et al. (ALICE Collaboration), "Direct photon production in Pb–Pb collisions at $\sqrt{s_{\mathrm{NN}}} = 2.76\,\mathrm{TeV}$," *Phys. Lett. B 754:235-248* (2016) .

[124] STAR Collaboration, "Direct virtual photon production in Au+Au collisions at $\sqrt{s_{\mathrm{NN}}} = 200\,\mathrm{GeV}$," *Phys. Lett. B 770, 451-458* (2017) .

[125] A. Adare et al. (PHENIX Collaboration), "Observation of Direct-Photon Collective Flow in Au + Au Collisions at $\sqrt{s_{\mathrm{NN}}} = 200\,\mathrm{GeV}$," *Phys. Rev. Lett 109:122302* (2012) .

[126] S. Acharya et al. (ALICE Collaboration), "Direct photon elliptic flow in Pb–Pb collisions at $\sqrt{s_{\mathrm{NN}}} = 2.76\,\mathrm{TeV}$," *Phys. Lett. B 789:308-322* (2019) .

[127] K. Dusling, "Photons as a viscometer of heavy ion collisions," *Nucl. Phys. A, 839, 14, 70-77* (2010) .

[128] C. Shen, U. W. Heinz, J.-F. Paquet, I. Kozlov, and C. Gale, "Anisotropic flow of thermal photons as a quark-gluon plasma viscometer," *Phys. Rev. C 91, 2, 024908* (2015) .

[129] J.-F. Paquet, C. Shen, G. S. Denicol, M. Luzum, B. Schenke, S. Jeon, and C. Gale, "Production of photons in relativistic heavy-ion collisions," *Phys. Rev. C 93, 4, 044906* (2016) .

[130] C. Grupen, *Particle Detectors*. Cambridge University Press, 2008.

[131] CERN. `https://www.lhc-closer.es/taking_a_closer_look_at_lhc/1.lhc`.

[132] A. Tauro, ALICE Schematics. ALICE-PHO-SKE-2017-001 (2017).

[133] ALICE Collaboration, "The ALICE experiment at the CERN LHC," *J. Instrum. 3, S08002* (2008) .

[134] ALICE Collaboration, "Performance of the ALICE Experiment at the CERN LHC," *Int. J. Mod. Phys. A 29, 1430044* (2014) .

[135] K. Aamodt et al. (ALICE Collaboration), "Alignment of the ALICE Inner Tracking System with cosmic-ray tracks," *J. Instrum. 5, P03003* (2010) .

[136] J. Alme *et al.*, "The ALICE TPC, a large 3-dimensional tracking device with fast readout for ultra-high multiplicity events," *Nucl. Instrum. Meth. A 622, 316-367* (2010) .

[137] ALICE Collaboration, "The ALICE Transition Radiation Detector: Construction, operation, and performance," *Nuclear Instruments and Methods in Physics Research A 881, 11* (2018) .

[138] M. O. Schmidt, "Space Point Calibration of the ALICE TPC with Track Residuals," *PhD thesis. Universität Heidelberg* (2020) .

[139] ALICE EMCal Collaboration, "ALICE EMCal Physics Performance Report," 2010. `https://arxiv.org/abs/1008.0413`.

[140] J. Allen *et al.*, "ALICE DCal: An Addendum to the EMCal Technical Design Report Di-Jet and Hadron-Jet correlation measurements in ALICE," 2010. CERN-LHCC-2010-011, ALICE-TDR-14-add-1.

[141] ALICE Collaboration, "PHOS, the ALICE-PHOton spectrometer," *J.Phys.G 34, 719* (2007) .

[142] D. Blau for the ALICE collaboration, "Calibration of the ALICE PHOS calorimeter," *J. Phys. Conf. Ser. 1390, 1, 012113* (2019) .

[143] F. Bock, "R distribution of reconstructed photon conversions (LHC10d) compared to MC (Phojet)," ALI-PERF-6268 (2012) .

[144] "An object-oriented data analysis framework." `http://root.cern.ch`.

[145] I. Foster and C. Kesselmann, "The grid: blueprint for a new comuting infrastructure," *Morgan Kaufmann Publishers* (1999) .

[146] P. Saiz et al., "AliEn - ALICE environment on the GRID," *Nucl. Instrum. Meth. A 502* (2003) .

[147] ALICE Collaboration, "ALICE: Physics Performance Report, Volume II," *J. Phys. G 32:1295-2040* (2006) .

[148] R. E. Kalman, "A new approach to linear filltering and prediction problems," *Trans. ASME, Series D, J. BasicEng., 82* (1960) .

[149] P. S. Maybeck, *Stochastic models, estimation, and control*. Academic Press, 1979.

[150] R. Frühwirth, "Application of Kalman filtering to trackand vertex fitting," *Nucl. Instrum. Meth. A 262* (1987) .

[151] I. Kisel, I. Kulakov, and M. Zyzak, "Standalone first level event selection package for the CBM experiment," *IEEE Transactions on Nuclear Science 60, 5, 3703-3708* (2013) .

[152] M. Arslandok, "ALICE TPC dE/dx performace in Run2 5.02 TeV Pb-Pb low-Interaction rate runs," ALI-PERF-107348 (2016) .

[153] N. Jacazio, "TOF β vs Momentum performance in Pb–Pb at 5.02 TeV (LHC15o)," ALI-PERF-106336 (2018) .

[154] ALICE Collaboration, "Centrality determination of Pb–Pb collisions at $\sqrt{s_{\mathrm{NN}}} = 2.76\,\mathrm{TeV}$ with ALICE," *Phys. Rev. C 88, 044909* (2013) .

[155] M. Miller, K. Reygers, S. J. Sanders, and P. Steinberg, "Glauber modeling in high-energy nuclear collisions," *Ann. Rev. Nucl. Part. Sci. 57, 205* (2007) .

[156] R. J. Glauber, "Cross sections in deuterium at high energies," *Phys. Rev. 100, 242* (1955) .

[157] UA 5 Collaboration, "Charged particle multiplicity distributions at 200 and 900 GeV c.m. energy," *Z. Phys. C - Particles and Fields 43: 357-374* (1989) .

[158] A. Toia and D. Chinellato, "Centrality determination in Pb–Pb collisions at 5.02 TeV," 2017. `https://alice-notes.web.cern.ch/system/files/notes/analysis/453/2017-Sep-26-analysis_note-ALICE_analysis_note.pdf`.

[159] R. Brun, A. C. McPherson, P. Zanarini, M. Maire and F. Bruyant, "GEANT 3: user's guide Geant 3.10, Geant 3.11," 1987.

[160] X. N. Wang and M. Gyulassy, "HIJING: a Monte Carlo model for multiple jet production in pp, pA and AA collisions," *Phys. Rev. D 44, 3501* (1991) .

[161] Particle Data Group, "Particle physics booklet," 2014.

[162] F. Bock, "ALICE Capabilities for Studying Photon Physics with the Conversion Method at LHC Energies." Bachelor thesis, University of Heidelberg, 2010.

[163] S. Acharya *et al.*, "Centrality and transverse momentum dependence of inclusive J/ψ production at midrapidity in Pb–Pb collisions at $\sqrt{s_{\mathrm{NN}}} = 5.02$ TeV," *Phys. Lett. B 805, 135434* (2020) .

[164] L. Leardini, "Measurement of neutral mesons and direct photons in Pb–Pb collisions at $\sqrt{s_{\mathrm{NN}}} = 2.76$ TeV with the ALICE experiment at the LHC," *PhD thesis. University of Heidelberg* (2017) .

[165] T. Dahms, "Measurement of photons via conversion pairs with the PHENIX experiment at RHIC," Master's thesis, Stony Brook University, 2005.

[166] J. Podolanski and R. Armenteros, "Analysis of V-Events," *Phil. Mag. 7* (1954) .

[167] Radoslav Rusanov, "Measurement of neutral-pion production suppression in Pb–Pb collisions at $\sqrt{s_{\mathrm{NN}}} = 2.76$ TeV with ALICE at the CERN LHC." Diploma thesis, University of Heidelberg, 2011.

[168] ALICE Collaboration, "Strange and multi-strange particle production in Pb–Pb at $\sqrt{s_{\mathrm{NN}}} = 5.02$ TeV," 2019. `https://alice-notes.web.cern.ch/node/588`.

[169] ALICE Collaboration, "Direct photon production at low transverse momentum in proton-proton collisions at $\sqrt{s} = 2.76$ TeV and 8 TeV." arXiv:1803.09857 [nucl-ex], 2018.

[170] T. Sjöstrand, S. Mrenna, P. Skands, "PYTHIA 6.4 Physics and Manual," *J. High Energy Phys. 05, 026* (2006) .

[171] R. Barlow, "Systematic Errors: Facts and Fictions," 2002. `https://arxiv.org/pdf/hep-ex/0207026.pdf`.

[172] F. Bock, "Neutral Pion and Eta Meson Production in pp and Pb-Pb Collisions at the LHC with the ALICE Detector," *Master thesis. University of Heidelberg* (2012) .

[173] V. Begun, W. Florkowski, M. Rybczynski, "Explanation of hadron transverse momentum spectra in heavy-ion collisions at $\sqrt{s_{\mathrm{NN}}} = 2.76\,\mathrm{TeV}$ within a chemical nonequilibrium statistical hadronization model," *Phys. Rev. C 90, 1, 014906* (2014) .

[174] K. Werner, Iu. Karpenko, M. Bleicher, T. Pierog and S. Porteboeuf-Houssais, "Jets, bulk matter, and their interaction in heavy ion collisions at several TeV," *Phys. Rev. C 85 064907* (2012) .

[175] G. D. Lafferty, T. R. Wyatt, "Where to Stick Your Data Points: The Treatment of Measurements Within Wide Bins," *Nuclear Instruments and Methods in Physics Research A 355* (1995) .

[176] W. Broniowski and W. Florkowski, "Explanation of the RHIC p(T) spectra in a thermal model with expansion," *Phys. Rev. Lett. 87, 272302* (2001) .

[177] J.-F. Paquet. private communication.

[178] M. H. P. Sas for the ALICE Collaboration, "Light neutral meson production in heavy ion collisions with ALICE in the era of precision physics at the LHC," *Contribution to the Quark Matter conference* (2019) .

[179] L.-G. Pang, H. Petersen, and X.-N. Wang, "Pseudorapidity distribution and decorrelation of anisotropic flow within the open-computing-language implementation CLVisc hydrodynamics," *Phys. Rev. C 97, 064918* (2018) .

[180] M. Djordjevic, M. Djordjevic, "LHC jet suppression of light and heavy flavor observables," *Phys. Lett. B 734:286-289* (2014) .

[181] Y.-T. Chien, A. Emerman, Z.-B. Kang, G. Ovanesyan, and I. Vitev, "Jet quenching from QCD evolution," *Phys. Rev. D 93, 074030* (2016) .

[182] G. D'Agostini, "A Multidimensional unfolding method based on Bayes' theorem," *Nucl. Instrum. Meth. A 362, 487498* (1995) .

[183] K. Reygers. Private communication.

[184] P. K. Khandai, P. Shukla, V. Singh, "Meson spectra and m_{T} scaling in p+p, d+Au and Au+Au collisions at $\sqrt{s_{\mathrm{NN}}} = 200\,\mathrm{GeV}$," *Phys. Rev. C 84, 054904* (2011) .

[185] ALICE Collaboration, "Production of $\mathrm{K}^*(892)^0$ and $\phi(1020)$ in pp and Pb–Pb collisions at $\sqrt{s_{\mathrm{NN}}} = 5.02\,\mathrm{TeV}$," 2019. `https://arxiv.org/abs/2106.13113`.

[186] L. Altenkämper, "Measurement of Direct Photons in Proton-Proton Collisions at $\sqrt{s} = 7\,\mathrm{TeV}$ with ALICE," Master's thesis, University of Heidelberg, 2016.

[187] ALICE Collaboration, "Production of charged pions, kaons and (anti-)protons in Pb–Pb and inelastic pp collisions at $\sqrt{s_{\mathrm{NN}}} = 5.02\,\mathrm{TeV}$," *Phys. Rev. C 101, 044907* (2020) .

[188] S. Acharya et al. (ALICE Collaboration), "π^0 and η meson production in proton–proton collisions at $\sqrt{s} = 8\,\mathrm{TeV}$," *EPJ C 78, 263* (2018) .

[189] S. Acharya et al. (ALICE Collaboration), "Neutral pion and η meson production in p–Pb collisions at $\sqrt{s_{\mathrm{NN}}} = 5.02\,\mathrm{TeV}$," *EPJ C 78, 624* (2018) .

[190] P. Dasgupta, S. De, R. Chatterjee, and D. K. Srivastava, "Photon production from Pb+Pb collisions at $\sqrt{s_{\mathrm{NN}}} = 5.02\,\mathrm{TeV}$ at LHC and at $\sqrt{s_{\mathrm{NN}}} = 39$ TeV at FCC," *Phys. Rev. C 98, 024911* (2018) .

[191] J. Pumplin et al., "New generation of parton distributions with uncertainties from global QCD analysis," *J. High Energy Phys. 07, 012* (2002) .

[192] C. Gale, J.-F. Paquet, B. Schenke, C. Shen, "Multi-messenger heavy-ion physics." arXiv:2106.11216 [nucl-th], 2021.

[193] H. van Hees, M. He, R. Rapp, "Pseudo-Critical Enhancement of Thermal Photons in Relativistic Heavy-Ion Collisions," *Nucl. Phys. A 933: 256271* (2015) .

[194] R. Chatterjee, H. Holopainen, T. Renk, and K. J. Eskola, "Collision centrality and τ_0 dependence of the emission of thermal photons from a fluctuating initial state in an ideal hydrodynamic calculation," *Phys. Rev. C 85, 064910* (2012) .

[195] S. De, "Extent of sensitivity of single photon production to parton distribution functions," 2013. `https://arxiv.org/abs/1305.0624`.

[196] D. K. Srivastava, "Scaling of single photon production in hadronic collisions," *Eur. Phys. J. C 22: 129-132* (2001) .

[197] A. Kurkela, A. Mazeliauskas, J.-F. Paquet, S. Schlichting, and D. Teaney, "Effective kinetic description of event-by-event pre-equilibrium dynamics in high-energy heavy-ion collisions," *Phys. Rev. C 99, 034910* (2019) .

[198] B. Schenke, S. Jeon, and C. Gale, "(3+1)D hydrodynamic simulation of relativistic heavy-ion collisions," *Phys. Rev. C 82, 014903* (2010) .

[199] C. Shen, Z. Qiu, H. Song, J. Bernhard, S. Bass, and U. Heinz, "The iEBE-VISHNU code package for relativistic heavy-ion collisions," *Comput. Phys. Commun. 199, 61-85* (2016) .

[200] W. Cassing and E.L. Bratkovskaya, "Parton-Hadron-String Dynamics: an off-shell transport approach for relativistic energies," *Nucl. Phys. A 831, 215-242* (2009) .

[201] J. Churchill, L. Yan, S. Jeon, and C. Gale, "Emission of electromagnetic radiation from the early stages of relativistic heavy-ion collisions," *Phys. Rev. C 103, 024904* (2021) .

[202] S. Stiefelmaier, "Improving the accuracy of the photon conversion method in ALICE." Masters thesis, University of Heidelberg, 2017. `https://www.physi.uni-heidelberg.de//Publications/thesis_as_uploaded_to_physi.pdf`.

[203] A. Marín private communication.

[204] A. Adare *et al.*, "Azimuthally anisotropic emission of low-momentum direct photons in Au+Au collisions at $\sqrt{s_{NN}} = 200$ GeV," *Phys. Rev. C 94, 6, 064901* (2016) .

[205] A. Andronic, "An overview of the experimental study of quark-gluon matter in high-energy nucleus-nucleus collisions," *Int. J. Mod. Phys. A 29, 1430047* (2014) .

[206] P. Braun-Munzinger, J. Stachel, "The quest for the quark-gluon plasma," *Nature 448, 302309* (2007) .

[207] U. Heinz, "From SPS to RHIC: Maurice and the CERN heavy-ion programme," *Phys. Scripta 78 028005* (2008) .

[208] F. Wilzek, "QCD Made Simple," *Physics Today53, 8, 22* (2000) .

[209] R. L. Jaffe, "One Theorists Perspective on Four Eras of Electron-Proton Scattering," (1998) .

[210] J. Ellis, "The Discovery of the Gluon," *World Scientific, 50 Years of Quarks, pp. 189-198* (2015) .

[211] G. David, "Direct real photons in relativistic heavy ion collisions," *Rept. Prog. Phys. 83, 4, 046301* (2020) .

Acknowledgements

First of all, I would like to thank my supervisor Prof. Dr. Johanna Stachel for the opportunity to work on this interesting topic and for her encouragement and guidance over the whole time. Also, for the opportunity to visit several conferences which were some of the highlights of my PhD. I thank Prof. Dr. Hans-Christian Schultz-Coulon to be available as second referee. Many thanks to Klaus, Ana, Ole and Jiyoung for proofreading parts of this thesis. I am grateful to Ana for her selfless support and all her good ideas and to Klaus for all the helpful discussions. Thanks to Lucia, who introduced me to the neutral meson and direct photon analysis and the whole photon conversion group for their coding work and technical assistance. Furthermore, I would like to thank the whole ALICE PI group for the lunch and coffee breaks including encouragement, discussions about physics, politics, and anything one can think of, without which the PhD time would have been much less fun. Those people outside of the ALICE collaboration to whom I am very thankful for their support, already know.